ELECTRON TRANSPORT DYNAMICS IN SEMICONDUCTOR HETEROSTRUCTURE DEVICES

by

IAN PILGRIM

A DISSERTATION

Presented to the Department of Physics
and the Graduate School of the University of Oregon
in partial fulfillment of the requirements
for the degree of
Doctor of Philosophy

September 2014

DISSERTATION APPROVAL PAGE

Student: Ian Pilgrim

Title: Electron Transport Dynamics in Semiconductor Heterostructure Devices

This dissertation has been accepted and approved in partial fulfillment of the requirements for the Doctor of Philosophy degree in the Department of Physics by:

Dr. Jens Nöckel	Chair
Dr. Richard Taylor	Advisor
Dr. Roger Haydock	Core Member
Dr. Mark Lonergan	Institutional Representative

and

J. Andrew Berglund	Dean of the Graduate School

Original approval signatures are on file with the University of Oregon Graduate School.

Degree awarded September 2014

© CC BY-SA 4.0 2014 Ian Pilgrim

DISSERTATION ABSTRACT

Ian Pilgrim

Doctor of Philosophy

Department of Physics

September 2014

Title: Electron Transport Dynamics in Semiconductor Heterostructure Devices

Modern semiconductor fabrication techniques allow for the fabrication of semiconductor heterostructures which host electron transport with a minimum of scattering sites. In such devices, electrons populate a two-dimensional electron gas (2DEG) in which electrons propagate in exactly two dimensions, and may be further confined by potential barriers to form electron billiards. At sub-Kelvin temperatures, electron trajectories are determined largely by reflections from the billiard walls, while net conduction through the device depends on quantum mechanical wave interference.

Measurements of magnetoconductance fluctuations (MCF) serve as a probe of dynamics within the electron billiard. Many prior studies have utilized heterostructures employing the modulation doping architecture, in which the 2DEG is spatially removed from the donor atoms to minimize electron scattering. Theoretical studies have claimed that MCF will be fractal when the confinement potential defining the billiard is soft-walled, regardless of the presence of smooth potentials within the billiard such as those introduced by remote ionized donors. The small-angle scattering sites resulting from these potentials are often disregarded as negligible; we use MCF measurements to investigate such claims.

To probe the effect of remote ionized donor scattering on the phase space in electron billiards, we compare MCF measured on billiards in a modulation-doped heterostructure to those measured on billiards in an undoped heterostructure, in which this potential landscape is believed to be absent. Fractal studies are performed on these MCF traces, and we find that MCF measured on the undoped billiards do not exhibit measurably different fractal characteristics than those measured on the modulation-doped billiards.

Having confirmed that the potential landscapes in modulation-doped heterostructures do not affect the electron phase space, we then investigate the effect of these impurities on the distribution of electron trajectories through the billiards. By employing thermal cycling experiments, we demonstrate that this distribution is highly sensitive to the precise potential landscape within the billiard, suggesting that modulation-doped heterostructures do not support fully ballistic electron transport. We compare our MCF correlation data with the dynamics of charge transfer within heterostructure systems to make qualitative conclusions regarding these dynamics.

CURRICULUM VITAE

NAME OF AUTHOR: Ian Pilgrim

GRADUATE AND UNDERGRADUATE SCHOOLS ATTENDED:

University of Oregon, Eugene, Oregon
Whitman College, Walla Walla, Washington

DEGREES AWARDED:

Doctor of Philosophy in Physics, 2014, University of Oregon
Bachelor of Arts in Mathematics-Physics, 2008, Whitman College

AREAS OF SPECIAL INTEREST:

Low-Temperature Experiment, Electron Transport in Mesoscopic Systems, Fractal Analysis

PROFESSIONAL EXPERIENCE:

Graduate Research Assistant, University of Oregon, 2009 - 2014

Graduate Teaching Fellow, University of Oregon, 2008 - 2009

GRANTS, AWARDS AND HONORS:

Science Literacy Program Fellow, University of Oregon, 2013

PUBLICATIONS:

A. P. Micolich, A. M. See, B. C. Scannell, C. A. Marlow, T. P. Martin, I. Pilgrim, A. R. Hamilton, H. Linke, and R. P. Taylor. Is it the boundaries or disorder that dominates electron transport in semiconductor ‘billiards’? *Fortschr. Phys.*, 61:332, 2013.

A. M. See, I. Pilgrim, B. C. Scannell, R. D. Montgomery, O. Klochan, A. M. Burke, M. Aagesen, P. E. Lindelof, I. Farrer, D. A. Ritchie, R. P. Taylor, A. R. Hamilton, and A. P. Micolich. Impact of small-angle scattering on ballistic transport in quantum dots. *Phys. Rev. Lett.*, 108:196807, 2012.

B. C. Scannell, I. Pilgrim, A. M. See, R. D. Montgomery, P. K. Morse, M. S. Fairbanks, C. A. Marlow, H. Linke, I. Farrer, D. A. Ritchie, A. R. Hamilton, A. P. Micolich, L. Eaves, and R. P. Taylor. Probing the sensitivity of electron wave interference to disorder-induced scattering in solid-state devices. *Phys. Rev. B*, 85:195319, 2012.

M. Pokrifchak, T. Turner, I. Pilgrim, M. R. Johnston, and K. W. Hipps. Scanning tunneling microscopy and orbital-mediated tunneling spectroscopy study of 1,5-di(octyloxy)anthracene adsorbed on highly ordered pyroliytic graphite from various solvents and in different environments. *J. Phys. Chem. C*, 111:7735, 2007.

ACKNOWLEDGEMENTS

This dissertation represents the culmination of an educational journey of more than two decades, during which I have been the beneficiary of a wealth of extraordinary opportunities and exceptional support. I humbly and sincerely thank everybody who has privileged me with their guidance, trust, and inspiration.

First and foremost, I thank my parents, Ric and Rita Pilgrim, whose boundless love and support are a constant source of inspiration to me. From an early age, they have encouraged my inquisitive spirit and given me countless opportunities to pursue my passions and explore my world; no written acknowledgment could possibly capture the love and gratitude I wish to express.

I thank my advisor, Dr. Richard Taylor, for his patient and insightful mentorship over the past five years. It has been a joy and an honor to work under an advisor with such a breadth of professional interests and expertise, and I have a deep appreciation for Dr. Taylor's personal philosophies on the intersection of physics and art.

I thank Jeff Hashimoto, my high school IB Physics teacher, for instilling in me a love for physics that would inspire me to pursue the subject in college and beyond. It was in Mr. Hashimoto's class that I first grasped the true elegance and utility of physics through hands-on demonstrations and projects.

From Whitman College, I thank Drs. Doug Juers, Kurt Hoffman, and Mark Beck for providing me with an excellent and entertaining physics education, as well as Dr. Laura Schueller for teaching me the LaTeX skills that would become invaluable to me as a physicist. From the University of Oregon, I thank Dr. Hailin Wang for an enlightening experience as an REU student, Dr. John Toner for sharing his engaging and profound understanding of physics, and Dr. Mike Raymer for the opportunity to take part in the Science Literacy Program. I thank my committee members, Drs. Jens Nöckel, Roger Haydock, and Mark Lonergan, for their time and flexibility in the weeks leading to my oral dissertation defense.

I am very grateful to Jodi Myers and Jeanne Basom for their ceaseless helpfulness. Special thanks as well to Kellie Geldreich for her patient and thorough assistance in helping me navigate the Graduate School's policies and procedures. Additionally, I am very grateful to the Pufendorf Institute at Lund University in Lund, Sweden, for the opportunity to take part in the IMPROVE theme in the winter of 2014. It was an honor to participate in discussions in such a diverse and talented interdisciplinary academic team.

It was an honor to work alongside Dr. Andrew See and to witness the skill and charm of Dr. Adam Micolich. Drs. See and Micolich are uniquely talented; their collaboration has been indispensable to me, and their guidance has made me a better scientist. I thank Dr. Billy Scannell for laying the foundation for the thermal cycling experiments, for introducing me to fractal analysis and low-temperature experimentation, and for his patient tenacity through long nights of troubleshooting. I thank Dr. Ted Martin for his invaluable assistance in understanding the InGaAs/InP material system through clear and detailed e-mail correspondences.

It has been a true pleasure to work alongside soon-to-be-Dr. Rick Montgomery, whose enthusiasm, skill, and gregarious spirit I've admired for as long as I've known him. There is nobody with whom I'd have rather shared the joys and challenges of life in the Taylor Lab. I've also greatly enjoyed working alongside my lab mate Bill Watterson and to witness his development into a truly skilled and effective scientist and team leader. Special thanks to REU student Shannon Conroy, who's editing skill were great help in poofreading this dissertion.

To Mom and Dad

TABLE OF CONTENTS

Chapter Page

I. INTRODUCTION 1

1.1. Toward High-Mobility Electron Transport 1
1.2. Electron Scattering and Ballistic Electron Transport 2
1.3. Dissertation Outline 8

II. MESOSCOPIC ELECTRON TRANSPORT: PRINCIPLES AND DEVICE FABRICATION 11

2.1. Principles of High-Mobility Electron Transport 11
2.2. Low-Dimensional Electron Transport 13
2.3. Conductivity and Resistivity in Two Dimensions 17
2.4. Quantum Mechanical Treatment of Two-Dimensional Conduction in a Magnetic Field 19
2.5. Characterizing a Two-Dimensional Electron System 22
2.6. Semiconductor Heterostructures and Electron Billiards 25
2.7. Electron Billiards 26
2.8. Magnetoconductance Fluctuations 35
2.9. Low-Temperature Measurement 42

Chapter Page

III. FRACTALS 47

3.1. On Self-Similarity and Dimension 47

3.2. Motivating the Fractal Dimension 50

3.3. Time-Series Fractal Structures 59

3.4. Fractal Analysis of Time-Series Traces: Beyond Box-Counting 61

3.5. Evaluating Fractal Analysis Techniques 69

3.6. Relationship between Fractal Dimension and Spectral Exponent 75

3.7. Generating and Characterizing Fractional Brownian Motions 76

IV. FRACTAL ANALYSIS OF MCF TRACES 88

4.1. Generating Simulated Traces 89

4.2. Analyzing the Simulated Traces 93

4.3. Identifying Correspondences 93

4.4. Assessing Scale Plot Pairs 96

V. THERMAL STABILITY OF ELECTRON CONDUCTION 102

5.1. Description of Experiment 102

5.2. Preliminary Results 108

5.3. Refinement of Correlation Analysis of AlGaAs/GaAs Billiards 110

5.4. Interpreting τ and η 116

Chapter Page

5.5. Refining the Data Set 118

5.6. Adding Data from Induced Billiard Devices 122

5.7. Interpretation of Fit Parameters 126

5.8. Charge Transfer and MCF Correlation in the InGaAs/InP Heterostructure 132

VI. CONCLUSIONS 143

APPENDICES

A. GENERALIZING MCF CORRELATION FIT FUNCTION 146

B. NORMALIZED SCALE PLOTS FROM CHAPTER IV ANALYSIS 149

REFERENCES CITED 156

LIST OF FIGURES

Figure Page

1.1. Moore's Law plots the exponential increase in the number of transistors in integrated circuits. 1

1.2. Illustrating three regimes of electron transport in two dimensions. . . . 3

1.3. Visualizing three classes of potential profiles in electron billiards. 7

2.1. The allowed energy states of an electron in a two-dimensional system of dimensions $L_x \times L_y$ visualized as the vertices of a grid in $\vec{k}$-space. . 14

2.2. Electron energy states in $\vec{k}$-space at absolute zero. 15

2.3. Comparing the densities of states for free electrons in two dimensions and electrons in the presence of a magnetic field. 21

2.4. Hall bar geometry for electrical measurements. 22

2.5. Shubnikov-de Haas and Hall effect measurements performed on a 2DEG in a Hall bar geometry. 25

2.6. Schematic of the band bending that occurs at the interface between aluminum gallium arsenide and gallium arsenide. 26

2.7. Schematic of the AlGaAs/GaAs heterostructure. 28

2.8. Modeling the conduction band structure of the AlGaAs/GaAs modulation-doped heterostructure. 29

2.9. Scanning electron micrograph of Ti/Au gates deposited on the AlGaAs/GaAs heterostructure used in this work. 29

2.10. Schematic of the InGaAs/InP heterostructure. 31

2.11. Band diagram for the InGaAs/InP heterostructure. 31

2.12. Comparison of the confinement potential profiles created using electrostatic depletion in the AlGaAs/GaAs system and wet etching in the InGaAs/InP system. 33

2.13. Schematic of the undoped $Al_{0.33}Ga_{0.67}As$/GaAs heterostructure. 34

Figure Page

2.14. Scanning electron micrographs of the undoped electron billiard devices labeled AS57N and AS61N. 35

2.15. Schematic of the experimental setup proposed in [1] to demonstrate the effect of the magnetic vector potential on the phase of the electronic wave function. 37

2.16. Sweeping the magnitude of a magnetic field applied perpendicular to an electron billiard which supports two distinct electron trajectories results in an interference pattern with a periodicity inversely related to the enclosed area S. 39

2.17. Sweeping the magnitude of a magnetic field applied perpendicular to an electron billiard which supports very many distinct electron trajectories results in an interference pattern with a spectral content reflecting the wide range of areas enclosed by phase-coherent electron trajectory loops. 39

2.18. Visualizing the skipping orbit regime of electron transport. 40

2.19. Correlation field B_c vs magnetic field B for determination of phase coherence length. 42

2.20. Schematic of the Oxford Instruments LLD and ^{3}He Heliox-VL Insert. . 43

2.21. Schematic of the constant-current electrical measurement setup. 45

2.22. Schematic of the constant-voltage electrical measurement setup. 46

3.1. The Sierpinski Carpet exhibits spatial exact self-similarity. 48

3.2. The initial six iterations of the construction of the Cantor set. 48

3.3. The first three iterations in the generation of the Peano curve. 50

3.4. Evaluating the length of the coastline of Britain at different levels of precision. 52

3.5. Defining the similarity dimensions of trivially self-similar Euclidian shapes. 53

3.6. The Koch Curve is an example of an exact self-similar structure with a non-integer similarity dimension. 54

3.7. Applying the box-counting method to the Koch curve. 55

3.8. Visualizing the effect of shifting box locations. 59

Figure Page

3.9. Daily closing prices for a single stock from December 1980 to October 1996. 61

3.10. Statistical self-affinity in a fractal time-series trace. 62

3.11. Magnetoresistance fluctuations recorded in an electron billiard device can provide examples of exact self-affinity in time-series structures. 62

3.12. Visualizing a variational box-counting method applied to stock price data. 63

3.13. Time-series traces with Hurst exponents of $H = 0.25$, 0.50, and 0.75. . 65

3.14. Visualizing the application of Dubuc's variance method at two distinct values of ϵ. 68

3.15. Visualizing the adaptive fractal analysis method. 70

3.16. The cumulative sum of Gaussian white noise results in Brownian motion. 72

3.17. Deriving a relationship between the Hurst exponent and fractal dimension. 74

3.18. Results of fractal analysis on colored noise traces generated with a specified power spectral density β. 76

3.19. Results of a Monte Carlo analysis of the fidelity of the four fractal analysis methods in determining the H value for randomly-generated 16384-point fBm traces. 79

3.20. Results of a Monte Carlo analysis of the fidelity of the four fractal analysis methods in determining the H value for randomly-generated 512-point fBm traces. 80

3.21. Comparison of a 512-point fBm trace with $H_{\text{in}} = 0.5$ before and after Fourier filtering to a minimum feature size of 10 points. 81

3.22. Results of a Monte Carlo analysis of the fidelity of the four fractal analysis methods in determining the H value for randomly-generated 512-point fBm traces Fourier filtered to a minimum feature size of 10 points. The analyses are performed over 1.01 orders of magnitude in length scale. 82

3.23. Results of a Monte Carlo analysis of the fidelity of the four fractal analysis methods in determining the H value for randomly-generated 512-point fBm traces Fourier filtered to a minimum feature size of 10 points. The analyses are performed over 0.71 orders of magnitude in length scale. 83

3.24. Comparison of scaling plots produced by the variational box-counting method applied to a 512-point fBm trace with $H_{\text{in}} = 0.5$ before and after Fourier filtering to a minimum feature size of 10 points. 84

3.25. Comparison of scaling plots produced by the variance method applied to a 512-point fBm trace with $H_{\text{in}} = 0.5$ before and after Fourier filtering to a minimum feature size of 10 points. 85

3.26. Comparison of scaling plots produced by the Dubuc variation method applied to a 512-point fBm trace with $H_{\text{in}} = 0.5$ before and after Fourier filtering to a minimum feature size of 10 points. 86

3.27. Comparison of scaling plots produced by the adaptive fractal analysis method applied to a 512-point fBm trace with $H_{\text{in}} = 0.5$ before and after Fourier filtering to a minimum feature size of 10 points. 87

4.1. Magnetoconductance fluctuations measured on modulation-doped and induced electron billiards. 90

4.2. A comparison of the six MD-MCF traces under consideration and their simulated counterparts. 95

4.3. A comparison of the six UD-MCF traces under consideration and their simulated counterparts. 96

5.1. MCF traces recorded on the AlGaAs/GaAs electron billiard back-to-back while the billiard is held at $T = 240$ mK. 104

5.2. MCF traces recorded on the InGaAs/InP electron billiard back-to-back while the billiard is held at $T = 240$ mK. 105

5.3. Comparison of MCF from the InGaAs/InP billiard measured at $T = 240$ mK after being warmed to three intermediate temperatures T_i. . . . 106

5.4. Comparison of MCF from the AlGaAs/InP billiard measured at $T = 240$ mK after being warmed to three intermediate temperatures T_i. . . . 107

Figure Page

5.5. Fitting the functional form of Equation 5.4 to the MCF correlation data taken on the modulation-doped AlGaAs/GaAs billiard, the modulation-doped InGaAs/InP billiard, and a uniformly-doped GaAs wire. 109

5.6. MCF measured on the AlGaAs/GaAs billiard on six distinct cooldowns from room temperature, and fractional Brownian motion traces, processed and selected to share statistical properties with the corresponding MCF 114

5.7. A plot of F_2 vs T_i for MCF recorded on the AlGaAs/GaAs system and a fit to the data based on a slight alteration to Equation 5.4. 115

5.8. A plot of F_2 vs T_i for the AlGaAs/GaAs billiards. 118

5.9. A plot of F_2 vs T_i for the AlGaAs/GaAs billiards. 119

5.10. A plot of fractal dimension vs the quantity Q for seven different billiard devices fabricated in the AlGaAs/GaAs heterostructure. 120

5.11. A plot of F_2 vs T_i for the AlGaAs/GaAs billiards. 121

5.12. Comparison of MCF traces taken on an electron billiard device in the undoped $Al_{0.33}Ga_{0.67}As$/GaAs heterostructure before and after a thermal cycle to room temperature. 122

5.13. A plot of F_2 vs T_i for the AlGaAs/GaAs billiards, the induced device AS57N, and the induced device AS61N. 125

5.14. A schematic of the slowly-varying electrostatic potential landscape induced in the plane of a 2DEG by ionized dopant atoms located above the plane of the 2DEG. 126

5.15. Conduction band diagram for the AlGaAs/GaAs heterostructure system. 128

5.16. Configuration coordinate diagram for the DX center in Si-doped n-$Al_{0.33}Ga_{0.67}As$. 129

5.17. Band diagram for the InGaAs/InP heterostructure. 133

5.18. Comparison of the MCF correlation data for the InGaAs/InP billiards using the correlation functions given by Equation 5.1 and Equation 5.5. 134

Figure Page

5.19. Comparison of the MCF correlation data for the InGaAs/InP billiards using the correlation functions given by Equation 5.1 and Equation 5.5, as well as the fits provided by Equation 5.4 and Equation 5.7 using the parameters published in Ref. [2]. 135

5.20. Normalized 2DEG density vs billiard temperature before and after illumination; MCF correlation data vs intermediate temperature for the InGaAs/InP billiard. 137

5.21. Mobility as a function of temperature for the InGaAs/InP billiard device. 138

5.22. Normalized 2DEG density vs billiard temperature after illumination. . 139

5.23. Post-illumination 2DEG density as a function of time at a constant temperature of $T = 120$ K. 140

A.1. Characterizing the heating and cooling rates for an electrical sample in the cryostat. 148

LIST OF TABLES

Table Page

2.1. Summary of typical values of physical quantities characterizing electron billiards in the three material systems. 36

4.1. Collecting and averaging the q values found based on the three fractal analyses. 98

4.2. Average values for Δq found by averaging across all traces in each trace group, listed by fractal analysis technique. 100

5.1. Values of the thermally-activated characteristic time for electron migration τ at several temperatures. 132

CHAPTER I

INTRODUCTION

1.1. Toward High-Mobility Electron Transport

In the decades since John Bardeen, Walter Brattain, and William Shockley developed the transistor in 1947, the technology world has witnessed the inexorable march toward ever smaller solid-state devices. The exponential rate at which the number of transistors populating integrated circuits increases is known as Moore's Law [3], and is displayed in Fig. 1.1.

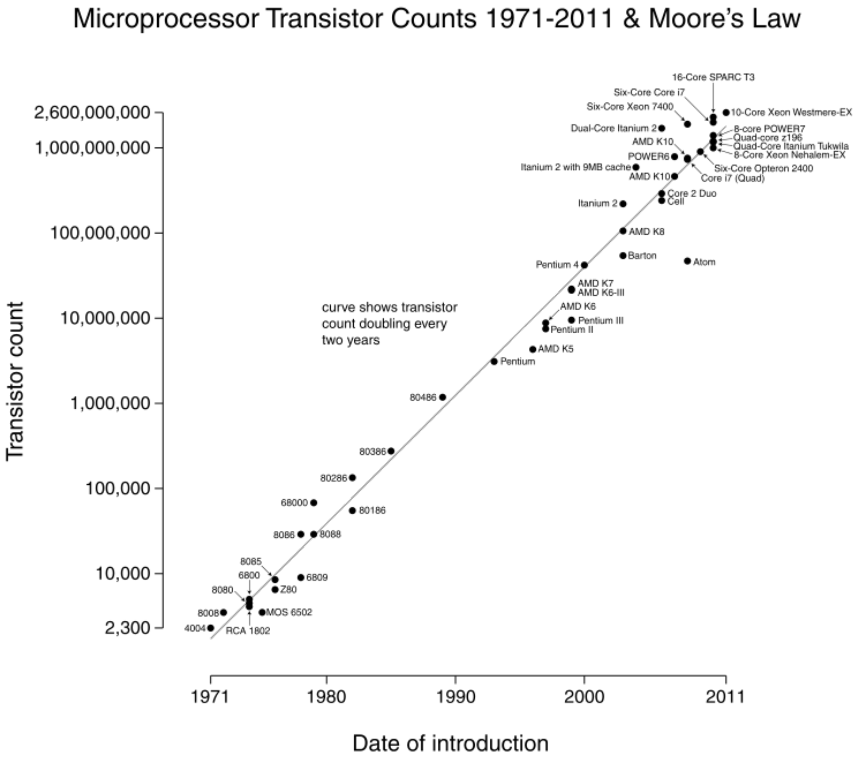

FIGURE 1.1. Moore's Law plots the exponential increase in the number of transistors found in integrated circuits. Image licensed under Creative Commons CC BY-SA 3.0 (creativecommons.org/licenses/by-sa/3.0/us) by Wikipedia contributor Wgsimon.

In spite of the remarkable tenacity of Moore's Law, it is likely unreasonable to expect that this trend will persist indefinitely—as transistors approach the atomic scale, fundamental physical constraints will prevent the further shrinking of devices. Nonetheless, even if we presume ourselves to be reaching fundamental size limits, there exists much active research regarding the optimization of transistor technologies.

One significant avenue of semiconductor device optimization, and one which serves as a guiding theme in this dissertation, pertains to the trajectories of electrons as they traverse a solid-state device. In abandoning cumbersome electron vacuum tubes in favor of their solid-state counterparts, we have also abandoned the elegance of ballistic electron transport in a vacuum for the disordered and circuitous electron paths typically found in metals and semiconductors. Is it possible to reclaim the efficiency of electron transport unperturbed by scattering events in solid-state devices? To address this question, we must first establish a vocabulary regarding electron transport.

1.2. Electron Scattering and Ballistic Electron Transport

In the ideal case, electrons traverse a conducting material via straight-line paths that only deviate upon reflection from an intentionally-designed feature, as is the case for an electron traveling in vacuum; such transport is termed 'ballistic' (see Fig. 1.2). In solid-state materials, however, electrons encounter a variety of impediments to ideal ballistic transport—impurities, phonons, and electrostatic potentials serve to scatter the electrons from their initial path. Such perturbations can be greatly mitigated, however—modern semiconductor fabrication techniques allow for the growth of a nearly perfect crystal lattice free of impurities, and phonon scattering is effectively eliminated at sub-Kelvin experimental temperatures.

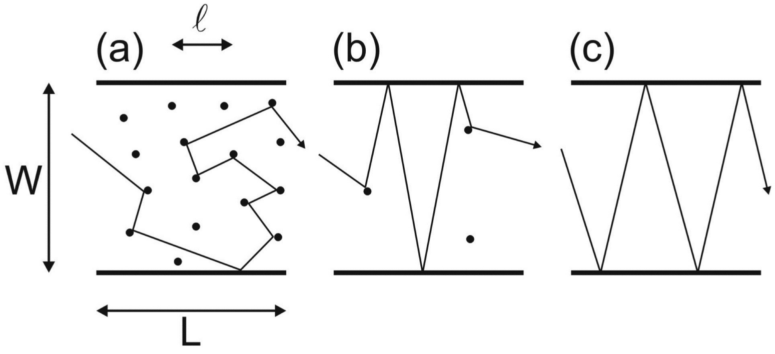

FIGURE 1.2. Illustrating three regimes of electron transport in two dimensions. (a) If the mean free path ℓ is smaller than the conducting area's dimensions W and L, the conduction is called diffusive. (b) If $L > \ell > W$, transport is known as quasi-ballistic. (c) If the mean free path ℓ exceeds the device dimensions, such that electrons follow straight-line trajectories until encountering intentionally defined boundaries, transport is known as ballistic. From Ref. [4].

The extent to which these scattering events perturb the motion of an electron may be represented by the mobility mean free path ℓ_μ, which measures the average distance traversed by an electron before encountering a large-angle scattering event. If the mean free path exceeds the dimensions of the conducting region, the electron is often said to undergo ballistic transport, in analogy to transport through vacuum. Such a definition assumes that small-angle scattering events have a negligible impact on the dynamics of electron transport; the ideal case of true ballistic transport, however, requires the absence of both large- and small-angle scattering events. The prospect of realizing ballistic electron transport in semiconductor devices holds considerable interest for both fundamental and applied physics—in particular, the study of electron transport in the semiclassical regime can harness the Aharonov-Bohm effect [1, 5] (see Section 2.8) as a probe of quantum chaos [6–9].

1.2.1. Electron Billiards: An Experimental Test Bed

The experimental investigations discussed in this dissertation pertain primarily to electron motion in a two-dimensional potential well at a semiconductor interface. While such systems may in principle be made arbitrarily large, a study of electron transport dynamics is simplified by constraining electron motion to a small portion of the plane. In particular, the electronic systems considered here typically involve confining electrons to an approximately 1 µm × 1 µm square with quantum point contacts serving as entry and exit ports; such devices are known as electron billiards, whose fabrication and properties are detailed in Section 2.7. The Fermi wavelength of an electron in a billiard device is many times smaller than the billiard size at roughly 50 nm; as a result, electrons may be idealized as traveling in straight-line paths through the billiard until experiencing a scattering event or specular reflection from the billiard walls. Furthermore, at low temperature, an electron may remain phase-coherent as it traverses a billiard device, so that the net conduction through the billiard derives from the quantum interference of the electronic wave functions as they exit the billiard. Our studies treat electron billiards almost exclusively in this semiclassical regime, in which we may harness quantum mechanical effects as a probe of electron dynamics while considering a distribution of classical trajectories.

Given that the billiard dimensions are typically smaller than the mean free path ℓ_μ, one might feel justified in considering scattering events within the billiard to be negligible. As we shall see, however, the elimination of large-angle scattering events is not sufficient to ensure true ballistic electron transport.

The primary means of investigating electron transport employed in this dissertation involves the measurement of the fluctuating conductance through an electron billiard as a function of the magnitude of an applied magnetic field. These fluctuations are known as magnetoconductance fluctuations (MCF), and are described in Section 2.8. The measured conduction through a billiard will depend on the quantum interference of the collection of phase-coherent electron trajectories through the billiard; the application of a magnetic field yields a systematic shift in the relative phases of these electrons through the Aharonov-Bohm effect, such that the precise form of an MCF trace may serve as a "fingerprint" of the precise distribution of electron trajectories through the billiard.

In the case of true ballistic electron transport, we would then expect the distribution of electron trajectories through the billiard, and hence the form of a measured MCF trace, to depend on the billiard geometry alone in a predictable and measurable manner. As an example, consider the relative properties of a circular billiard and a stadium-shaped billiard (i.e., two half-circles connected by straight lines): the classical trajectories through the stadium are chaotic, in the sense that two nonidentical but initially similar trajectories will diverge exponentially in time, while the trajectories through the circle are stable. Employing a theoretical framework set forth by Jalabert *et al.* [10], prior experimental studies by Marcus *et al.* [6] have claimed to be able to distinguish between such billiards based on the spectral content of MCF traces measured on each device. Such a claim, however, rests on the assumption that electron transport in billiard devices is indeed ballistic.

In reality, we cannot say for certain whether ballistic electron transport has been achieved based solely on mobility mean free path measurements. These measurements are heavily biased toward large-angle scattering events, with the implicit assumption that small-angle scattering events are negligible with respect to the distribution of electronic trajectories within a billiard. These small-angle scattering events are an inevitable consequence of the modulation doping method of heterostructure fabrication, which introduces a spatial separation between the conducting plane and the ionized dopants used to populate the conducting plane with electrons (see Section 2.6). The modulation doping method thus yields a conduction plane that remains prone to scattering from the electrostatic potentials of remote ionized impurities. Topinka *et al.* [11] cite this soft potential landscape as the mechanism for their observed branching of electron flow within an AlGaAs/GaAs heterostructure system, which they note is a purely classical phenomenon. Their work, as well as the experimental findings presented in this dissertation, suggest that the potential landscape induced by remote ionized impurities plays a very substantial role in determining the electron trajectories in electron billiard devices.

This potential landscape may be eliminated, however, in electron billiard devices which populate a two-dimensional conducting plane with electrons without the use of dopant atoms. These ‘undoped’ electron billiards, characterized in depth by Drs. Andrew See and Adam Micolich at the University of New South Wales, employ a positively biased, degenerately-doped n^+-GaAs cap on an AlGaAs/GaAs heterostructure to electrostatically induce the conduction electrons to populate the heterostructure interface.

1.2.2. Fractals and Electron Billiards

Additionally, an investigation of the fractal properties of MCF measured on electron billiard devices allows for a probe of electron dynamics within the billiard. Generally speaking, the term ‘fractal’ may be understood to denote a pattern which exhibits structure on a variety of size scales; a rigorous discussion is provided in Chapter III. In the case of MCF, a fractal structure denotes a trace which exhibits fluctuations at a wide range of scales in magnetic field. Fractal structures were originally observed in MCF by R. P. Taylor *et al.* [8] and by A. P. Micolich *et al.* [12], and subsequently and independently by A. S. Sachrajda *et al.* [13].

Dr. Roland Ketzmerick has demonstrated [14] that MCF traces measured on billiards characterized by a mixed phase space supporting both chaotic and stable trajectories will generally be fractal, such that a fractal analysis of these traces can reveal details regarding the nature of this phase space. It is understood that a mixed phase space may result from the two-dimensional geometry of the billiard as well as the gradient of the potential barriers used to form the billiard. But what about the small-angle scattering introduced by remote ionized donors? Do these have sufficient influence on the phase space within a billiard to alter these fractal characteristics? Ketzmerick argued that they do not, claiming that "[a]s long as the *elastic* scattering can be modeled by smooth impurity potentials it will not change the generic properties of the mixed phase space" [14] (emphasis in original).

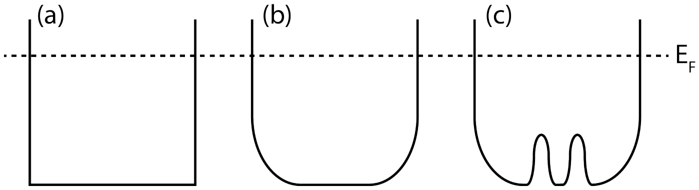

FIGURE 1.3. Visualizing three classes of potential profiles in electron billiards. The dashed line represents the Fermi energy in the billiard. (a) A 'hard-walled' billiard, which will support only stable electron trajectories unless the billiard geometry is designed so as to introduce chaos. (b) A 'soft-walled' billiard, which will yield a mixed phase space and hence fractal MCF. (c) A soft-walled billiard with an additional potential landscape introduced by remote ionized donors.

Figure 1.3 schematically portrays the question at hand. This figure displays three classes of potential profiles within the electron billiard: panel (a) shows a billiard defined by 'hard-walled' potentials, in which only the billiard geometry could introduce chaos to the phase space; panel (b) shows a billiard defined by 'soft-walled' potentials, which Ketzmerick notes will lead to a mixed phase space and hence the observation of fractal MCF. Panel (c), on the other hand, portrays the potential profile of a modulation-doped electron billiard, which exhibits both soft walls and small-angle scatterers. We hypothesize that the potential landscape introduced by remote ionized impurities may in fact yield a measurable difference in the fractal qualities of MCF measured on a modulation-doped billiard. To test this hypothesis, we conduct an investigation of the fractal properties of MCF traces measured on both the modulation-doped and undoped AlGaAs/GaAs electron billiards, with the expectation that the modulation-doped billiards should yield MCF with a more pronounced fractal structure.

1.3. Dissertation Outline

This dissertation is presented as follows:

Chapter II describes the theory of electron transport in two dimensions. Following a quantum mechanical description of electron transport in the presence of an applied magnetic field, we describe the semiconductor heterostructure devices known as electron billiards on which our experimental measurements are made. Finally, we discuss the technical details of low-temperature electrical measurements.

Chapter III discusses fractal structures, both as spatial and time-series structures. We discuss a variety of techniques for characterizing fractal structures, and discuss the complications that can arise when applying these techniques to structures found in nature which may exhibit a limited range of scaling properties. The nature of these difficulties is studied systematically through the application of the fractal analysis techniques discussed to computer-generated fractal structures under a variety of conditions.

Chapter IV investigates of the fractal properties of MCF measured in both modulation-doped and undoped AlGaAs/GaAs electron billiards, with the aim of concluding whether one set of fluctuations is demonstrably more fractal than the other. Given that the modulation-doping technique is hypothesized to yield a potential landscape that serves to introduce chaos to the electrons' phase space, we expect MCF traces measured on the modulation-doped billiard to exhibit a more pronounced fractal character than those measured on the undoped billiard. Our results, however, fail to support this hypothesis; we instead find that MCF traces measured on each billiard exhibit similar fractal characteristics, and that a rigorous comparison is hindered by the limited scaling range exhibited in these traces.

Chapter V describes an investigation of the thermal stability of MCF measured on electron billiard devices. While Chapter IV demonstrates that remote ionized donors do not impact the phase space in AlGaAs/GaAs electron billiards in a detectible way, we seek to probe and understand the way in which these ionized donors affect the individual electron trajectories within the billiard. We describe an experimental procedure in which MCF traces are recorded before and after thermal cycles of the electron billiards to various intermediate temperatures, which serve to rearrange the potential profile in the plane of the 2DEG. The temperature-dependent decorrelation of MCF traces is quantified and fitted to a model which describes the charge transfer process hypothesized to be responsible for the decorrelation in both the AlGaAs/GaAs and InGaAs/InP material systems. These results serve to demonstrate that electron trajectories in modulation-doped electron billiards are highly sensitive to the charge distribution among the ionized dopants, such that these devices do not support true ballistic electron transport.

Finally, the dissertation concludes with a summary of our findings and suggestions of avenues for future research

CHAPTER II

MESOSCOPIC ELECTRON TRANSPORT: PRINCIPLES AND DEVICE FABRICATION

2.1. Principles of High-Mobility Electron Transport

Electron transport through a system of disordered atoms subject to thermal lattice vibrations is in general intractably complex on the subatomic scale—a fully quantum-mechanical description of electronic transport through such a system would require an understanding of the precise configuration of all atoms in the system as well as the individual wave functions for each of an Avogadro's number of electrons. In such cases, which are representative of electron transport in traditional metal wires at room temperature, conductance is necessarily described as the net motion of the collection of electrons, with a net current density proportional to the strength of the applied electric field $\vec{E}$: $\vec{J} = \sigma \vec{E}$, where σ is known as the conductivity of the system. We can further relate the current density to the mean velocity of electrons in the system through $\vec{J} = en_e\vec{v}_d$, where $e = |e|$ is the charge of a single electron, n_e denotes the number of electrons participating in the conduction, and $\vec{v}_d$ is the average velocity of conduction elections, known as the drift velocity. Combining these expressions for current density yields

$$\sigma = en_e \left| \frac{v_d}{E} \right| = en_e\mu_m. \qquad \text{(Equation 2.1)}$$

The quantity μ_m, which represents the proportionality between the electronic drift velocity and the magnitude of the applied electric field, is known as the electron mobility.

For a given applied electric field, the electron mobility is thus limited by those factors which limit the electronic drift velocity—namely, such factors as thermal vibrations and the inhomogeneity of the atomic lattice. One method for improving electron mobility, then, is to eliminate the atomic lattice entirely and harness electron conduction in a vacuum, as is the case in electron vacuum tubes. In such a system, a fully quantum-mechanical description of electron transport is tractable; however, the elegance of this solution is undermined by the technical considerations that make such a solution impractical for everyday usage, such as the volume and mass of electron vacuum systems relative to solid-state electronics. As a result, there is considerable technological interest in optimizing a solid-state conductive material such that thermal perturbations are negligible and momentum-randomizing scattering events are minimized. Such a system is now realizable with modern semiconductor fabrication technology such as molecular beam epitaxy (MBE) and metal-organic vapor phase epitaxy (MOVPE), which allow for the deposition of a high-purity semiconductor device one atomic monolayer at a time, resulting in a near-perfect crystal lattice.

In principle, even a perfect crystal lattice does little to ameliorate the difficulties of a fully quantum-mechanical description of charge transport in a solid-state device, since the wave function $\Psi(\vec{x})$ for any given electron would need to account for the potential introduced by every atomic nucleus and non-conducting electron comprising the conductive system. However, the translational symmetry introduced by a perfect lattice allows us to derive a semiclassical solution for the electronic wave function in which the effect of the atomic lattice is entirely accounted for through an adjustment of the electron's effective mass. In the fully quantum-mechanical approach, we would seek electron wave functions $\Psi(\vec{x})$ which satisfy $\hat{H}\Psi(\vec{x}) = \epsilon\Psi(\vec{x})$, where

$\hat{H} = \hat{p}^2/2m + U(\vec{x})$. In a perfectly periodic potential landscape $U(\vec{x})$, the electronic wave functions will be of the form $\Psi(\vec{x}) = e^{\imath \vec{k}\cdot\vec{x}}u(\vec{x}) = \psi(\vec{x})u(\vec{x})$, where $\vec{k}$ is the wave vector. Such a wave function—a plane wave modulated by a periodic function $u(\vec{x})$ which encapsulates the periodicity of the lattice—is known as a Bloch wave. Applying the Schrödinger equation to a Bloch wave function and assuming a parabolic dispersion relation $\epsilon_n(\vec{k})$ for small $\vec{k}$ yields

$$\hat{H}\psi(\vec{x}) = -\frac{\hbar^2}{2m^*}\vec{\nabla}^2\psi(\vec{x}) + V(\vec{x})\psi(\vec{x}) = \epsilon_n\psi(\vec{x}), \qquad \text{(Equation 2.2)}$$

where

$$m^* = \frac{\hbar^2/m_0}{\partial^2\epsilon_n(k)/\partial k^2} \qquad \text{(Equation 2.3)}$$

is the electron's effective mass (with m_0 as the electron's rest mass), $V(\vec{x})$ represents the potential experienced by the electron due to any defects in the lattice (in the absence of an external field), and ϵ_n represents the single-electron energy. We may thus describe electron wave functions in a near-perfect crystal lattice as equivalent to plane waves traveling in a vacuum with an effective mass m^* which depends on the material properties of the crystal lattice.

2.2. Low-Dimensional Electron Transport

Through careful band engineering (discussed below), it is possible to fabricate solid-state devices in which the generally three-dimensional electron wave functions are confined to its lowest-energy bound states in a single dimension (typically labeled as the $\hat{z}$ direction) such that electron transport takes place in two dimensions. In addition to simplifying device architecture and reducing the number of scattering impurities in the conducting region, low-dimensional electron transport may introduce novel physical properties. For instance, in two dimensions, the density of states is energy-independent. To understand why this is the case, consider a planar region of area $A = L_x L_y$, in which the allowed quantum mechanical wave vectors are $k_x = 2\pi n_x / L_x$ and $k_y = 2\pi n_y / L_y$, where n_x and n_y are integers. In such a system, an electron's energy state may be fully characterized by the parameters n_x and n_y, such that its energy state may be represented as a point on a grid in $\vec{k}$-space (see Fig. 2.1).

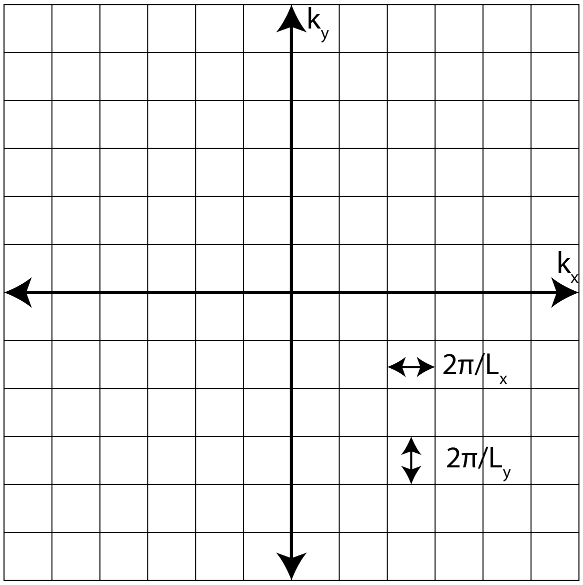

FIGURE 2.1. The allowed energy states of an electron in a two-dimensional system of dimensions $L_x \times L_y$ may be visualized as the vertices of a grid in $\vec{k}$-space.

In the low-temperature limit, electrons will minimize their energy $E = \hbar^2 \vec{k}^2 / 2m^*$; however, as fermions, no two electrons in the same spin state may be characterized by wave functions with identical values of both k_x and k_y, such that each location on the grid in k-space may be occupied by at most two electrons (one for each spin state). Thus, electrons will populate the allowed states in $\vec{k}$-space in a way that minimizes their distance from the origin while obeying the Pauli exclusion principle; in two dimensions, this corresponds to the electron energy states forming a circle in

$\vec{k}$-space whose radius k_F is known as the Fermi energy E_F (measured relative to the conduction band minimum) [15]; see Fig. 2.2.

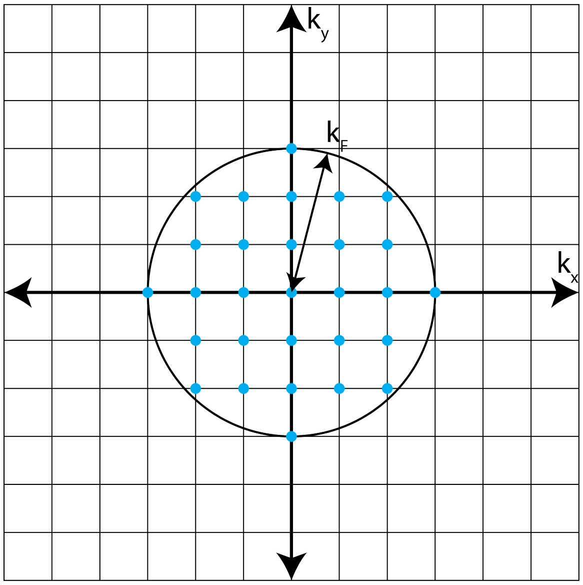

FIGURE 2.2. Electron energy states in $\vec{k}$-space at absolute zero. At absolute zero, electron energy states populate $\vec{k}$-space in such a way that they fill a Fermi circle with radius k_F.

Thus, at absolute zero, all energy states with $|\vec{k}| = \sqrt{k_x^2 + k_y^2} \leq k_F$ will be filled (with a spin degeneracy of two). As a result, we may express the Fermi energy as a function of the total number of available states N in the system: $N(k_F) = k_F^2 A/2\pi$. More generally, for $k \leq k_F$ and using $E(k) = \hbar^2 k^2/2m^*$, the number of available energy states with energy no greater than $E(k)$ is $N(E, A) = m^* E A/\pi\hbar^2$. The density of states (DOS) for an arbitrary system represents the number of available energy states per unit volume and per unit energy, and so may generally be calculated as

$$g(E) = \frac{1}{A}\frac{\partial N(E, A)}{\partial E}. \qquad \text{(Equation 2.4)}$$

In the two-dimensional case, this simplifies to

$$g_{2D}(E) = \frac{m^*}{\pi\hbar^2}. \qquad \text{(Equation 2.5)}$$

Thus, notably, the two-dimensional density of states is independent of energy. (For comparison, the densities of states in the one- and three-dimensional cases scale as $E^{-1/2}$ and $E^{1/2}$, respectively). The carrier density of any electronic system may be calculated as $n_s = \int_0^\infty g(E)f(E)dE$, where

$$f(E) = \frac{1}{e^{(E-E_F)/k_BT} + 1} \qquad \text{(Equation 2.6)}$$

is the Fermi-Dirac distribution which gives the probability of an electron at temperature T occupying an energy state E. In the low-temperature limit, $E_F \gg k_BT$, and $f(E)$ may be approximated by the step function $\Theta(E - E_F)$. Hence, for the 2D density of states obtained above and in the low-temperature limit, we find

$$n_s = \int_0^{E_F} \frac{m^*}{\pi\hbar^2} dE = \frac{m^* E_F}{\pi\hbar^2}, \qquad \text{(Equation 2.7)}$$

where n_s is the two-dimensional electron sheet density. Thus, in two dimensions and at low temperature, we find a direct proportionality between the electron density and Fermi energy.

In the low-temperature limit, all electrons that contribute to conduction processes possess an energy very near the Fermi energy E_F, since the lowest available energy states are also very near E_F [16]; this allows for a straightforward derivation of physical quantities characterizing their wave functions. For instance, the Fermi wavenumber corresponding to the Fermi energy is given by

$$\begin{aligned} E_F &= \frac{\hbar^2 k_F^2}{2m^*} \\ k_F &= \frac{1}{\hbar}\sqrt{2m^* E_F} \\ &= \sqrt{2\pi n_s}. \end{aligned} \qquad \text{(Equation 2.8)}$$

Since the velocity $\vec{v}$ corresponding to a wave vector $\vec{k}$ is given by $\vec{v} = \hbar\vec{k}/m$, the velocity of electrons contributing to conduction is related to the carrier density as

$$v_F = \frac{\hbar\sqrt{2\pi n_s}}{m^*}, \qquad \text{(Equation 2.9)}$$

and the Fermi wavelength of these electrons is thus

$$\lambda_F = \frac{2\pi}{k_F} = \sqrt{\frac{2\pi}{n_s}}. \qquad \text{(Equation 2.10)}$$

2.3. Conductivity and Resistivity in Two Dimensions

We have previously defined the conductivity σ of a material as the proportionality constant that satisfies $\vec{J} = \sigma\vec{E}$, such that σ is a scalar quantity and $\vec{J} \parallel \vec{E}$. In the presence of a magnetic field, it is no longer true that $\vec{J} \parallel \vec{E}$, and it is necessary to replace the scalar σ with the conductivity tensor $\boldsymbol{\sigma}$, such that in two dimensions we have:

$$\begin{pmatrix} J_x \\ J_y \end{pmatrix} = \begin{pmatrix} \sigma_{xx} & \sigma_{xy} \\ \sigma_{yx} & \sigma_{yy} \end{pmatrix} \begin{pmatrix} E_x \\ E_y \end{pmatrix}. \qquad \text{(Equation 2.11)}$$

Equation 2.11 describes the response of the two-dimensional current density to a two-dimensional electric field (perhaps in the presence of a magnetic field, whose effect is encapsulated in the conductivity tensor); inverting this equation gives the field response to a current density via the resistivity tensor $\boldsymbol{\rho}$:

$$\begin{pmatrix} E_x \\ E_y \end{pmatrix} = \begin{pmatrix} \rho_{xx} & \rho_{xy} \\ \rho_{yx} & \rho_{yy} \end{pmatrix} \begin{pmatrix} J_x \\ J_y \end{pmatrix}, \qquad \text{(Equation 2.12)}$$

where

$$\boldsymbol{\rho} = \boldsymbol{\sigma}^{-1} = \frac{1}{\sigma_{xx}^2 + \sigma_{xy}^2} \begin{pmatrix} \sigma_{yy} & -\sigma_{yx} \\ -\sigma_{xy} & \sigma_{xx} \end{pmatrix}. \qquad \text{(Equation 2.13)}$$

We may determine the components of the conductivity and resistivity tensors by considering the Drude model of conduction, which asserts that, in the steady state, the momentum gained by a system of electrons due to their interaction with electric and magnetic fields must be precisely balanced by the momentum lost due to scattering processes [17], such that

$$\left(\frac{d\vec{p}}{dt}\right)_{\text{scattering}} = \left(\frac{d\vec{p}}{dt}\right)_{\text{fields}}. \qquad \text{(Equation 2.14)}$$

If we introduce the momentum relaxation time τ_m, we may then write

$$\frac{m^* \vec{v}_d}{\tau_m} = e\left(\vec{E} + \vec{v}_d \times \vec{B}\right), \qquad \text{(Equation 2.15)}$$

where $\vec{v}_d$ is the electrons' drift velocity. This vector equation may be rewritten as a tensor equation as

$$\begin{pmatrix} E_x \\ E_y \end{pmatrix} = \begin{pmatrix} \frac{m^*}{e\tau_m} & -B \\ B & \frac{m^*}{e\tau_m} \end{pmatrix} \begin{pmatrix} v_x \\ v_y \end{pmatrix}; \qquad \text{(Equation 2.16)}$$

rewriting further in terms of $\vec{J} = e\vec{v}_d n_s$, we have

$$\begin{aligned}\begin{pmatrix} E_x \\ E_y \end{pmatrix} &= \begin{pmatrix} \frac{m^*}{e\tau_m} & -B \\ B & \frac{m^*}{e\tau_m} \end{pmatrix} \begin{pmatrix} \frac{J_x}{en_s} \\ \frac{J_y}{en_s} \end{pmatrix} \\ &= \sigma^{-1} \begin{pmatrix} 1 & -\mu B \\ \mu B & 1 \end{pmatrix} \begin{pmatrix} J_x \\ J_y \end{pmatrix}, \end{aligned} \qquad \text{(Equation 2.17)}$$

where $\sigma \equiv en_s\mu$ and $\mu \equiv e\tau_m/m^*$. Hence, the elements of the conductivity and resistivity tensors are given by

$$\rho_{xx} = \rho_{yy} = \sigma^{-1} \qquad \text{(Equation 2.18)}$$

and

$$\rho_{yx} = -\rho_{xy} = \mu B/\sigma = B/en_s, \qquad \text{(Equation 2.19)}$$

together with Equation 2.13.

2.4. Quantum Mechanical Treatment of Two-Dimensional Conduction in a Magnetic Field

In the presence of a nonzero magnetic field, the Hamiltonian for free electrons must be modified to include a contribution from the magnetic vector potential $\vec{A}$. In the Landau gauge, the magnetic vector potential corresponding to a magnetic field $\vec{B} = B\hat{z}$ is $\vec{A} = (0, Bx, 0)$, and the Hamiltonian for free electrons confined to the $x-y$ plane becomes

$$\hat{H} = \frac{(\vec{p} + e\vec{A})^2}{2m^*} = \frac{\hat{p}_x^2 + (\hat{p}_y + eB\hat{x})^2}{2m^*}. \qquad \text{(Equation 2.20)}$$

Since an electron traveling at a velocity $\vec{v}$ in the presence of a magnetic field $\vec{B}$ will experience a Lorentz force $\vec{F} = e(\vec{v} \times \vec{B})$, the electron will begin moving in a circular path. By equating the centripetal force mv^2/r to the magnitude of the Lorentz force eBv, we may derive the angular frequency of this circular motion $\omega_c = eB/m$, known as the cyclotron frequency. We may then express Equation 2.20 as follows:

$$\hat{H} = \frac{\hat{p}_x^2}{2m^*} + \frac{1}{2}m^*\omega_c^2\left(\hat{x} - \frac{\hbar k_y}{m^*\omega_c}\right)^2. \qquad \text{(Equation 2.21)}$$

Comparing Equation 2.21 to the Hamiltonian for the quantum harmonic oscillator

$$\hat{H}_{QHO} = \frac{\hat{p}^2}{2m} + \frac{1}{2}m\omega^2\hat{x}^2, \qquad \text{(Equation 2.22)}$$

we find that the Hamiltonian of an electron in a perpendicular magnetic field matches that of a quantum harmonic oscillator with a potential minimum shifted by $\hbar k_y/m^*\omega_c$ whose energy levels are given by $E_n = \hbar\omega_c(n + 1/2)$ $(n = 1, 2, 3, \ldots)$. Thus, whereas a system of free electrons confined to two dimensions exhibits an energy-independent density of states, the available energy states for the same system in the presence of a perpendicular magnetic field are discretized into states known as Landau levels [17] separated in energy by $\hbar\omega_c$; see Fig. 2.3. Under the approximations of zero temperature and a perfect crystal lattice, the Landau levels take the form of a series delta-functions in a plot of density of states vs energy; however, electron scattering induced by finite temperature and lattice imperfections results in a broadening of these levels. It is nonetheless instructive to consider these energy levels as delta-functions, such that the density of states in the presence of a perpendicular magnetic field $\vec{B}$ can be written

$$g_B(E) = \frac{2eB}{h} \sum_n \delta(E - E_n). \qquad \text{(Equation 2.23)}$$

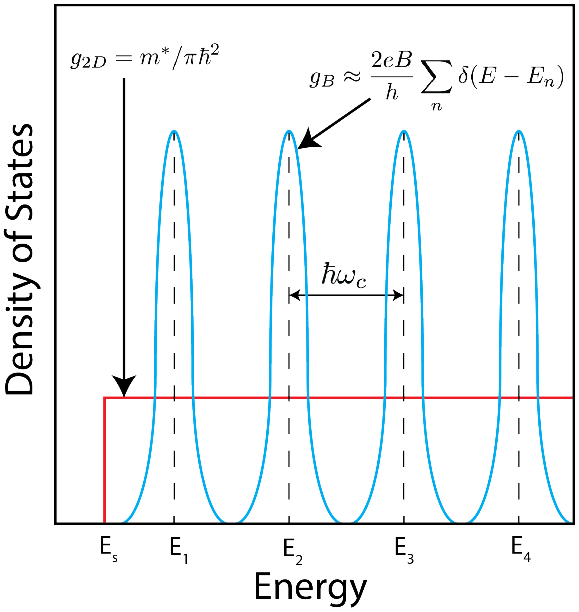

FIGURE 2.3. Comparing the densities of states for free electrons in two dimensions (red) and electrons in the presence of a magnetic field (blue).

Given that the sheet density of electrons n_s must be independent of the applied magnetic field, the integral of $g_B(E)$ over all $E \leq E_F$ must return the same value n_s regardless of the value of B. Hence, the degeneracy of each Landau level changes with magnetic field such that each Landau level contributes a value of $2eB/h$ to the total electron density, which motivates the introduction of the filling factor

$$\nu = \frac{hn_s}{2eB} \qquad \text{(Equation 2.24)}$$

which indicates the number of Landau levels that are completely filled at a magnetic field B and electron sheet density n_s. Thus, for a given sheet density n_s, increasing the magnitude of a perpendicular magnetic field will lead to a decrease in the filling factor ν such that each filled Landau level must account for a greater proportion of the total n_s.

2.5. Characterizing a Two-Dimensional Electron System

Consider a two-dimensional conducting region in the geometry shown in Fig. 2.4; this geometry is known as a Hall bar [17] owing to its utility in observing the Hall effect, described below.

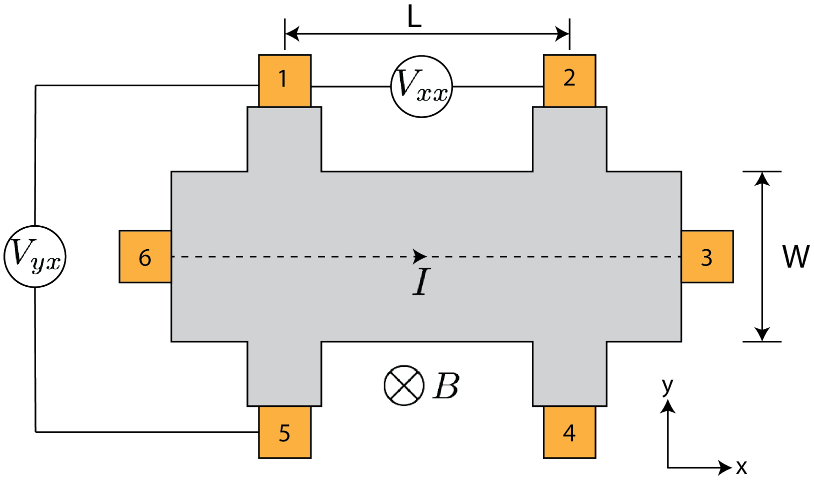

FIGURE 2.4. Hall bar geometry for electrical measurements. The numbered yellow squares represent electrical leads, while the grey area represents the active region for electron conduction. A typical characterization measurement consists of passing a current $\vec{I}$ through the Hall bar (here, from lead 6 to lead 3) and applying a perpendicular magnetic field $\vec{B}$, and measuring the longitudinal voltage drop $V_{xx} = V_2 - V_1$ and the transverse voltage drop $V_{yx} = V_5 - V_1 = V_H$.

When a current $\vec{I}$ is applied through the length of the Hall bar, the y-component of the current density $\vec{J}$ is zero, and Equation 2.19 becomes

$$\begin{pmatrix} E_x \\ E_y \end{pmatrix} = J_x \begin{pmatrix} (en_s\mu)^{-1} \\ B(en_s)^{-1} \end{pmatrix}. \qquad \text{(Equation 2.25)}$$

The current density J_x is simply related to the current I and Hall bar width A as $I = J_x W$, and the electric field components E_x and E_y are related to the respective voltage drops V_{xx} and V_{yx} and the Hall bar dimensions as $E_x = V_{xx}/L$ and $E_y = V_{yx}/W$. We may thus express Equation 2.25 as:

$$V_{xx} = \frac{L}{W}\frac{I}{en_s\mu}, \qquad \text{(Equation 2.26)}$$

$$V_{yx} = \frac{IB}{en_s}. \qquad \text{(Equation 2.27)}$$

Therefore, the electron sheet density n_s and the electron mobility μ may be determined through measurements of the longitudinal voltage drop V_{xx} and the transverse voltage drop V_{yx} as a function of B and at a given current I.

The above derivations of n_s and μ predict that V_{xx} is constant with respect to magnetic field and that V_{yx} increases linearly with magnetic field. While these classical arguments are true to good approximation at low magnetic field, higher magnetic fields uncover the quantum mechanical nature of the electron energy levels through the previously discussed Landau levels. Consider Fig. 2.3; while the locations in energy space and the densities of states represented by the Landau levels vary with the magnetic field B, the Fermi energy E_F remains at a constant value. In the context of the filling factor ν, we may say that the density of states at the Fermi energy is a minimum when ν is an integer, while the density of states at E_F is a maximum at half-integer values of ν (i.e., $\nu = n + 1/2$ where n is an integer), such that E_F lies in the middle of a half-filled Landau level. Because conduction occurs from states very near the Fermi energy, the longitudinal resistivity ρ_{xx} falls to zero when the density of states at the Fermi energy is zero, and reaches a maximum when the density of states at E_F is maximized. Thus, as an applied magnetic field is increased, a measurement of ρ_{xx} will exhibit oscillations that fall to zero at magnetic fields corresponding to integer values of ν; this phenomenon is known as the Shubnikov-de Haas (SdH) effect [17].

Indeed, whereas the Hall effect as described by Equation 2.27 provides a measurement of the electron sheet density n_s based on purely classical arguments, the periodicity of the SdH oscillations provides a quantum mechanical probe of this quantity: From Equation 2.24, we see that a plot of ν vs $1/B$ is expected to be linear with a slope corresponding to n_s. In practice, it is simpler to determine this electron density by employing the Hall effect, as this measurement does not require high magnetic fields. Nonetheless, measurements of SdH oscillations are valuable for identifying the presence of conduction via a plane parallel to the intended plane of electrons—if parallel conduction is present, a nonzero longitudinal resistivity ρ_{xx} will remain at magnetic fields corresponding to integer values of ν.

The transverse resistivity ρ_{yx} also exhibits a quantum mechanical structure at high magnetic fields: Comparing Equation 2.27 to Equation 2.24, we may write

$$R_{yx}^{-1} = \nu \frac{2e^2}{h}; \qquad \text{(Equation 2.28)}$$

that is, the transverse conductance increases in steps of the conductance quantum $2e^2/h$ as ν is increased (which corresponds to a decrease in magnetic field), such that a plot of R_{xy} vs B will exhibit plateaus of constant resistance centered on values of B corresponding to integer filling factors, separated by steps in resistance of $h/2e^2$. This phenomenon is known as the (integer) quantum Hall effect [17]. Figure 2.5 provides examples of the Shubnikov-de Haas and integer quantum Hall effects as measured in an AlGaAs/GaAs heterostructure.

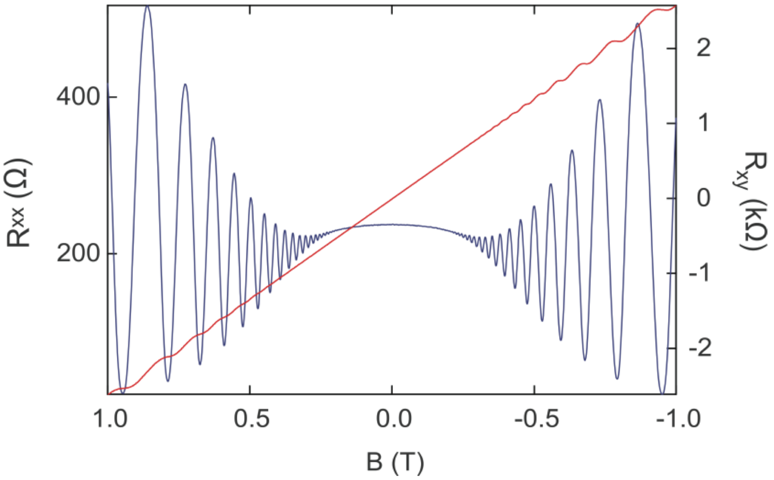

FIGURE 2.5. Shubnikov-de Haas (blue, left axis) and Hall effect (red, right axis) measurements performed on a 2DEG in a Hall bar geometry. Measurements performed by Drs. Andrew See and Adam Micolich at the University of New South Wales using the AlGaAs/GaAs heterostructure featured in the studies described in Chapters IV and V. From Ref. [18].

2.6. Semiconductor Heterostructures and Electron Billiards

When semiconductor materials with different band gaps are brought together in an atomically smooth planar interface, electrons from the larger band gap material migrate to the lower conduction band of the smaller band gap material, establishing an electric potential difference that serves to bend the conduction and valence bands. The result is a roughly triangular potential well whose one-dimensional bound state energies may be calculated; see Fig. 2.6. If the first bound state is the only state whose energy lies below the Fermi energy E_F, electrons will be confined to this energy state and will only be free to move in the two dimensions of the interfacial plane; such a system is known as a two-dimensional electron gas (2DEG), as the electrons in the plane may be approximated as noninteracting and freely-propagating particles [17].

The electron density in the 2DEG may be increased by doping the higher-band-gap material with an electron-donor species. However, this increase in electron density

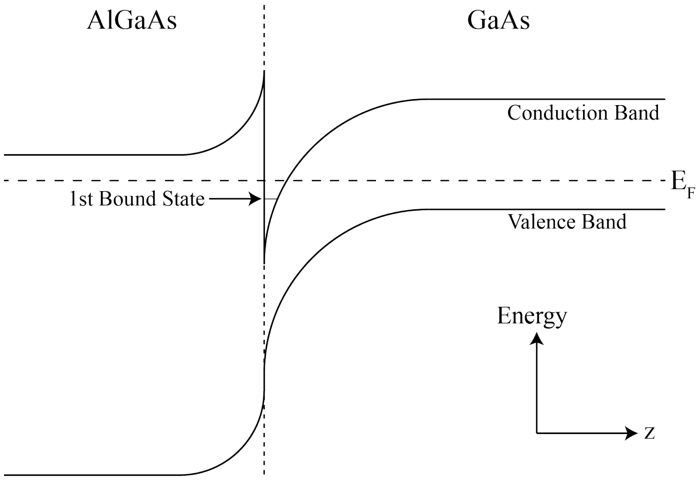

FIGURE 2.6. Schematic of the band bending that occurs at the interface between aluminum gallium arsenide and gallium arsenide. The vertical axis represents energy; the horizontal axis represents the distance z in the heterostructure growth direction. The difference in the band gaps of these materials leads to bending of the conduction and valence bands so as to preserve a constant Fermi energy throughout the material, resulting in the formation of a potential well in which electrons may collect.

comes at the cost of a decrease in the electron mobility, due to increased Coulombic scattering off the ionized donor atoms which lie in close proximity to the plane of the 2DEG. This issue may be mitigated by introducing an undoped spacer layer of the higher-band-gap material between the doped layer and the plane of the 2DEG. This technique, known as modulation doping [19] (see Fig. 2.7), results in a decrease in the carrier density in the 2DEG, but does succeed in significantly increasing the mobility of those electrons in the 2DEG.

2.7. Electron Billiards

Having confined a system of electrons to two kinetic degrees of freedom, we may further confine the electrons within the plane of the 2DEG by defining potential barriers. In particular, the electronic systems considered here typically involve confining electrons to an approximately 1 µm × 1 µm square within a Hall bar channel;

such devices are known as electron billiards. Electrons enter and exit such devices through narrow constrictions known as quantum point contacts (QPCs), which serve to further confine electrons to one-dimensional quantum modes [20, 21]. In this dissertation, we primarily investigate electron billiards fabricated in two distinct material systems, the aluminum gallium arsenide/gallium arsenide (AlGaAs/GaAs) heterostructure and the indium gallium arsenide/indium phosphide (InGaAs/InP) heterostructure, in which electron billiards are defined using distinct techniques.

2.7.1. $\mathrm{Al}_x\mathrm{Ga}_{1-x}\mathrm{As/GaAs}$ Electron Billiards

The study of electron billiard devices has its roots in the aluminum gallium arsenide/gallium arsenide heterostructure system, commonly denoted $\mathrm{Al}_x\mathrm{Ga}_{1-x}\mathrm{As/GaAs}$, where x denotes the mole fraction of aluminum arsenide in the AlAs/GaAs alloy. Studies of 2DEGs in AlGaAs/GaAs heterostructures frequently employ a value $x = 0.33$, which ensures that the AlGaAs band gap is direct (as is the case for $x < 0.45$) and that the AlGaAs and GaAs lattice parameters are closely matched while maintaining the band gap difference necessary for the formation of a 2DEG [22].

The AlGaAs/GaAs devices discussed in this dissertation were fabricated on a single wafer labeled C2275 grown at the Cavendish Laboratory by Drs. Ian Farrer and David Ritchie. The wafer was grown using molecular beam epitaxy (MBE) and consists of (in order of deposition) a GaAs base layer, a 20 nm undoped $\mathrm{Al}_{0.33}\mathrm{Ga}_{0.67}\mathrm{As}$ spacer layer, a 40 nm n-$\mathrm{Al}_{0.33}\mathrm{Ga}_{0.67}\mathrm{As}$ layer doped with silicon at a concentration of 1.20×10^{18} cm^{-3}, and a 10 nm GaAs cap layer; see Fig. 2.7. This heterostructure results in a 2DEG electron density n_s of 2.4×10^{11} cm^{-2} and electron mobility of 3.89×10^{5} cm^{2}/Vs, as reported by the fabrication facility. The resulting conduction band profile, provided by Dr. Alex Hamilton of the University of New South Wales, is modeled using a one-dimensional Poisson solver program[1], and is displayed in Fig. 2.8. The electron billiards studied in this work were fabricated on this wafer at the Semiconductor Nanofabrication Facility (SNF) by Drs. Andrew See and Adam Micolich.

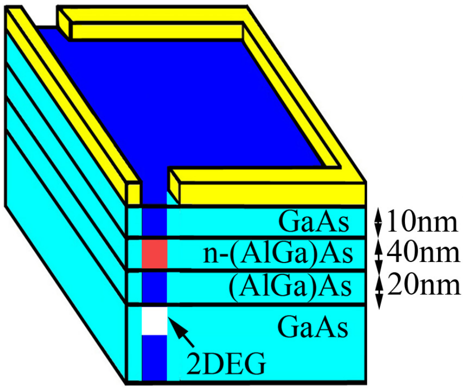

FIGURE 2.7. Schematic of the AlGaAs/GaAs heterostructure. A 2DEG (white) forms at the interface between the undoped AlGaAs spacer layer and the GaAs layer. The doped AlGaAs layer (red) contains a Si donor density of 1.2×10^{18} cm^{-3}. The billiard walls (light blue) are electrostatically defined by surface gates (yellow). From Ref. [2].

In the AlGaAs/GaAs heterostructure, a conducting region is defined within the 2DEG by depositing patterned metallic gates on the surface. Applying a negative voltage to these gates results in a depletion of the 2DEG in the regions under the gate, allowing for the formation of billiards of arbitrary size. Furthermore, since the precise profile of the electrostatic depletion depends on the magnitude of the negative bias applied to the surface gates, adjustment of this bias allows for the fine-tuning of the size of a billiard on a given device. Figure 2.9 displays the patterned gates defining a square electron billiard on one of the two nominally identical devices studied here as imaged using a scanning electron microscope.

---

[1] These data were produced using the software package HETMOD, an internal IBM Poisson solver. Similar software is available as freeware at Dr. Gregory Snider's Web site at www3.nd.edu/ gsnider/.

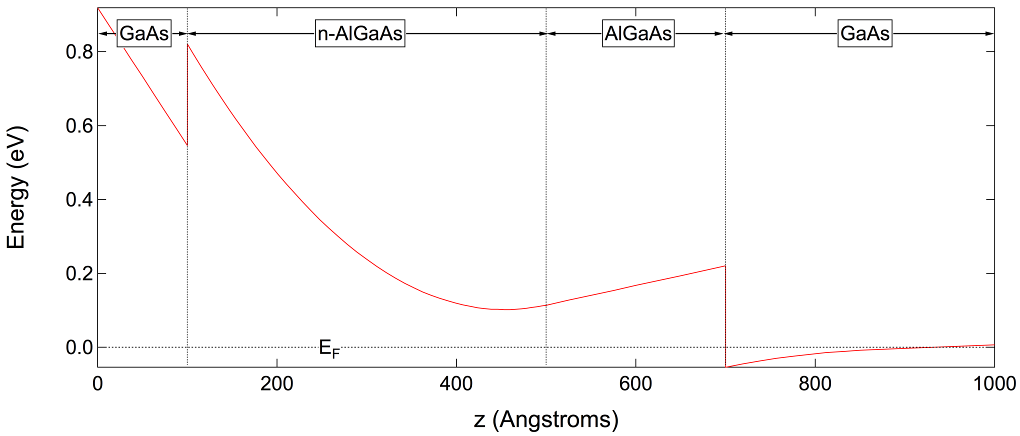

FIGURE 2.8. Modeling the conduction band structure of the AlGaAs/GaAs modulation-doped heterostructure. The vertical axis represents energy; the horizontal axis represents the distance z in the heterostructure growth direction. Data produced using a one-dimensional Poisson solver and provided by Dr. Alex Hamilton.

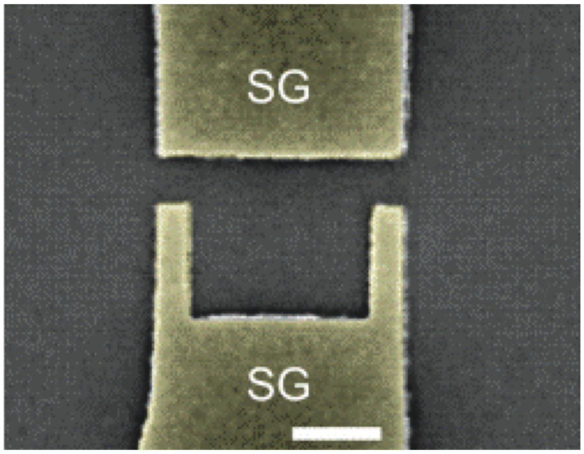

FIGURE 2.9. Scanning electron micrograph of Ti/Au gates deposited on the AlGaAs/GaAs heterostructure used in this work. The gaps separating the gates form the quantum point contacts that serve as entry and exit ports for electrons in the 2DEG. The lithographic dimensions of the electron billiard are 1.09 µm × 1.06 µm. The gate deposition consisted of 10 nm Ti and 30 nm Au. Scale bar is 0.5 µm. From Ref. [18].

Because the surface gates which serve to define the conducting region are spatially removed from the conducting plane, the electrostatic potential profile edge is not perfectly normal to the conducting plane; instead, the confinement potential exhibits 'soft' walls; see Fig. 2.12 below. Additionally, because the billiard is only defined when a negative voltage is applied to the surface gates, it is necessary to calibrate this voltage prior to measurement. With increasing (negative) voltage, the area of the billiard will shrink in such a way that the QPCs serving as entry and exit ports for the billiards will eventually ‘pinch off’ and the billiard will become nonconducting. In practice, our measurements on the AlGaAs/GaAs electron billiards described in Chapter V employed a gate voltage corresponding to a zero-field conductance through the device of $3 \times 2e^2/h$, such that the QPCs contain six transverse modes.

2.7.2. $\mathbf{In_{1-x}Ga_xAs/InP}$ Electron Billiards

The indium gallium arsenide/indium phosphide (denoted InGaAs/InP) devices discussed in this dissertation were fabricated by Dr. Ivan Shorubalko at the University of Lund in Lund, Sweden. The fabrication process employed metal-organic vapor phase epitaxy (MOVPE) on a substrate of semi-insulating InP:Fe and consist of (in order of deposition) a 50 nm buffer layer of InP, a 9 nm $In_{0.75}Ga_{0.25}As$ layer which forms a quantum well, a 20 nm undoped InP spacer layer, a ∼1 nm layer of n-InP doped with silicon at a concentration of $\sim 5 \times 10^{18}$ cm^{-3}, and a 20 nm undoped InP cap layer. Additionally, the heterostructure is capped with a 1 μm thick layer of photoresist used in defining the electron billiard (see below) and finally a uniform Ti/Au top gate; see Fig. 2.10

The band diagram for the InGaAs/InP system is displayed in Fig. 2.11. Unlike the AlGaAs/GaAs system, in which the 2DEG is formed in the triangular potential well near the AlGaAs/GaAs interface, the InGaAs/InP system supports a 2DEG in the quantum well resulting in the InGaAs layer sandwiched by the larger-band-gap InP layers. At sufficiently low temperature and a sufficiently narrow InGaAs layer, there exists only one bound state with energy lower than the Fermi energy, allowing

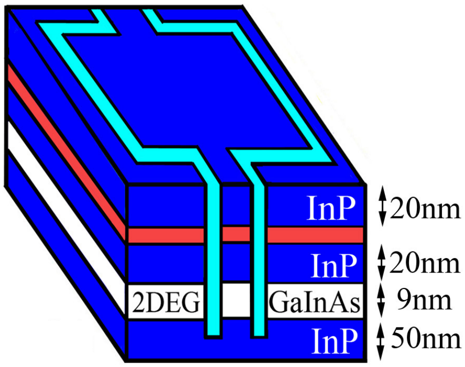
InP
20nm
InP
20nm
2DEG
GaInAs
9nm
InP
50nm

FIGURE 2.10. Schematic of the InGaAs/InP heterostructure. A 2DEG (white) forms in the InGaAs layer. A 1 nm thick δ-doped InP layer (red) contains a Si donor density of 5×10^{18} cm^{-3}. The billiard walls (light blue) are defined by etched trenches. From Ref. [2].

for the formation of a 2DEG in which electrons are prohibited from propagating in the transverse direction.

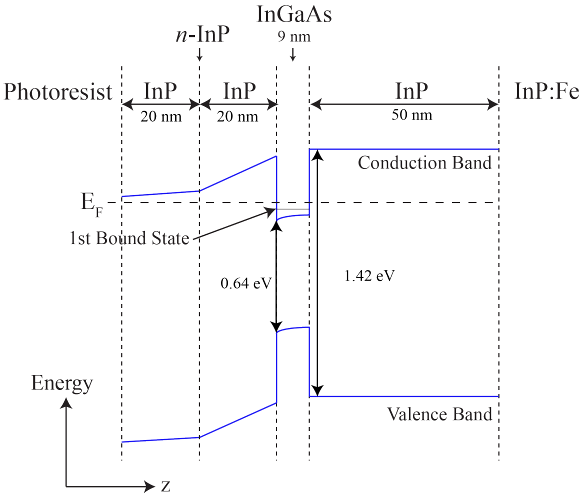
InGaAs
9 nm
n-InP
Photoresist
InP
20 nm
InP
20 nm
InP
50 nm
InP:Fe
Conduction Band
E_F
1st Bound State
0.64 eV
1.42 eV
Energy
Valence Band
z

FIGURE 2.11. Band diagram for the InGaAs/InP heterostructure. The vertical axis represents energy; the horizontal axis represents the distance z in the heterostructure growth direction.

The lattice constant of $\mathrm{In}_{1-x}\mathrm{Ga}_x\mathrm{As}$ varies with the mole fraction x and matches that of InP at $x = 0.47$, such that many studies are performed on the $\mathrm{In}_{0.53}\mathrm{Ga}_{0.47}\mathrm{As}$/InP system to avoid mechanical strain. By contrast, the $\mathrm{In}_{0.75}\mathrm{Ga}_{0.25}\mathrm{As}$ alloy used in this work was chosen to optimize low-temperature electron mobility [23].

Due to the InGaAs/InP lattice mismatch, the InGaAs layer is highly strained, and its heterostructure thickness of 9 nm matches the critical thickness above which lattice dislocations will form [24].

The material content of the InGaAs/InP heterostructure system allows for the fabrication of electron billiards using techniques other than electrostatic depletion of the 2DEG. Specifically, unlike the AlGaAs/GaAs system, whose aluminum content quickly oxidizes when exposed to atmosphere, the InGaAs/InP system allows for billiard formation using chemical etching techniques. Using a combination of electron beam lithography and a non-selective, 70 nm deep, HBr-based wet etching, electron billiards may be formed by physically removing material at the plane of the 2DEG. To electrically isolate the heterostructure from the Ti/Au top gate, the etched trenches are subsequently filled in with a 1 µm thick insulating layer of Shipley 1813 photoresist, which is deposited onto the heterostructure and hard-baked for stability. This procedure results in a potential gradient at the plane of the 2DEG that is an order of magnitude steeper than in the AlGaAs/GaAs heterostructure due to the 2DEG's proximity of surface charges on the etched boundary relative to the spatially separated surface gates in the AlGaAs/GaAs architecture [25]; see Fig. 2.12.

Unlike the AlGaAs/GaAs electron billiards, no calibration procedure is necessary to ensure that the electron billiard dimensions and conducting profile are constant between experimental runs on the InGaAs/InP system. While properties of the InGaAs/InP heterostructure such as 2DEG electron density and conduction band profile may be modified via a voltage applied to the top gate, our studies described in Chapter V are performed with this top gate held at ground.

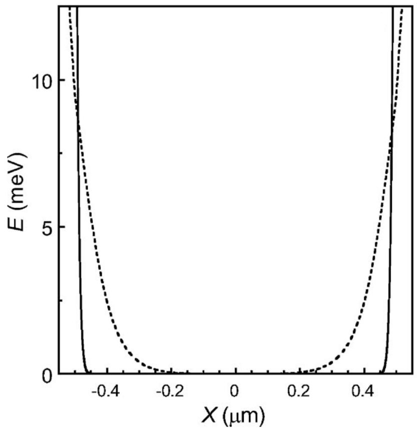

FIGURE 2.12. Comparison of the confinement potential profiles created using electrostatic depletion in the AlGaAs/GaAs system (dashed line) and wet etching in the InGaAs/InP system (solid line). The vertical axis represents electrostatic potential energy; the horizontal axis represents the spatial location relative to the billiard's center. The profiles are based on simulations of the potential energy in a cross section through the billiard's central region. From Ref. [25].

2.7.3. Electron Billiards in Undoped AlGaAs/GaAs Heterostructures

As a means to further reduce the effect of remote ionized impurity scattering on electron dynamics in a 2DEG, it is also possible to create a 2DEG in a semiconductor heterostructure without relying on dopants to provide the conduction electrons. While there exist a variety of heterostructure architectures which accomplish this, the devices discussed in this work follow the design described in Ref. [26] as studied by Drs. Andrew See and Adam Micolich at the University of New South Wales [18, 27]. In this architecture, a n^+-GaAs cap layer, degenerately doped at a density of 3.3×10^{18} cm^{-3} so as to exhibit metallic conductivity at low temperature, serves as a gate at low temperatures to induce electrons to populate the potential well at an $Al_{0.33}Ga_{0.67}As$/GaAs interface deeper in the heterostructure; see Fig. 2.13.

The application of a positive bias to the n^+-GaAs gate allows for the tuning of electron density and mobility, with typical values of roughly 2×10^{11} cm^{-2} and

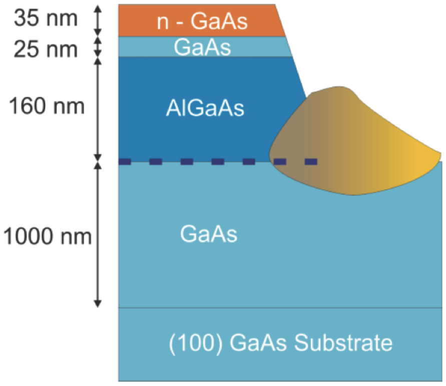

FIGURE 2.13. Schematic of the undoped $Al_{0.33}Ga_{0.67}As/GaAs$ heterostructure. A positive bias applied to a degenerately doped n^+-GaAs cap (orange) induces the formation of a 2DEG (dashed line) at the AlGaAs/GaAs interface. The NiGeAu Ohmic contact (yellow) must be formed such that it is overlapped by the n^+-GaAs gate but is electrically isolated from the gate. The heterostructure is grown on a semi-insulating (100) GaAs substrate. Figure from Ref. [18].

300×10^3 cm^2/Vs, respectively. The electron density in the cap layer is sufficient to screen the 2DEG from the electrostatic forces of the ionized donors in the cap [28].

The undoped AlGaAs/GaAs electron billiard devices described in this work were fabricated by Dr. See at the Semiconductor Nanofabrication Facility (SNF) and the University of New South Wales node of the Australian National Fabrication Facility (ANFF). The AlGaAs/GaAs wafer, labeled NBI30, was grown by Drs. Martin Aagesen and Poul Lindelof at the Niels Bohr Institute in Copenhagen, Denmark. Scanning electron micrographs of the devices studied here, labeled AS57N and AS61N, are provided in Fig. 2.14.

2.7.4. Summary of Electron Billiard Properties

Table 2.1 lists typical values for the parameters characterizing the electron billiards discussed in this dissertation. Electron density and mobility are determined using a measurement of the Hall voltage as described by Equation 2.27; electron

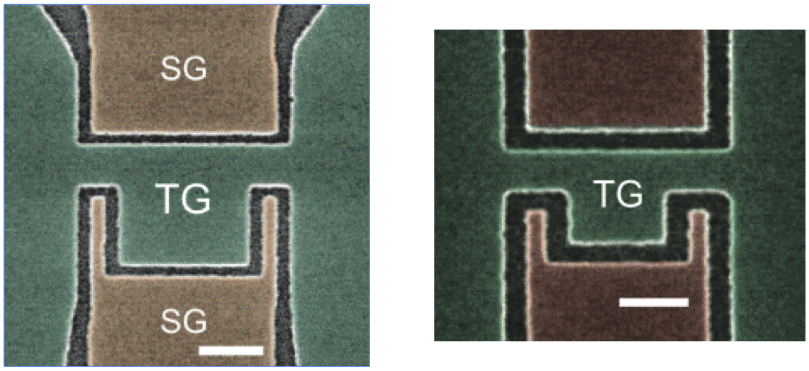

AS57N AS61N

FIGURE 2.14. Scanning electron micrographs of the undoped electron billiard devices labeled AS57N (left) and AS61N (right). The devices are identical aside from the billiard dimensions: AS57N has billiard dimensions 1.33 µm × 1.23 µm; AS61N has billiard dimensions 0.74 µm × 0.66 µm. Both scale bars are 0.5 µm. From Ref. [18].

phase coherence length is determined using a correlation field analysis as described in Section 2.81 and Ref. [29]; mobility mean free path is determined through the relation $\ell_\mu = v_F \tau_\mu$, where v_F is the Fermi velocity and τ_μ is related to the mobility through $\tau_\mu = \mu m^*/e$.

2.8. Magnetoconductance Fluctuations

Recall from Section 2.4 that the Hamiltonian of an electron in a nonzero magnetic field may be written as

$$\hat{H} = \frac{(\vec{p} + e\vec{A})^2}{2m^*}, \qquad \text{(Equation 2.29)}$$

where the magnetic vector potential $\vec{A}$ is defined through $\vec{B} = \vec{\nabla} \times \vec{A}$. In addition to the aforementioned quantization of energy levels in a magnetic field, this leads to an electronic wave function whose phase ϕ evolves as

$$\Delta\phi = -\frac{e}{\hbar} \int \vec{A} \cdot d\vec{\ell}. \qquad \text{(Equation 2.30)}$$

Quantity	Units	Modulation-Doped AlGaAs/GaAs	Modulation-Doped InGaAs/InP	Undoped AlGaAs/GaAs
E_F	meV	8.2	41	8.2
n_s	cm^{-2}	2.3×10^{11}	6.8×10^{11}	2.3×10^{11}
μ	$\mathrm{cm}^{-2}/\mathrm{Vs}$	3.3×10^{5}	3.3×10^{5}	3.7×10^{5}
ℓ_μ	µm	2.7	4.5	3.4
ℓ_ϕ	µm	3.5	5.9	10.4
m^*/m_e	—	0.067	0.040	0.067

TABLE 2.1. Summary of typical values of physical quantities characterizing electron billiards in the three material systems. The quantities tabulated include the Fermi energy E_F, the 2DEG electron density n_s, the electron mobility μ, the mobility mean free path ℓ_μ, the electron phase coherence length ℓ_ϕ, and the electron effective mass m^*.

That is, an electron propagating in the presence of a magnetic field $\vec{B}$ with a nonzero component normal to the direction of propagation will acquire a phase shift $\Delta\phi$ which depends on the magnitude of the field $\vec{B}$ and the orientation of the field with respect to the direction of motion. However, since the effect of the magnetic field on the electron's phase is conveyed through the magnetic vector potential $\vec{A}$, the electron need not even travel through a region of nonzero magnetic field in order to exhibit such a phase shift. As was noted by Aharonov and Bohm in 1959 [1], this remarkable result could be confirmed experimentally by directing a coherent electron beam to pass on either side of a solenoid and recombining the electron beams (see Fig. 2.15). Since the magnetic field is essentially confined to the interior of the solenoid, neither electron path passes through a region of nonzero magnetic field; however, the magnetic field inside the solenoid has an associated vector potential field in the plane of the electron propagation, such that $\int \vec{A} \cdot \vec{d\ell}$ is nonzero. Specifically, the differences in the accumulated phases of electrons traversing the top and bottom paths will be

$$\begin{aligned}\phi_2 - \phi_1 &= \frac{e}{\hbar}\oint \vec{A}\cdot d\vec{\ell} \\ &= \frac{e}{\hbar}\int_S \vec{B}\cdot d\vec{S} \\ &= \frac{e}{\hbar}BS \\ &= \frac{e}{\hbar}\Phi, \qquad \text{(Equation 2.31)}\end{aligned}$$

where S is the area enclosed by the two paths and Φ is the total magnetic flux enclosed in this area.

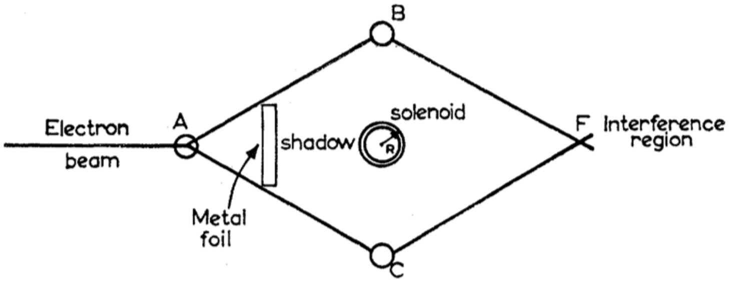

FIGURE 2.15. Schematic of the experimental setup proposed in [1] to demonstrate the effect of the magnetic vector potential on the phase of the electronic wave function. An electron traveling from point A to point F via point B or point C will experience a phase shift due to its interaction with the magnetic vector potential $\vec{A}$ corresponding to the magnetic field $\vec{B}$ inside the solenoid. For a given magnetic field, the paths ABF and ACF will yield distinct phase shifts, such that the interference at point F will depend on the magnitude of $\vec{B}$. From Ref. [1].

This result, known as the Aharonov-Bohm (A-B) Effect, is significant for its revelation of a measurable quantum mechanical effect of electromagnetic potentials on particles even in regions where no force acts on the particles. The A-B Effect is of course also present in systems in which electrons pass directly through a perpendicularly applied magnetic field, as is the case for the electron billiard devices studied in this work. Specifically, consider an electron traversing a square electron billiard device: if we let the electron traverse the billiard from left to right as in Fig. 2.16, an electron may travel from the entry QPC to the exit QPC via a single bounce off the top wall or the bottom wall with equal probability. These two possible trajectories enclose some area S, and in the presence of a magnetic field $\vec{B}$ applied perpendicular to the plane of the 2DEG, the area S will enclose a magnetic flux $\Phi = BS$. The magnitude of $\vec{B}$ will thus determine the phase relation between electrons that traverse the left and right paths such that these electrons will fall in and out of phase with a periodicity proportional to the flux quantum h/e and inversely proportional to the area S; see Fig. 2.16. Such an interference pattern may thus be experimentally observed by measuring the conductance through the billiard at a constant bias voltage as a function of the magnitude of the perpendicular field $\vec{B}$: this conduction will reach a maximum value when the electron wave functions arrive at the exit QPC in phase, and will reach a minimum value when these wave functions fall out of phase. The period in magnetic field of these oscillations is related to the total area enclosed by the phase-coherent trajectories as

$$\Delta B = \frac{h}{eA}. \qquad \text{(Equation 2.32)}$$

Of course, an electron billiard device supports many more than the two electron trajectories shown in Fig. 2.16, and each of these trajectories lends a unique contribution to the total conductance through the billiard resulting from the sum of the electron interference processes. This results in a trace of conductance as a function of magnetic field with a spectral content reflecting a wide range of areas enclosed by phase-coherent trajectory loops; see Fig. 2.17.

The resulting plot of conductance as a function of applied magnetic field is known as a magnetoconductance fluctuation (MCF) trace, and provides a wealth of

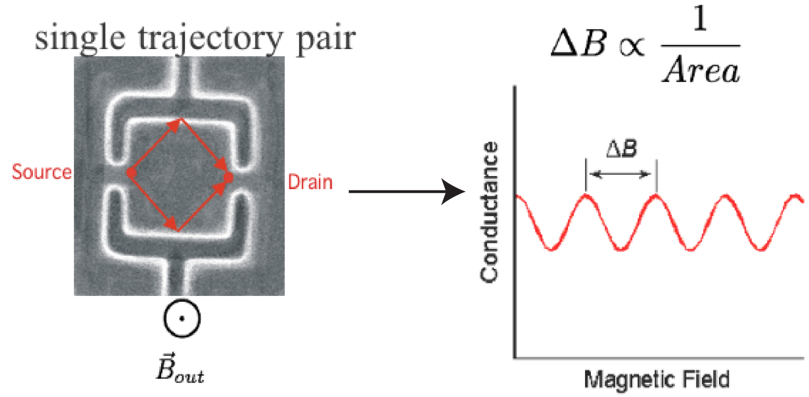
single trajectory pair
Source
Drain
$\vec{B}_{out}$
$\Delta B \propto \frac{1}{Area}$
ΔB
Conductance
Magnetic Field

FIGURE 2.16. Sweeping the magnitude of a magnetic field applied perpendicular to an electron billiard which supports two distinct electron trajectories results in an interference pattern with a periodicity inversely related to the enclosed area S. From Ref. [30].

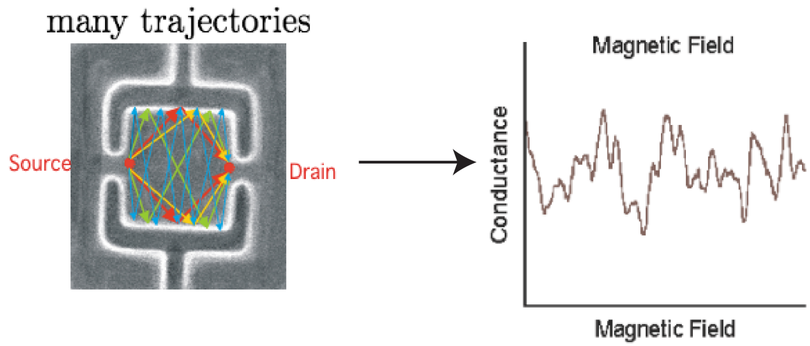
many trajectories
Source
Drain
Magnetic Field
Conductance
Magnetic Field

FIGURE 2.17. Sweeping the magnitude of a magnetic field applied perpendicular to an electron billiard which supports very many distinct electron trajectories results in an interference pattern with a spectral content reflecting the wide range of areas enclosed by phase-coherent electron trajectory loops. From Ref. [30].

information regarding the dynamics of electrons within an electron billiard device. Although it would be practically impossible to use an MCF trace to determine the precise configuration of electron trajectories within the billiard, the extreme sensitivity of the precise form of the MCF to that distribution of trajectories makes the MCF a valuable tool for probing electron dynamics in these devices.

In practice, it is customary to restrict an analysis of an MCF trace to the magnetic field range $|B| < B_{\mathrm{cyc}}$, where the cyclotron field B_{cyc} is the field at which the electron's cyclotron diameter matches the billiard width. At fields greater than B_{cyc}, electron transport through the billiard enters a 'skipping orbit' regime in which electrons traverse the billiard by skipping along the boundary; see Fig. 2.18. As the magnetic field strength increases and the cyclotron radius decreases, the electron trajectories through the billiard become less sensitive to the billiard geometry, and the MCF cease to be an effective probe of the dynamics influencing these trajectories. The cyclotron fields for the AlGaAs/GaAs and InGaAs/InP billiards, each of which has a width of 1 µm, are 160 mT and 280 mT, respectively.

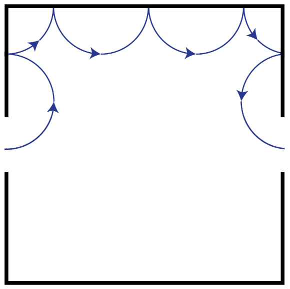

FIGURE 2.18. Visualizing the skipping orbit regime of electron transport. When the applied magnetic field exceeds the cyclotron field B_{cyc}, electrons enter a regime of transport in which trajectories skip along the billiard edge.

2.8.1. Phase Coherence Measurements

Although the skipping orbit regime of electron transport through an electron billiard is avoided for studies of electron trajectory distributions, measurements in this regime provide an effective probe of the electron's phase coherence length ℓ_{ϕ}. In the technique proposed by J. P. Bird *et al.* [29], a MCF trace $g(B)$ is measured at magnetic fields greater than roughly twice the cyclotron field B_{cyc}. They then define the correlation function

$$F(\Delta B) = \langle [g(B) - \langle g(B) \rangle][g(B + \Delta B) - \langle g(B) \rangle] \rangle, \qquad \text{(Equation 2.33)}$$

and define the 'correlation field' B_c as the value of the magnetic field which satisfies $F(B_c) = F(0)/2$. The value of the correlation field increases with increasing magnetic field B in the skipping orbit regime: in this regime, the total area enclosed by an electron trajectory which makes N_c phase coherent bounces with the billiard wall is

$$A_c = N_c \frac{\pi r_c^2}{2}, \qquad \text{(Equation 2.34)}$$

where $r_c = \hbar\sqrt{2\pi n_s}/eB$ is the cyclotron radius. The quantity N_c is related to the phase coherence length as

$$\ell_\phi = N_c \pi r_c, \qquad \text{(Equation 2.35)}$$

so we may rewrite Equation 2.34 as

$$A_c = \frac{\ell_\phi h}{2eB}\sqrt{\frac{n_s}{2\pi}}. \qquad \text{(Equation 2.36)}$$

Finally, noting that A_c is related to B_c through Equation 2.32, we may solve Equation 2.36 for ℓ_ϕ and simplify to arrive at

$$\ell_\phi = \frac{2}{(B_c/B)}\sqrt{\frac{2\pi}{n_s}}, \qquad \text{(Equation 2.37)}$$

where B_c/B is the gradient of a plot of B_c against B in the appropriate field range. An example plot of B_c vs B is shown in Fig. 2.19.

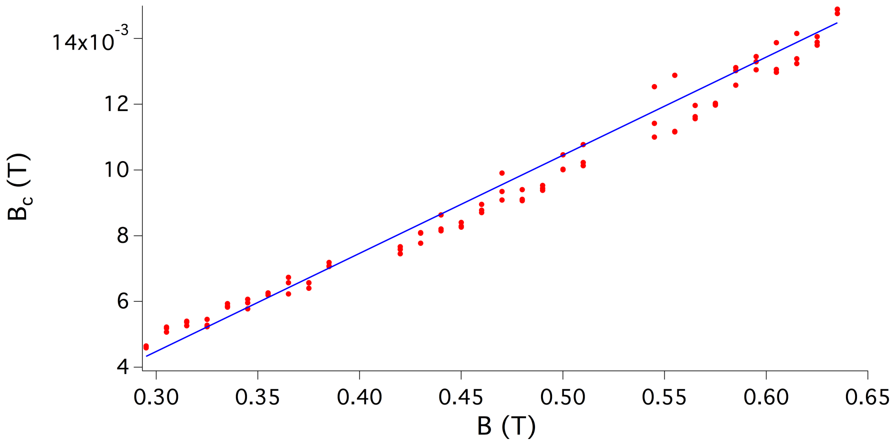

FIGURE 2.19. Correlation field B_c vs magnetic field B for determination of phase coherence length, following Ref. [29]. Analysis was performed on the AlGaAs/GaAs electron billiard device Ca and returned a fit line (blue) with a gradient of $B_c/B = 0.02985$, corresponding to a phase coherence length of 3.5 μm.

2.9. Low-Temperature Measurement

All low-temperature experiments described in this dissertation conducted at the University of Oregon were performed using an Oxford Instruments Low Loss Dewar (LLD) with a ^{3}He Heliox-VL Insert, which allows for cooling electronic devices to a base temperature of 240 mK and holding these temperatures for many days at a time. Electrical contact is made between the electron billiard device and a semiconductor chip using wire bonding; the chip is then mounted on a connection header on the insert, and may subsequently be referred to as the ‘sample’. The cryostat, shown schematically in Fig. 2.20, consists of a 90 L main bath for liquid ^{4}He surrounded by a 65 L liquid nitrogen (LN$_2$) jacket and outer vacuum canister (OVC) at a pressure of roughly 10^{-6} mbar to minimize radiative heat transfer with the surroundings. The experimental sample is mounted to the bottom of a sample insert containing a fixed amount of ^{3}He, which is gaseous above 3.2 K. Prior to insertion into the liquid helium main bath, the lower portion of the sample insert is enclosed in an inner vacuum canister (IVC), which is pumped down to a pressure of roughly 10^{-3} mbar before introducing a few mL[2] of ^{4}He exchange gas.

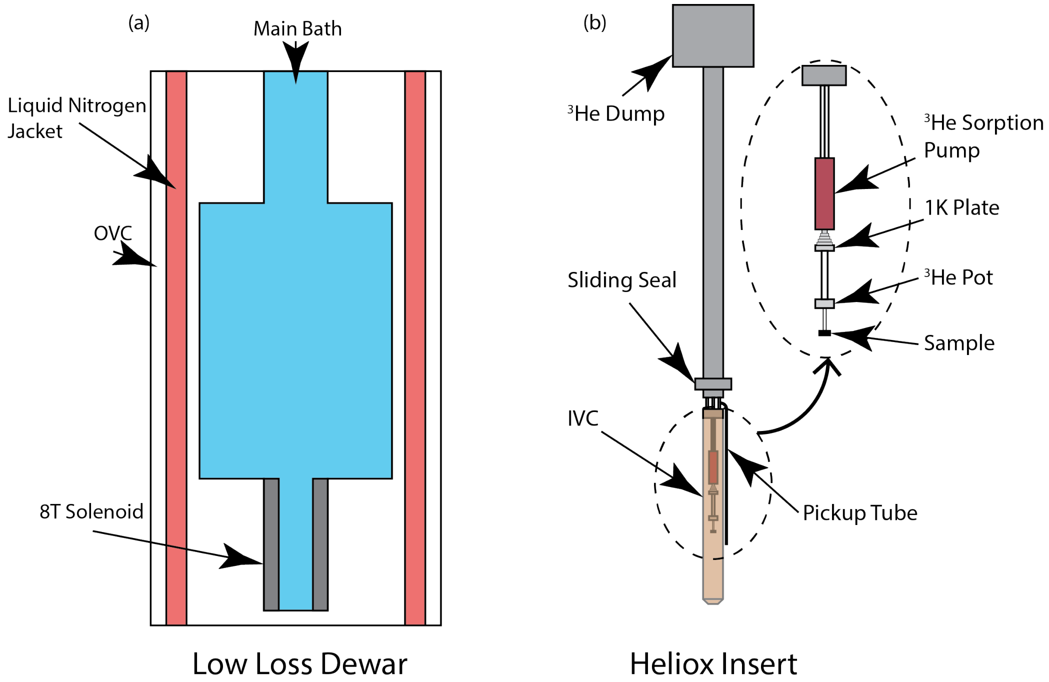
(a)
Main Bath
Liquid Nitrogen Jacket
OVC
8T Solenoid
Low Loss Dewar
(b)
³He Dump
³He Sorption Pump
1K Plate
³He Pot
Sample
Sliding Seal
IVC
Pickup Tube
Heliox Insert

FIGURE 2.20. Schematic of the Oxford Instruments LLD and ^{3}He Heliox-VL Insert. (a) A liquid nitrogen jacket (red) surrounds a liquid helium bath (blue) which houses a superconducting solenoid (gray). (b) Insert onto which the electrical device is mounted and which is lowered into the liquid helium bath. The inner vacuum chamber (IVC; tan) encloses the sample and the apparatus which allows sub-Kelvin temperatures to be reached.

Sub-Kelvin temperatures are achieved in the ^{3}He cryostat as follows: The liquid ^{4}He bath cools the IVC to 4.2 K, which is in turn brought into thermal equilibrium with the experimental sample via the exchange gas inside the IVC. A roughing pump attached to the top of the sample insert draws liquid ^{4}He into a pickup tube located near the bottom of the sample insert and through a coil in thermal contact with a metal plate. The helium in the tube undergoes evaporative cooling, bringing the temperature of the plate (known as the 1 K plate) to roughly 1.5 K. An activatedcarbon sorption pump removes the exchange gas from the IVC, while a ^{3}He sorption pump is heated to introduce gaseous ^{3}He to the interior of the insert. The ^{3}He then condenses at the 1 K plate and collects in a ^{3}He pot in thermal contact with the sample, bringing the sample temperature down to approximately 1.5 K. Finally, the ^{3}He sorption pump heater is switched off such that the pump evaporatively cools the liquid ^{3}He in the ^{3}He pot, bringing the pot and sample down to a temperature of roughly 240 mK.

---

[2] Colloquially, a sparrow's fart.

Electrical measurements of the electron billiard devices are performed using either a constant-current or a constant-voltage configuration. In the constant-current configuration, a Stanford Research Systems SR830 lock-in amplifier supplies a 0.1 V (peak-to-peak voltage) electrical signal at 37 Hz or 73 Hz, which is then passed through a 100 MΩ ballast resistor in series with a 10 kΩ resistor and the sample to yield a current of 1 nA. The lock-in amplifier frequencies are chosen so as to avoid any harmonics with the 60 Hz frequency of the electrical mains to mitigate unwanted noise. The role of the ballast resistor is to provide a known, constant resistance several orders of magnitude higher than any other resistance in the signal path such that the current through the circuit remains very nearly constant. It is necessary to restrict the applied current to the order of nanoamps so as to ensure that $eV \ll k_BT$ to avoid electron heating effects. The 10 kΩ resistor provides a known resistance across which we measure a voltage drop to extract a precise value for the current passed through the sample. Measuring the voltage drop across the sample, in conjunction with the measured current, then provides a measurement of the conductance through the sample. Voltage measurements are performed using SR830 lock-in amplifiers phase-locked to the source amplifier, such that voltage signals on the order of microvolts can be distinguished.

In the constant-voltage measurement configuration, the source SR830 lock-in amplifier provides a 1 V signal which is passed through a voltage divider to drop the voltage to 100 µV, which is then applied across the device. An additional SR830 lock-in amplifier phase-locked with the source then measures the current through the device, which is on the order of hundreds of nA. The actual voltage drop across the device is also measured with a lock-in amplifier, such that the conductance through the billiard is calculated from measured values of both voltage and current.

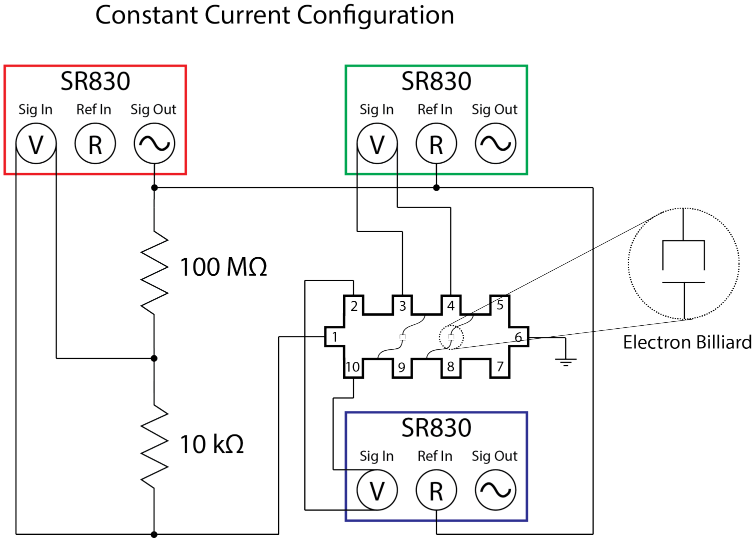
Constant Current Configuration
SR830
Sig In
Ref In
Sig Out
V
R
SR830
Sig In
Ref In
Sig Out
V
R
100 MΩ
10 kΩ
1
2
3
4
5
6
7
8
9
10
Electron Billiard
SR830
Sig In
Ref In
Sig Out
V
R

FIGURE 2.21. Schematic of the constant-current electrical measurement setup. A current of 1 nA enters the device at lead 1 and exits to ground at lead 6. In this example, the red SR830 lock-in amplifier provides the driving current and also measures the voltage drop across the 10 kΩ resistor to measure the current supplied to the device, while the green SR830 lock-in amplifier measures the longitudinal voltage drop across the left billiard, and the blue SR830 lock-in amplifier measures the transverse voltage drop V_{yy}.

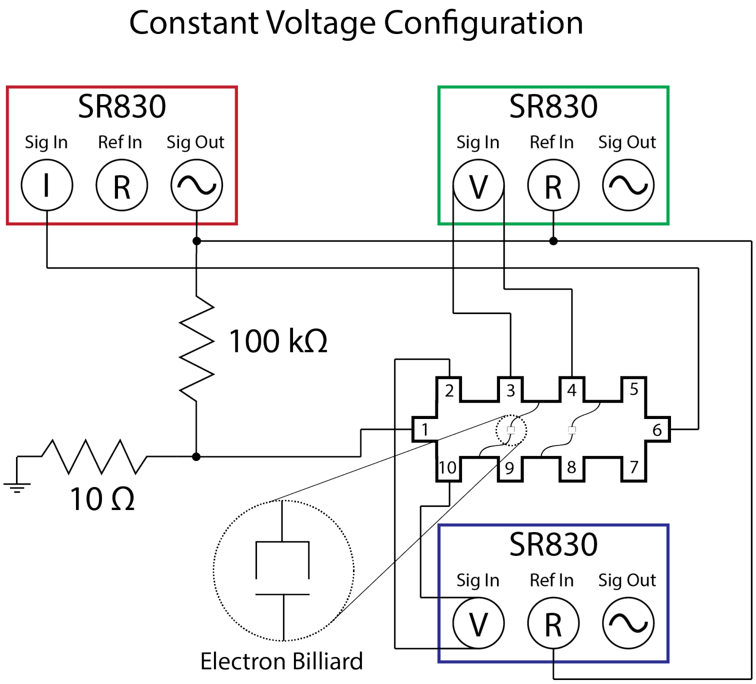
Constant Voltage Configuration
SR830
Sig In
Ref In
Sig Out
I
R
SR830
Sig In
Ref In
Sig Out
V
R
100 kΩ
10 Ω
2
3
4
5
1
6
10
9
8
7
SR830
Sig In
Ref In
Sig Out
V
R
Electron Billiard

FIGURE 2.22. Schematic of the constant-voltage electrical measurement setup. A voltage of 100 µV is applied to the device at lead 1 and exits to ground via an ammeter through lead 6. In this example, the red SR830 lock-in amplifier provides the driving voltage and also measures the current passed through the device, while the green SR830 lock-in amplifier measures the longitudinal voltage drop across the left billiard, and the blue SR830 lock-in amplifier measures the transverse voltage drop V_{yy}.

CHAPTER III

FRACTALS

As a means to probe the phase space of electrons in electron billiard devices, we employ a fractal analysis of MCF traces measured on these billiards. Before discussing the analysis methods which may be applied to the variety of fractals we seek to observe, let us begin with a general description of fractal patterns, their analysis, and the difficulties presented by such analyses.

3.1. On Self-Similarity and Dimension

As we shall see, there are several different kinds of structures which we may call 'fractals'. Although the precise nature of the fractals differs from case to case, we may generally define a fractal structure as one which preserves some measurable quantity across many of its scales. For instance, a mathematically-generated spatial fractal such as the Sierpinski Carpet (Fig. 3.1) is an example of a structure whose patterns repeat exactly at all length scales that are an integer factor of 1/3 the scale of the entire structure.

However, this exact repetition of features is not a necessary quality of fractals—spatial fractals can also exist as statistically self-similar fractals, in which the preserved measurable quantity is a statistical property such as coverage density. All spatial fractals, whether statistical or exact in nature, may exist as structures embedded in one, two, or three spatial dimensions—for instance, the Cantor Set (Fig. 3.2) is an exactly self-similar fractal structure embedded in one spatial dimension (though necessarily visualized in two), whereas the branching structures of lung

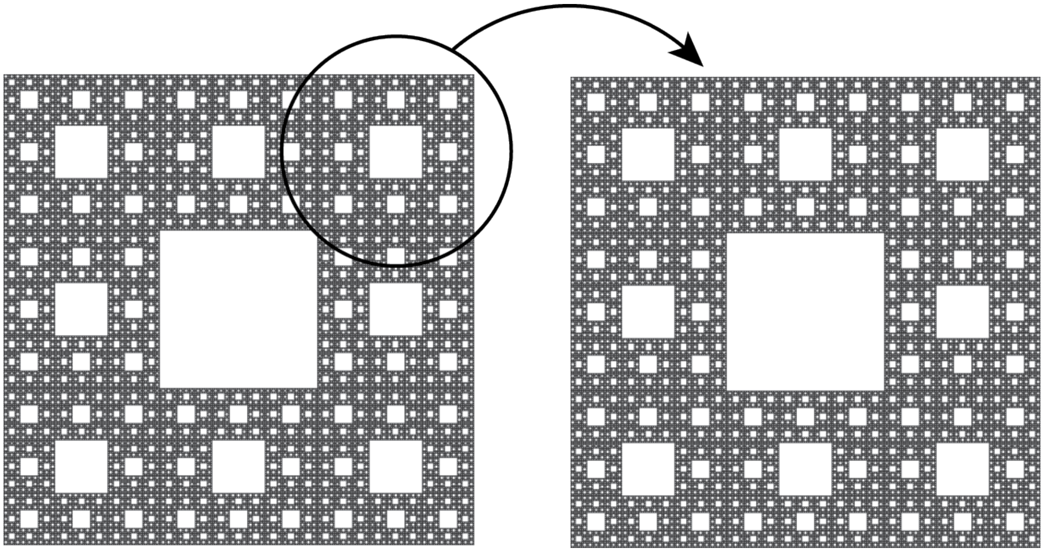

FIGURE 3.1. The Sierpinski Carpet exhibits spatial exact self-similarity. Image released into public domain by Wikipedia user Joshi1983.

bronchioles and tree branches are examples are statistically self-similar spatial fractals embedded in three dimensions.

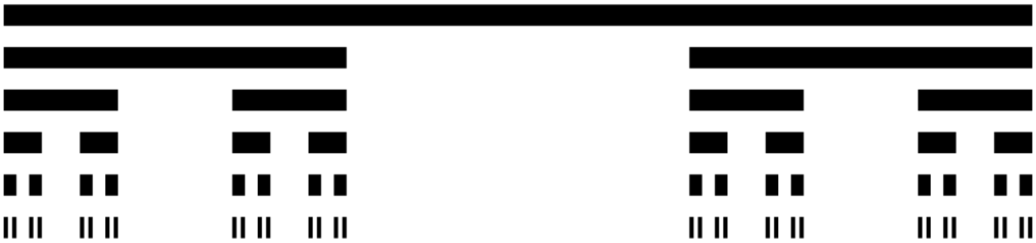

FIGURE 3.2. The initial six iterations of the construction of the Cantor set. The Cantor set is an example of an exact self-similar fractal structure embedded in one dimension. The set is constructed as follows: Beginning with the interval $[0, 1]$, remove the middle third of the set to produce the set $\left[0, \frac{1}{3}\right] \cup \left[\frac{2}{3}, 1\right]$. Repeating this process on the remaining segments yields increasingly fine, nonempty sets; the limit of these sets is the Cantor set. Image released into public domain by Wikipedia user Sarang.

When speaking of the dimensionality of fractal structures, we have thus far only discussed the dimensionality of the structure comprising the object. In most contexts familiar to everyday life, it suffices to equate this ‘topological dimension’ with the dimension of the object in question—we are familiar with a wide range of two-dimensional geometric shapes on the plane and three-dimensional solids in space, and in these cases restricting possibilities for spatial dimensions to the integers zero, one, two, and three is quite reasonable. In the case of fractal structures, however, this familiar conception of dimensionality breaks down: By employing generalized geometrical analysis techniques that return the expected integer dimension values for standard, 'Euclidian' shapes, we find that fractal structures are generally characterized by non-integer dimensions. To understand why this is so, it is instructive to reflect on what is meant when we speak of an object's 'dimension'.

It is perhaps tempting to define the dimension of a structure as the number of unique coordinates needed to specify any point on the structure. For instance, a point on a plane may be specified by its x and y coordinates, while a point on a solid is identified using three distinct coordinates. Such a definition is mathematically imprecise, however—since the cardinality of the set $\Re^n$ is the same for all $n \in \mathbb{Z}$, it is possible to define a one-to-one mapping between the points in any two sets $\Re^{n_1}$ and $\Re^{n_2}$ ($n_1,\ n_2 \in \mathbb{Z}$), and thus, any point in $\Re^n$ can in principle be uniquely identified with a single number.

A more precise and general definition of dimension may be obtained by considering the properties of a space-filling curve. In general, we may consider a curve to be any continuous function whose domain is the unit interval $[0, 1]$. It is possible, then, to construct a curve by iteration such that the limiting curve visits every point in some area of the plane, hence "filling" the space. Such a curve thus provides an example of a function that maps an interval in $\Re^1$ (the domain of the function) to an area in $\Re^2$—that is, using a one-dimensional line to fill a two-dimensional space. Figure 3.3 displays the first-studied space-filling curve, known as the Peano curve.

The limiting state of this iterative construction process is a structure comprised only of piecewise linear curves and yet it passes through every point in the unit square.

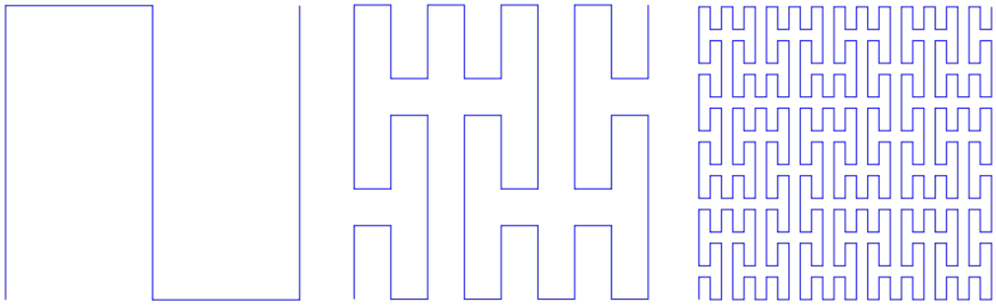

FIGURE 3.3. The first three iterations in the generation of the Peano curve. The Peano curve is constructed as follows: Beginning with the initial figure in the unit square (left panel), a new iteration is formed by dividing the unit square into nine subdivisions, each of which is replaced by the figure of the prior iteration, scaled and flipped such that the resulting figure remains a single continuous line. The Peano curve, as the limit of this iterative process, is a figure which is comprised of a single line but visits every point in the unit square. Image licensed under Creative Commons CC BY-SA 3.0 (creativecommons.org/licenses/by-sa/3.0/us) by Wikipedia contributor To Campos1.

In the case of a space-filling curve, we find that a one-dimensional object can apparently fill a two-dimensional area. To understand the nature of this space filling, it is thus necessary to assign titles to these evidently distinct conceptions of dimension. Since the curve is exploring the area of a two-dimensional plane, we say that the curve has an 'embedding dimension' of two; since the elements of the curve itself are one-dimensional, we say that the curve has a 'topological dimension' of one. That is, the embedding dimension, D_{E}, describes the space in which an object exists, while the topological dimension, D_{T}, describes the basic elements constituting the structure.

3.2. Motivating the Fractal Dimension

For familiar, Euclidian forms, it is generally the case that $D_{\mathrm{T}} = D_{\mathrm{E}} \in \mathbb{Z}$. However, the case of the space-filling curve demonstrates that an object may occupy a higher-dimensional space than its constituent elements. In fact, the dimensionality of a structure need not be limited to its topological or embedding dimensions—it is possible to create a structure that is, for instance, more space-filling than a one-dimensional line but does not entirely fill a two-dimensional area. To quantitatively evaluate the degree to which a general curve fills space, we introduce the concept of a fractal dimension.

The concept of a fractional, or fractal, dimension is often traced back to an early work by the mathematician Benoit B. Manedelbrot, who, in 1967, provided mathematical rigor to the question: "How long is the coast of Britain?" [31]. In fact, the question had been discussed by Lewis Fry Richardson six years prior in the *General Systems Yearbook* [32]. Richardson, a pacifist and mathematician (among other titles), sought evidence for the hypothesis that the probability of two neighboring nations engaging in war is related to the length of their shared border. The difficulty in evaluating this statement, Richardson and Mandelbrot note, is evident in the fact that various reports of the length of the west coast of Britain yield values spread over a remarkable range, differing by up to a factor of three. Indeed, more precise measurements of the coastline length—that is, measurements done with a smaller "ruler" relative to the size of the map—invariably produce greater values for the total length (see Fig. 3.4). This quality reflects the fact that this profile is an example of a 'self-similar' structure—that is, a structure which, upon magnification, appears to possess the same statistical qualities (if not exact details) at a wide range of length scales.

Mandelbrot notes that Richardson had indeed supplied an empirical relation between a measured coast length L and the smallest unit of measurement G:

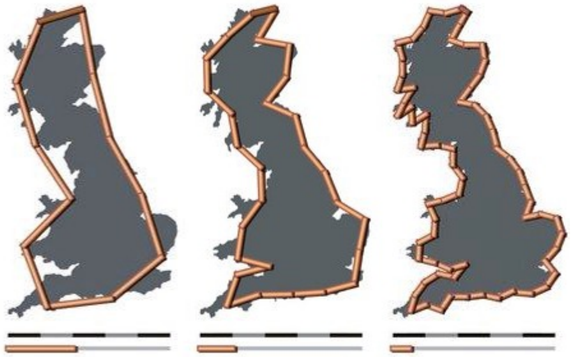

FIGURE 3.4. Evaluating the length of the coastline of Britain at different levels of precision. When the length of the "ruler" used to measure the profile is reduced, the number of rulers needed to encompass the profile increases at a greater rate, yielding a greater number for the measured total length. Image licensed under Creative Commons CC BY-SA 3.0 (creativecommons.org/licenses/by-sa/3.0/us) by Wikipedia contributor Avsa.

$L(G) = MG^{1-D}$, where M is a positive constant and $D \geq 1$—but points out that "unfortunately it attracted no attention" [31].

In light of this apparent fundamental indeterminacy, Mandelbrot notes that familiar geometrical metrics such as length are inadequate to describe the complexity found in nature. To this end, Mandelbrot expands upon Richardson's empirical parameter to introduce the concept of a fractional, or fractal,[1] dimension to characterizes the rate at which the number of rulers needed to encompass the coastline "outpaces" the rate at which the individual rulers are shrunk when viewing the structure with increasing precision.

To generalize the concept of dimension, Mandelbrot notes, it is instructive to examine the scaling behavior of trivially self-similar objects such as a line, a square, and a cube. Consider a line segment of length L, which can be decomposed into N non-overlapping subsets of length L/N, each of which is identical to the whole

---

[1] Though Mandelbrot discusses the concept of fractional dimension in this 1967 paper, he did not introduce the term 'fractal' until 1975 [33].

segment save for a scaling factor $r(N) = 1/N$. Similarly, a square with side length L can be decomposed into N^2 facsimiles of side length L/N, which are each scaled down by a factor $r(N) = 1/\sqrt{N}$, and a cube of side length L can be decomposed into N^3 copies of side length L/N with corresponding scaling ratio $r(N) = 1/\sqrt[3]{N}$; see Fig. 3.5. This result can be generalized by noting that the scaling ratio $r(N)$ follows the relationship $r(N) = 1/N^{1/D}$, where $D = -\log(N)/\log(r(N))$ is called the similarity dimension of the figure in question.

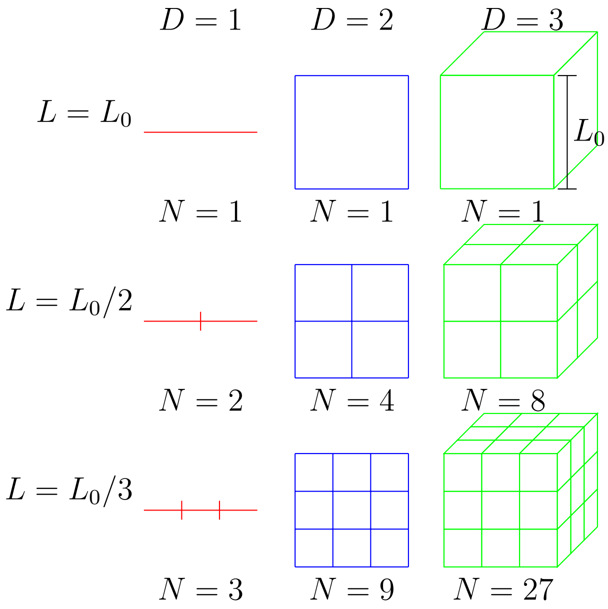

FIGURE 3.5. Defining the similarity dimensions of trivially self-similar Euclidian shapes. A Euclidian shape in D dimensions contains $N = (L/L_0)^{-D}$ exact copies of itself scaled by $\epsilon = L/L_0$. Image provided by Rick Montgomery.

This formulation of a 'similarity dimension' is easily extended to exact self-similar figures that can be built by iteration. For instance, consider the Koch curve, whose construction is displayed in Fig. 3.6. The Koch curve is constructed as follows: Beginning with a line segment of unity length, append onto the segment an equilateral triangle whose base corresponds to the middle third of the line segment; then remove this segment. The resulting figure consists of four line segments, each of which has been scaled down by a factor of 1/3. The concept of a similarity dimension does not yet apply to such a shape, since no nontrivial subset of the shape is identical to the whole; however, repeating the above process by iteration produces figures with increasingly fine detail, such that the limiting state of this series exhibits exact self-similarity. Since this final figure is decomposable into four exact copies of itself, each scaled down by a factor of 1/3, we can apply the above relation to find that the Koch curve has a similarity dimension of $D = -\log(4)/\log(1/3) \approx 1.26$. We may also use the example of the Koch curve to understand the evidently divergent perimeter of self-similar objects. Note that at every iteration in the construction of the Koch curve, the total length of the curve increases by a factor of 4/3. Thus, the Koch curve, as the limiting case of this process, has infinite perimeter!

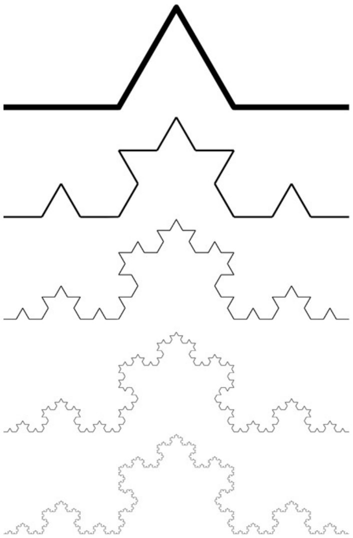

FIGURE 3.6. The Koch Curve is an example of an exact self-similar figure with a non-integer similarity dimension. From fractalfoundation.org/resources/fractivities/koch-curve/

The similarity dimension described above is only one of many dimensions that can be defined and calculated for a given figure. Indeed, its scope of usefulness is rather limited, as it can only treat figures that exhibit exact self-similarity, whereas the complexity seen in natural systems such as coastlines exhibit self-similarity only in the statistical sense. To approach this more general class of fractal systems, we introduce the (roughly self-explanatory) ‘box-counting dimension’, also known as the ‘covering dimension’. For a structure embedded in two dimensions[2], the box-counting dimension is calculated as follows: First, overlay a square grid with total size $L \times L$ and boxes of size $\ell \times \ell$ over the figure in question, and count the number of boxes $N(\ell)$ in which some portion of the figure in question is found (see Fig. 3.7). Repeat this procedure for a variety of box sizes ℓ and construct a plot of $\log(N(\ell))$ vs $\log(1/\ell)$; the gradient of the best-fit line to these data then corresponds to the box-counting dimension D.

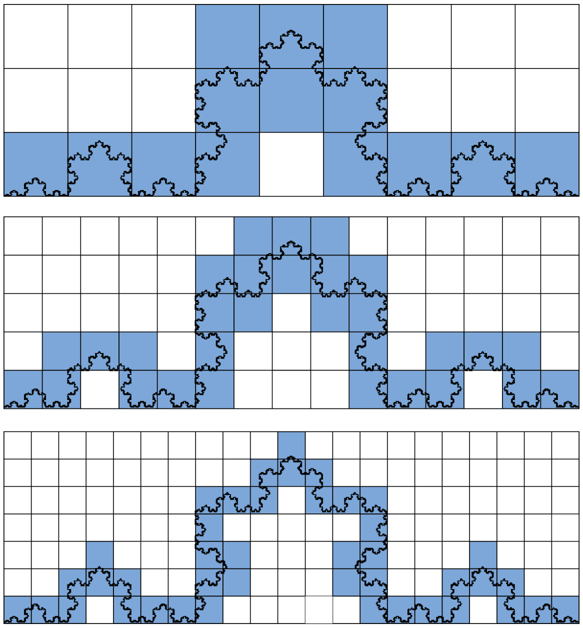

FIGURE 3.7. Applying the box-counting method to the Koch Curve. Koch Curve image released into public domain by Wikipedia user Quackor.

---

[2] While the box-counting method is most often applied to structures embedded in two dimensions, it is straightforward to generalize the technique to higher- or lower-dimensional systems.

Another means of conceptualizing the box-counting method is to observe that the set of all counted boxes at a given length scale ℓ serves to constitute an approximation of the total structure as observed at the length scale ℓ. In general, however, the boxes covering the analyzed structure will not correspond well to the shape of the structure at any length scale—see, for instance, Fig. 3.7, in which it is evident that the incommensurability of the square boxes and the Koch curve leads to a markedly rough representation of the structure at all length scales. By contrast, there exists a subset of fractal structures for which a box-counting method returns exactly the similarity dimension of the structure. For instance, consider the Sierpinski carpet (Fig. 3.1): the rectilinear exact self-similar nature of this structure leads to a correspondence between the structure and its covering boxes for all length scales $\ell = L/3^n$, $n = 1, 2, 3, \ldots$. Such a circumstance is referred to as a 'commensurability' between the structure and its covering boxes, such that a box-counting analysis that operates only at these specific length scales provides an exact measurement of the similarity dimension of the structure.

The box-counting method for the estimation of fractal dimension is appealing in its simplicity, but several considerations must be made to optimize its utility. First, it is necessary to choose an appropriate range of box sizes ℓ over which to examine the scaling trend. It is clear that a fractal scaling trend cannot extend over all length scales—if it is possible to encompass a structure of interest in a box of size $L \times L$, applying the box-counting method with boxes of size $\ell \geq L$ will always return a value $N(\ell) = 1$, such that the apparent fractal dimension is zero in this regime. Also, in a length scale range where $\ell \approx L$, it will be the case that nearly all boxes are filled, such that the box count $N(\ell)$ will scale as the square of the inverse box size $1/\ell$, returning an apparent fractal dimension of $D = 2$. In this case, we may say that the pattern "looks two-dimensional" when examined at the coarse scale. The opposite extreme of possible length scales merits consideration as well. For a mathematically-generated fractal figure, taken as the limiting case of an iterative generating procedure, the figure may extend to arbitrarily fine scales such that the scaling trend revealed by the box-counting method can be witnessed at arbitrarily small box sizes ℓ. The fractal structures that appear in nature, however, necessarily exhibit a smallest length scale at which a scaling trend may be supported: certainly, the trend must break down as the scope of examination reaches the molecular and atomic scales, but the fractal structure typically "bottoms out" at length scales many times larger than this. In practice, when the box-counting method is applied at length scales ℓ that are smaller than the minimum feature size observed in the structure, the number of filled boxes $N(\ell)$ scales linearly with the inverse box size $1/\ell$, and the figure "looks one-dimensional" to the analysis at these scales.

How, then, do we account for this limited range of length scales when assessing the fractal dimension using a box-counting method? This determination may be made either empirically, by observing the range of length scales over which the scaling plot is sufficiently linear, or by convention, based on statistical arguments. In practice, it is generally not known *a priori* whether a structure under consideration should be expected to be a fractal, and hence whether it should exhibit a linear scaling relation on a logarithmic plot between cutoffs defined by physical and measurement limitations. Therefore, it is common to adopt the following convention: The coarse-scale measurement limit of the range of length scales is tied to the physical coarse-scale limit and is set at $\ell = L/5$, where L is the side length of the smallest square that can entirely enclose the structure, to ensure that the grid consists of no fewer than 25 boxes. Hence, the coarse-scale analysis cutoff corresponds to this measurement limit. On the fine scale, the physical limit corresponds to the minimum physical feature size observed in the structure, while the measurement limit corresponds to the requirement that each box contain no fewer than five data points; in practice, the more restrictive of these two limits is chosen (i.e., the limit corresponding to the larger length scale).

Another consideration in the optimal execution of the box-counting method regards the precise position and orientation of the grid. Inasmuch as the box-counting method seeks to probe an inherent quality of a structure, the observed fractal dimension should not be affected by a spatial translation of the grid with respect to the structure. However, consider the case shown in Fig. 3.8, in which the box-counting method is applied to a profile. In the "traditional" box-counting scheme, all boxes that contain any portion of the figure under examination are counted toward the total, and we find that 35 boxes are filled using this box size ℓ. Suppose, however, that one is able to reposition the boxes semi-independently of one another, by translating contiguous $\ell \times \ell$ boxes within columns of width ℓ—in this case, we find that, through a careful repositioning of the boxes, the box count $N(\ell)$ has dropped to 29. This discrepancy serves to motivate an amendment to the box-counting method described above known as the variational box-counting method, in which the boxes are shifted in columns as described above so as to minimize the number of boxes needed to entirely cover the figure in question. The variational box-counting method thus provides a means of breaking the ambiguity seen in the traditional box-counting method. Note that some ambiguity remains in this amended method, in the sense that the rotational orientation of the columns with respect to the figure remains unspecified. To address this ambiguity, one may repeat the above-described variational method at a variety of rotation angles of the grid with respect to the figure and choose the case that minimizes $N(\ell)$ for each value of ℓ, but in practice, this residual variation is typically negligible for practical purposes.

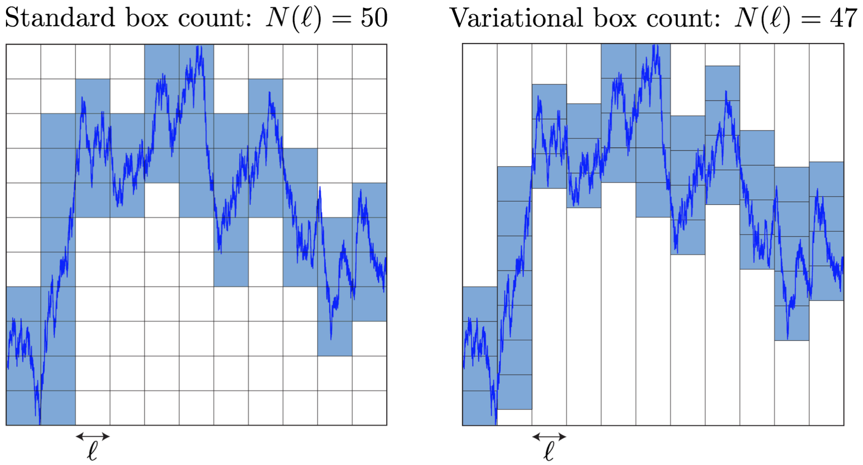
Standard box count: $N(\ell) = 50$

Variational box count: $N(\ell) = 47$

FIGURE 3.8. Visualizing the effect of shifting box locations. In this example, when the boxes are fixed to a grid, we find a box count $N(\ell) = 50$; however, when the $\ell \times \ell$ boxes are allowed to shift vertically in columns of width ℓ, the box count $N(\ell)$ drops to 47.

3.3. Time-Series Fractal Structures

The above discussion of fractal structures considers spatial fractal figures—that is, figures whose fractal characteristics are manifest in their spatial form. Another important class of structures to which fractal analysis may be directed is that of 'time-series' structures—that is, structures that take the form of a single-valued function of a single variable. As suggested by their name, time-series structures may be graphs of some quantity—say, stock market prices, or atmospheric pressure—that fluctuates in time, but for the purposes of this document we take the term to refer to any plot of a dependent variable as a single-valued function of an independent variable.

As with spatial structures, time-series structures may exhibit fractal characteristics, either in the statistical or exact sense. Furthermore, as with spatial fractals, time-series structures may be quantitatively described using a fractal dimension; however, the box-counting method described above for determining this dimension is no longer suitable. Simply put, the reason for this is the fact that the box-counting method assesses the fractal dimension of a shape in space, and the "shape" of a time-series structure is ill-defined. That is, since the two axes of a plot of a time-series structure generally represent fundamentally incommensurate variables, the aspect ratio of a plot to be analyzed is effectively arbitrary. For instance, consider the fractal structure displayed in Fig. 3.9, which plots the daily closing price of a certain technology stock over a period of roughly 16 years. This figure displays three versions of the same data, with their respective y-axes scaled by different factors. Qualitatively, it may be said that the data in the top panel appear the most linear, with the trend becoming more space-filling as the dependent variable range is reduced. Thus, since a box-counting fractal analysis technique effectively assesses the extent to which a figure fills a plane, such an analysis would yield distinct results for each of these plots.

The difficulty here lies in the fact that a box-counting fractal analysis necessarily treats a figure as a spatial entity whose orthogonal components are commensurate. A time-series trace such as the one displayed in Fig. 3.9 lacks this property, for the aforementioned reasons, but may still exhibit fractal characteristics in the form of either statistical or exact self-affinity. Exact and statistical self-affinity refer to structures whose precise details or statistical properties, respectively, are repeated as its two orthogonal dimensions are resized by independent quantities, in contrast with exact and statistical self-similarity, in which the rescaling must be isotropic [34]—due to the incommensurability of the orthogonal axes defining a time-series trace, such structures cannot exhibit self-similarity, only self-affinity. As an example, see Fig.

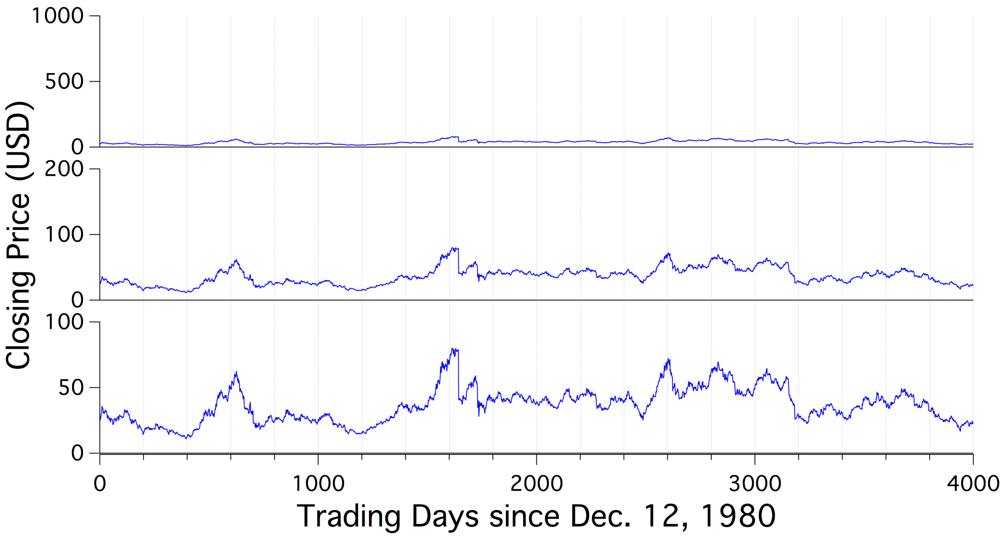

FIGURE 3.9. Daily closing prices for a single stock from December 1980 to October 1996. Each of the three plots displays the same data, but with their respective y-axes scaled by different amounts. Therefore, a box-counting fractal analysis would return unique results for each plot.

3.10, in which these same data are displayed alongside a subset of the data. When this subset is appropriately rescaled in the y-axis, the resulting plot shares the general statistical properties of the original trace, and hence exhibits statistical self-affinity.

It is also possible, albeit less common, for a time-series trace to exhibit *exact* self-affinity. Take for example the magnetoconductance fluctuation traces shown in Fig. 3.11, in which rescaling the x- and y-axes of the traces about the zero-field resistance peak by carefully chosen factors reveals structures which share the characteristics of the original trace [8].

3.4. Fractal Analysis of Time-Series Traces: Beyond Box-Counting

Because the fractal character of a time-series trace as analyzed by a box-counting method depends on the aspect ratio chosen to plot the data, which is in turn an arbitrary choice, it is necessary to utilize fractal analysis techniques that are

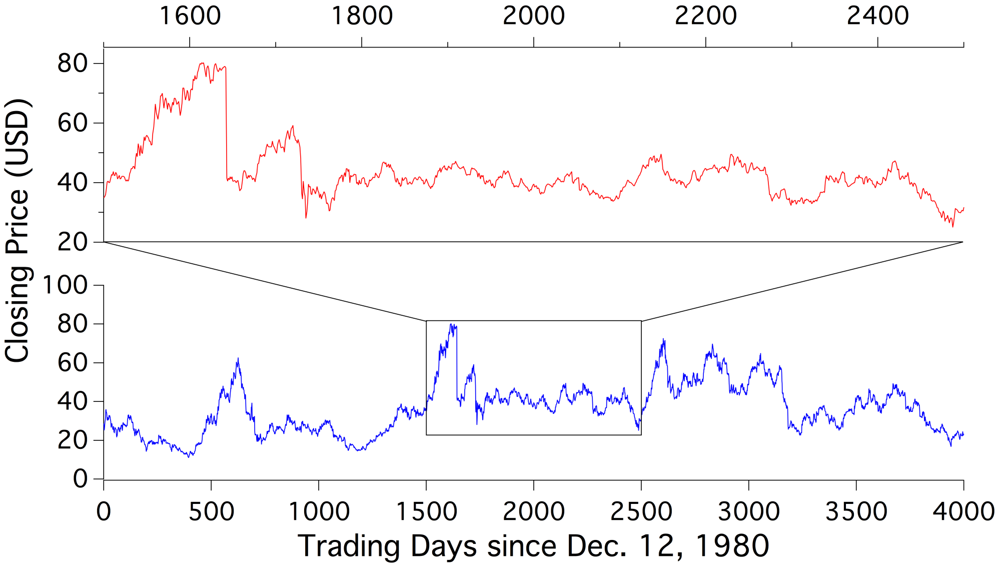

FIGURE 3.10. Statistical self-affinity in a fractal time-series trace. Choosing a subset of the stock price data shown in Fig. 3.9 and rescaling the y-axis yields a trace that shares statistical properties with the original.

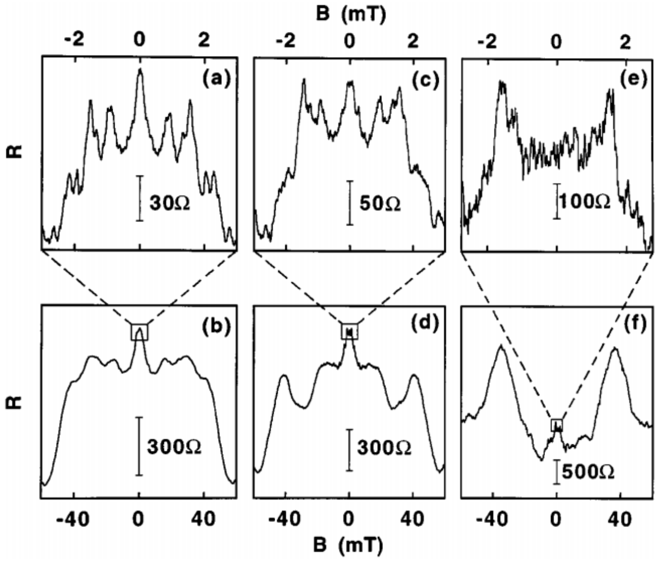

FIGURE 3.11. Magnetoresistance fluctuations recorded in an electron billiard device can provide examples of exact self-affinity in time-series structures. From Ref. [8].

insensitive to this geometric parameter. Below is a discussion of a sampling of the techniques proposed in the literature.

Early fractal analyses of MCF traces were performed using the variational box-counting method described above [22, 35], which does indeed offer performance improvements over the traditional fixed-grid box-counting method, but still suffers from a fatal flaw. To see why this is the case, consider the trace shown in Fig. 3.12, in which the variational box-counting method is assessing the stock data mentioned above at some length scale ℓ.

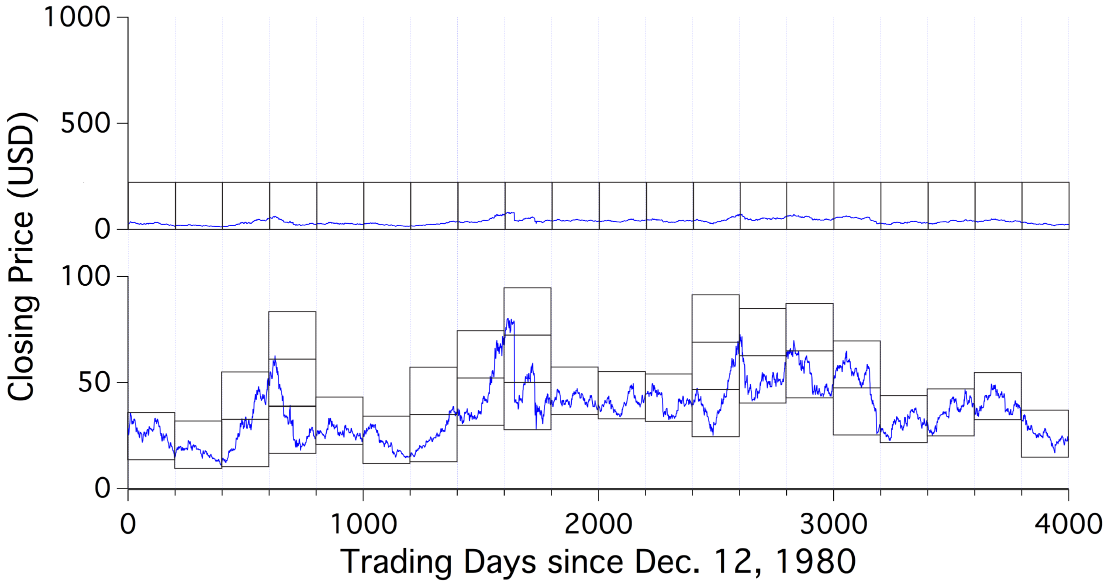

FIGURE 3.12. Visualizing a variational box-counting method applied to the stock price data shown above at a "length" scale $\ell = 200$ trading days. When the data are displayed with a price range from 0-100 USD, the box count at this value of ℓ is 37; when the price range is expanded to 0-1000 USD, the box count shrinks to 20.

In Fig. 3.12, we see the stock price data displayed at two different scalings of the price axis, and a variational box-count method is applied at a "length" scale $\ell = 200$ trading days. When the prices shown range from 0-100 USD, we find that it takes a minimum of 37 boxes to entirely cover the trace. However, when the price range is expanded to 0-1000 USD (effectively increasing the domain:range aspect ratio of the data), we find that we only need 20 boxes to cover the trace. Indeed, it should be apparent that the number of boxes $N(\ell)$ needed to cover the compressed data trace will be proportional to $1/\ell$ for all values of ℓ that yield boxes taller than the data range in any of its L/ℓ columns—that is, as long as the boxes are "taller" than the data within each column, the trace will look 1-dimensional to this method.

The problem here, of course, is that the concept of an $\ell \times \ell$ "box" on a time-series trace is meaningless, since the enclosed "area" has units of (in this case) days times dollars. Whereas it was entirely reasonable in the case of a box-counting analysis of a spatial fractal to tile the figure with boxes of a well-defined area, the concept of a square drawn on a plot with incompatible and independently-scaleable axes is nonsensical. One possible resolution to this difficulty is to adopt a convention in which all time-series traces under consideration are rescaled in their x- and y-axes such that the plot domain and range each run from 0 to 1, and the figure sent through a box-counting analysis is a square plot that just encloses the trace—while such a standardization procedure may provide a means for comparing the scaling properties of a set of similar time-series traces, the dimensions returned would remain meaningless in an absolute sense.

To develop a fractal analysis technique that effectively treats the character of time-series traces, one may effectively take one of two approaches: to treat a time-series trace as a geometric figure without a defined aspect ratio, or as a record of a process whose degree of randomness can be quantified. The latter approach was that taken by Harold Edwin Hurst who, in a 1951 paper on the long-term storage capacity of water reservoirs [36], laid the foundation for a quantitative understanding of complex time-series structures. The impact of Hurst's paper is survived by the 'Hurst exponent' H, which characterizes the nature of the randomness present in a time-series trace by means of an autocorrelation measurement. Specifically, a Hurst exponent of $H = 0.5$ corresponds to a process that is perfectly random—that is, the value of the trace at time t_i is entirely uncorrelated with the value at time t_j, $i \neq j$—while Hurst exponents in the range $0.5 < H < 1$ represent traces exhibiting positive autocorrelations, and Hurst exponents in the range $0 < H < 0.5$ represent traces exhibiting negative autocorrelations. Simply put, a positive autocorrelation can be understood to mean that a 'high' value (say, relative to the mean) is more likely to be followed by further "high" values, while a negative autocorrelation refers to a process which is more prone to rapid switching between "high" and "low" values at short time scales; see Fig. 3.13.

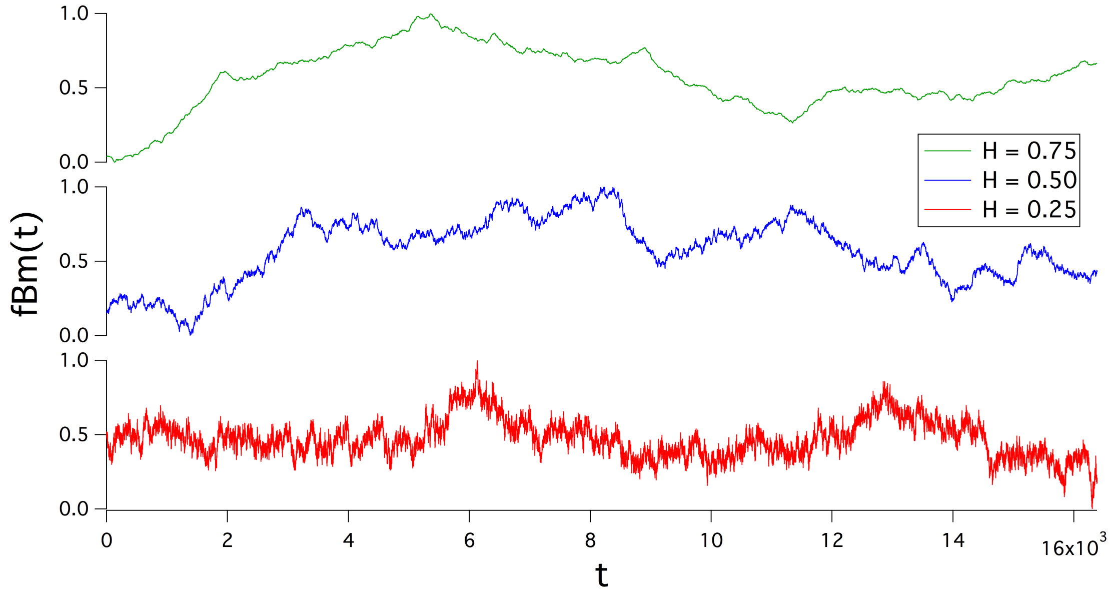

FIGURE 3.13. Time-series traces with Hurst exponents of $H = 0.25$, 0.50, and 0.75. A trace with $H = 0.5$ represents purely random process, whereas traces with $H = 0.25$ and $H = 0.75$ represent processes whose subsequent increments are negatively and positively correlated, respectively.

In practice, the Hurst exponent is calculated by means of examining the scaling properties of the 'rescaled range' of the data. Let the set of values $\{x_t\}$ $(t = 1, 2, 3, \ldots, T)$ represent the time-series trace under consideration, and let

$\{x_i, x_{i+1}, \ldots, x_{i+\tau}\}$, $\tau \leq T$, $i = 1, 2, 3, \ldots, T - \tau$ represent any sequence of $\tau + 1$ points within the data set. The rescaled range (R/S) statistic is then defined as:

$$\left(\frac{R}{S}\right)_\tau = \frac{1}{s_\tau}\left[\sup_{i \leq t \leq i+\tau} \sum_{k=i}^{t} (x_k - \overline{x}_{i,\tau}) - \inf_{i \leq t \leq i+\tau} \sum_{k=i}^{t} (x_k - \overline{x}_{i,\tau})\right], \qquad \text{(Equation 3.1)}$$

where $\overline{x}_{i,\tau} = (1/\tau)\sum_{t=i}^{\tau} x_t$ is the sample mean and $s_{i,\tau} = \left[(1/\tau)\sum_{t=i}^{\tau}(x_t - \overline{x}_{i,\tau})^2\right]^{1/2}$ is the sample standard deviation. The quantity $\left\langle \left(\frac{R}{S}\right)_\tau \right\rangle_i$ is then proportional to τ^H, such that the gradient of a plot of $\log\left(\left\langle \left(\frac{R}{S}\right)_\tau \right\rangle_i\right)$ vs $\log(\tau)$ corresponds to the Hurst exponent H.

A more direct means of evaluating the Hurst exponent characterizing a time-series traces is known as the 'variance method', which directly probes the scaling properties of the trace's autocorrelation as a function of time interval[3]. Specifically, the variance method calculates the quantity $V(\Delta t) = \left\langle [x_{t+\Delta t} - x_t]^2 \right\rangle_t$ for a range of values of Δt; since the Hurst exponent characterizes the long-range correlations of a time-series trace as $V(\Delta t) \propto (\Delta t)^{2H}$, a plot of $\log(V(\Delta t))$ vs $\log(\Delta t)$ should be linear (over an appropriate range) with slope $2H$. In practice, however, the variance method is an imprecise estimator of a trace's Hurst exponent, in part because it suffers from the diminished statistics of only examining the endpoints of each Δt 'window' rather than any of the points contained therein.

The next fractal analysis technique to be discussed is that proposed by Benoit Dubuc in a 1989 paper [37] on the fractal dimension of profiles. Dubuc's proposed 'variation method' shares many similarities with the variational box-counting method described above, but avoids the fundamental inconsistencies that arise when using a box-counting method that insists on counting an integer number of boxes. In short,

---

[3] In all discussions of time-series traces, I will refer to the independent variable as "time" if it is not otherwise specified.

Dubuc's variation method probes the space-filling properties of a time-series trace by assessing the scaling behavior of the amplitude of the trace in an ϵ neighborhood as ϵ is varied.

The practical implementation of Dubuc's algorithm is as follows: Consider a time-series trace $\{x_t\}$ ($t = 1, 2, 3, \ldots, T$). For a given value of ϵ, we define the functions $u_\epsilon(t)$ and $b_\epsilon(t)$ as follows:

$$u_\epsilon(t) = \sup_{t' \in R_\epsilon(t)} x_{t'}, \qquad \text{(Equation 3.2)}$$

$$b_\epsilon(t) = \inf_{t' \in R_\epsilon(t)} x_{t'}, \qquad \text{(Equation 3.3)}$$

where $R_\epsilon(t) = \{s : \ |t - s| \leq \epsilon \text{ and } s \in [1, T]\}$. That is, for a given value of ϵ and for each point t_i in the trace, examine the set of points $\{x_{t'}\}$ within ϵ data points of t_i, and let $u_\epsilon(t_i)$ and $b_\epsilon(t_i)$ be (respectively) the maximum and minimum values of $x_{t'}$ found in this range. Thus, $u_\epsilon(t)$ and $b_\epsilon(t)$ can be understood to represent (respectively) the upper and lower envelopes of oscillation of a trace at a particular scale set by ϵ. At large values of ϵ, $u_\epsilon(t)$ and $b_\epsilon(t)$ will be slowly varying relative to the variation present in the trace; reducing the value of ϵ will produce curves $u_\epsilon(t)$ and $b_\epsilon(t)$ that each resemble the trace under consideration with increasing fidelity (see Fig. 3.14).

Having constructed the curves $u_\epsilon(t)$ and $b_\epsilon(t)$, we then find $v_\epsilon(t) = u_\epsilon(t) - b_\epsilon(t)$ and calculate $V(\epsilon) = 1/\epsilon^2 \sum_t v_\epsilon(t)$. In this sense, $V(\epsilon)$ may be understood to be analogous to the (vitally, not necessarily integer) number of $\epsilon \times \epsilon$ "boxes" required to fill the "area" between $u_\epsilon(t)$ and $b_\epsilon(t)$—though, of course, the concept of "area" is ill-defined for a plot of a time-series trace. As with the box-counting method, the fractal dimension of the trace is then assessed by the relationship $V(\epsilon) \propto (1/\epsilon)^D$, such

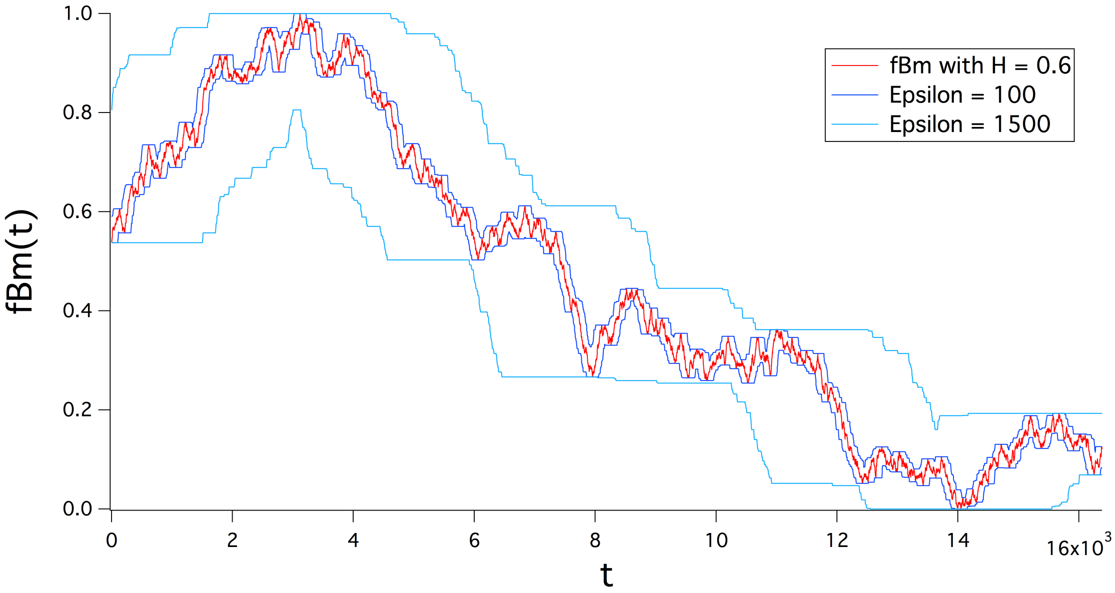

FIGURE 3.14. Visualizing the application of Dubuc's variance method at two distinct values of ϵ. The trace under consideration is a fractional Brownian motion (fBm), whose properties are discussed below.

that a plot of $\log(V(\epsilon))$ vs $\log(1/\epsilon)$ is expected to be linear with a slope corresponding to the fractal dimension D.

The final fractal analysis technique to be considered is known as 'adaptive fractal analysis' (AFA) [38], and shares many similarities with Dubuc's variation method. Whereas Dubuc's variation method can be understood as examining the generalized "area" needed to cover a time-series trace at different time scales, AFA probes the scaling of the fidelity of approximations to the trace itself at a range of time scales. As an illustration of the AFA algorithm, we again consider a time-series trace $x(t)$ ($t = 1, 2, 3, \ldots, T$). Next, we choose an odd integer window width $w = 2n+1$, $w < T$, and partition the data trace into subsets of length w which overlap by $n + 1$ data points. Within each window, we fit the data with a polynomial of order $M = 1$ or 2; the result is a series of disconnected lines (for $M = 1$) or parabolas (for $M = 2$) overlapping such that each value of t on the original trace corresponds to a point on each of two subset fit lines (except for the n data points at either end of the trace). In practice, using $M = 1$ is sufficient to obtain accurate estimates of H, as described below, so we shall limit our discussion to this case. Next, we "stitch" these fit lines together to create an approximation to the trace $x(t)$ as follows: Label the windows spanning the trace with consecutive integers, and their corresponding best-fit lines $y^{(j)}(l)$ $(l = 1, 2, \ldots, n + 1)$. Then, choosing a window j, construct the trace

$$y^{(w)}(l) = w_1 y^{(j)}(l + n) + w_2 y^{(j+1)}(l),\ l = 1, 2, \ldots, n + 1, \qquad \text{(Equation 3.4)}$$

where $w_1 = \left(1 - \frac{l-1}{n}\right)$ and $w_2 = \frac{l-1}{n}$. That is, each point $y^{(c)}(l)$ is the weighted average of the values of the two best-fit lines at that point, weighted such that the weights decrease linearly with the distance separating the point from the window's midpoint. Repeating this procedure across all windows yields a trace $y^{(w)}(t)$ which is continuous and differentiable, and which serves as an approximation to the trace $x(t)$ at a length scale defined by w (see Fig. 3.15).

As w is decreased, $y^{(w)}(t)$ will become a better approximation to $x(t)$; the scaling behavior of this fidelity as w is varied is used to determine the Hurst exponent. Specifically,

$$F(w) = \left[\frac{1}{T}\sum_{i=1}^{T}\left(y^{(w)}(t_i) - x(t_i)\right)^2\right]^{1/2} \propto w^H, \qquad \text{(Equation 3.5)}$$

such that a plot of $\log(F(w))$ vs $\log(w)$ will be linear with slope H.

3.5. Evaluating Fractal Analysis Techniques

Each of the above fractal analysis techniques is best understood as providing an estimate of the fractal dimension or Hurst exponent of a time-series trace.

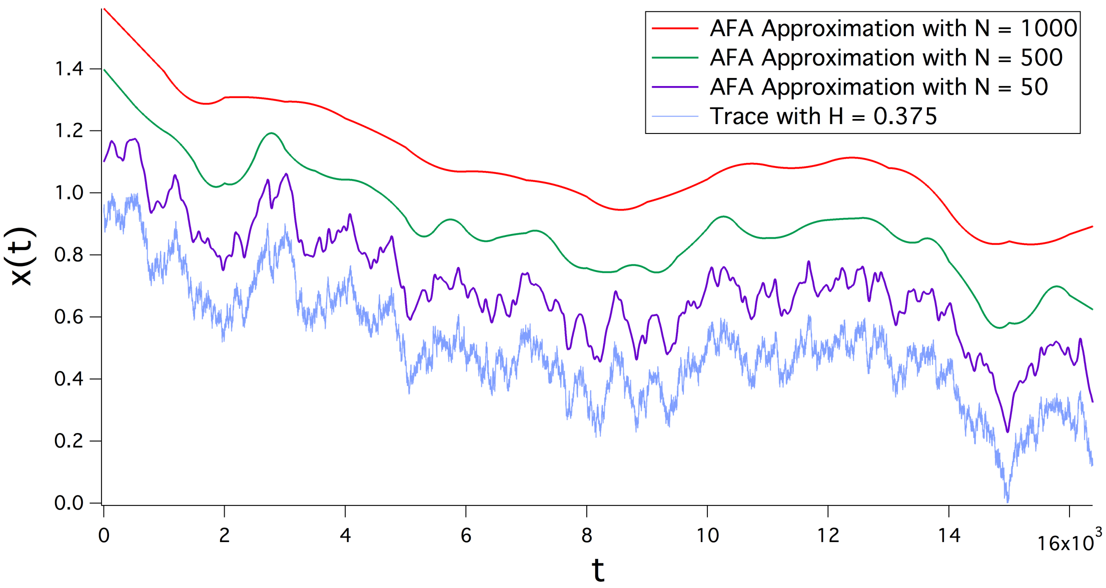

FIGURE 3.15. Visualizing the adaptive fractal analysis method. The light blue trace is a 16384-point fractal trace with $H = 0.375$, while the red, green, and purple traces represent approximations produced by the AFA technique at $N = 1000$, 500, and 50, respectively. Traces are vertically offset for clarity. Note that lower values of N create approximations that better represent the trace under consideration.

The sections that follow present a method for evaluating the fidelity of these estimates developed and applied by myself to the fractal analysis techniques under consideration. In order to probe the robustness of these techniques, it is necessary to compare their performance on traces with a known Hurst exponent or fractal dimension. To introduce a method for producing such traces, we begin with a general discussion of noise traces.

3.5.1. Colored Noises

There are a variety of means of quantifying the character of a noise trace. In addition to the aforementioned metrics of space-filling character and long-range correlations, an analysis of the spectral content of a noise trace leads to a natural quantification of the trace's statistical properties. An important and wide-ranging class of noise traces is that of power-law noise, whose power spectral density $P(f) \propto 1/f^{\beta}$. Noise characterized by $\beta = 0$ thus represents noise whose spectral power density is a constant across all frequencies, while $\beta = 1$ corresponds to the '$1/f$ noise' often found in natural systems, and $\beta = 2$ corresponds to a so-called 'brown noise'. While β can, in principle, assume any value, we begin our investigation by considering the $\beta = 2$ case.

A noise trace characterized by a power spectral density with $\beta = 2$ is termed 'brown noise' owing to its relation to Brownian motion, which describes the net motion of a particle whose individual steps are random and independent. A Brownian motion may exist as a structure in a system of any dimension, but for our purposes, we consider a brown noise as a plot of the position of a particle undergoing Brownian motion in one dimension as a function of time (in the discussion that follows, 'Brownian motion' and 'brown noise' will be used interchangeably to describe a Brownian motion in one dimension). In this sense, given that a Brownian motion represents the cumulative sum of random, independent steps, a Brownian motion trace is readily generated as a cumulative integral of a white noise trace, which for our purposes we can define as a series of values with zero mean taken from a normal distribution (i.e., a Gaussian noise trace; see Fig. 3.16). As a result, a brown noise trace is characterized by a Hurst exponent of $H = 0.5$.

If we relax the restriction that the Gaussian noise trace consist of independent increments, such that consecutive increments are positively or negatively correlated, the trace formed by its cumulative sum is then characterized by a Hurst exponent that deviates from $H = 0.5$—such a trace is then known as 'fractional Brownian motion' (fBm). Mandelbrot and Van Ness [39] provide a formalism to such structures as follows: First, consider an ordinary Brownian motion $B(t, \omega)$, where t denotes

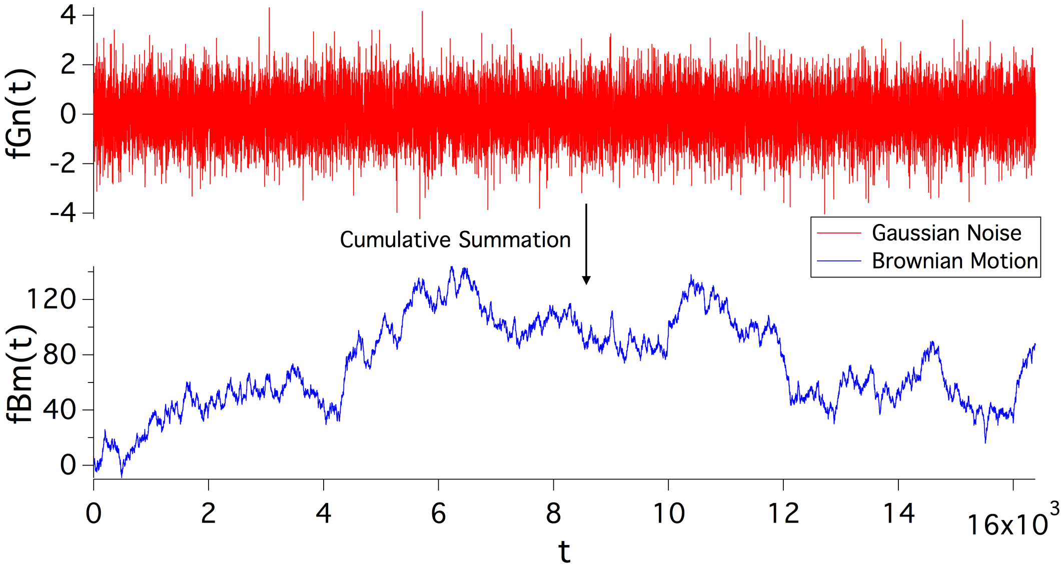

FIGURE 3.16. The cumulative sum of Gaussian white noise results in Brownian motion.

time and ω denotes the set of values corresponding to the random function that gives way to the specific realization of a Brownian motion (i.e., the series of random steps whose cumulative summation results in a Brownian motion). A Brownian motion $B(t,\omega)$ is a real-valued function whose increments $B(t_2,\omega) - B(t_1,\omega)$ have zero mean and variance $|t_2 - t_1|$, and whose non-overlapping increments $B(t_2,\omega) - B(t_1,\omega)$ and $B(t_4,\omega) - B(t_3,\omega)$ are independent. A 'reduced fractional Brownian motion' $B_H(t,\omega)$ then, is further characterized by the parameter H, $0 < H < 1$, and satisfies

$$\begin{aligned} B_H(0,\omega) &= b_0, \\ B_H(t,\omega) - B_H(0,\omega) &= \frac{1}{\Gamma(H+\frac{1}{2})}\left\{\int_{-\infty}^{0}\left[(t-s)^{H-1/2} - (-s)^{H-1/2}\right] dB(s,\omega) \right. \\ &\quad \left. + \int_0^t (t-s)^{H-1/2} dB(s,\omega)\right\}. \qquad \text{(Equation 3.6)} \end{aligned}$$

A fractional Brownian motion trace is thus self-affine in the sense that

$$\{B_H(t_0+\tau,\omega)-B_H(t_0,\omega)\} \triangleq \{h^{-H}[B_H(t_0+h\tau,\omega)-B_H(t_0,\omega)]\}, \quad \text{(Equation 3.7)}$$

where $\{X(t,\omega)\} \triangleq \{Y(t,\omega)\}$ indicates that two random functions $X(t,\omega)$ and $Y(t,\omega)$ have the same finite joint distribution functions [39]. That is, on average, when an interval on an fBm trace is expanded by a factor of h, the difference of the values bounding the interval $B_H(t_0+h\tau,\omega)-B_H(t_0,\omega)$ increases by a factor of h^H. This is thus an example of statistical self-affinity, as it represents a transformation in which the x and y axes need to be scaled by distinct factors (*viz.*, h and h^H, respectively) in order to observe the preservation of statistical properties. By contrast, a statistically self-similar structure is one whose statistical properties are preserved upon an isotropic rescaling [34].

This definition of self-affinity in terms of the Hurst exponent then allows us to draw a parallel between the Hurst exponent and the fractal dimension. Following the argument of Voss [34], consider an fBm trace $V_H(t)$ covering a time span $\Delta t = 1$ and a vertical range $\Delta V_H = 1$. If the time span is divided into n increments each of width $1/n$, then we expect each interval to contain a portion of the trace whose vertical range is $\Delta t^H = 1/n^H$ (see Fig. 3.17). Then, we would further expect the portion of $V_H(t)$ present in each interval to be covered by $\Delta V_H/\Delta t = (1/n^H)/(1/n) = n/n^H$ square boxes of side length $1/n$. Hence, the total number of square boxes of side length $1/n$ required to cover the entire trace is expected to be $n(n/n^H) = n^{2-H}$. Recall that the box-counting method of estimating fractal dimension finds the number of square boxes of side length ℓ needed to cover a trace follows $N(\ell) \propto (1/\ell)^{D_F}$; comparing these results leads to the relationship[4] $D_F = 2 - H$.

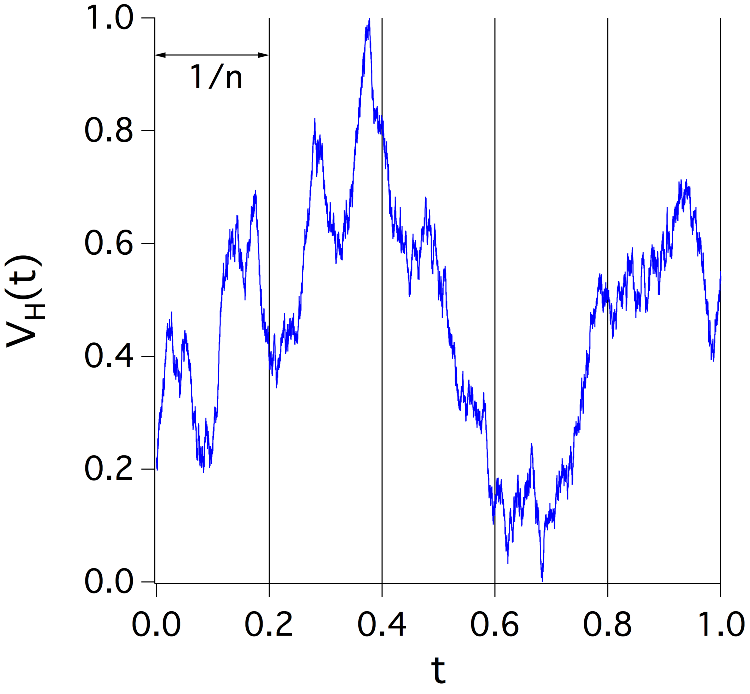

FIGURE 3.17. Deriving a relationship between the Hurst exponent and fractal dimension. A Brownian motion trace $V_H(t)$ $(H = 0.5)$ is rescaled to fit inside a unit square, and is divided into n intervals of width $1/n$. The self-affine nature of an fBm trace leads to a prediction for the number of square boxes needed to cover the trace at a given length scale, leading to a relationship between H and D_F. See text for details.

In spite of the ubiquity of the relation $D_F = 2 - H$ found in the literature, Voss is quick to note the inherent difficulty in assigning a fractal dimension to a self-affine structure, as this argument requires fixing a scaling between distinct coordinates. Mandelbrot, too, notes the apparent relation $D_F = 2 - H$ [40], and clarifies that this relation holds in the fine-scale limit. Indeed, this disparity highlights a general distinction between the Hurst exponent and the fractal dimension as descriptors of a time-series trace; namely, the former is a descriptor of global correlations, while the latter describes a trace's local fine-scale structure [41].

---

[4] Note that this relation only applies to time-series fractals, since the notion of a Hurst exponent is undefined for spatial fractals.

3.6. Relationship between Fractal Dimension and Spectral Exponent

We now return briefly to the spectral exponent β as a means of describing the nature of a fractal trace. In practice, it is uncommon to describe the fractal properties of a time-series structure by means of a spectral analysis, owing to the imprecision (relative to the aforementioned fractal analysis techniques) of fitting a spectral decomposition of a trace using a power law. Nonetheless, it remains instructive to observe the relationship that exists between the spectral exponent β, the fractal dimension D_F, and the Hurst exponent H. The spectral exponent is typically said to relate to the Hurst exponent at $\beta = 2H+1$, implying the relationship $D_F = (5-\beta)/2$. This relationship derives from the observation that the two-point autocorrelation function

$$G_V(\tau) = \langle V(t)V(t+\tau)\rangle - \langle V(t)\rangle^2 \propto \tau^{\beta-1} \qquad \text{(Equation 3.8)}$$

for a trace $V(t)$ is related to the quantity $\langle |V(t_\tau) - V(t)|^2\rangle$ as

$$\langle |V(t_\tau) - V(t)|^2\rangle = 2[\langle V^2\rangle - G_V(\tau)]; \qquad \text{(Equation 3.9)}$$

comparing this result to the variance method for the determination of the Hurst exponent

$$\langle |V(t+\tau) - V(t)|^2\rangle \propto \tau^{2H} \qquad \text{(Equation 3.10)}$$

leads to the expression $\beta - 1 = 2H$ [42]. However, systematic study [43] has shown that such a relationship does not generally hold. In analogy to the investigation performed by Ref. [43], we investigated this relationship by generating a collection of 20 noise traces with a length of 16384 points at each of 40 evenly spaced values of β between 0 and 2. The results of fractal analyses on these traces are displayed in Fig. 3.18, and demonstrate that the relationship $D_F = (5 - \beta)/2$ breaks down for D_F close to 1 or 2.

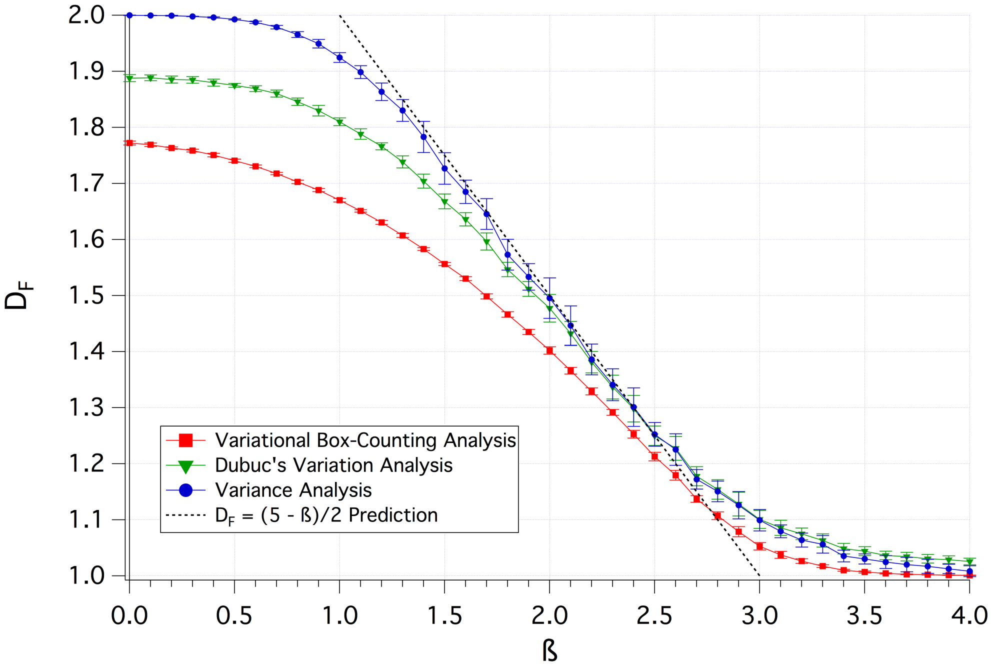

FIGURE 3.18. Results of fractal analysis on colored noise traces generated with a specified power spectral density β. Each data point represents the average value of D_F measured for the set of 20 traces at the corresponding value of β. Error bars represent one standard deviation from the mean value of D_F recorded for each set of traces. Lines connecting the data points are provided as a guide to the eye.

3.7. Generating and Characterizing Fractional Brownian Motions

A variety of methods exist for generating a random realization of a fractional Brownian motion trace with arbitrary Hurst exponent, including Fourier filtering of white noise, random midpoint displacement, and the summation of independent jumps [42]. The randomly generated fBm traces discussed in this dissertation are created using a Matlab program that creates a fractional Gaussian noise trace via a Fourier transform, and takes the cumulative sum of the noise trace to yield a fractional Brownian motion trace with a specified well-defined Hurst exponent.

While these computer-generated fBm traces are created using a well-defined Hurst exponent, they may realistically only be considered to be approximations to true fractal fractional Brownian motions—as with any structure that appears in the physical world, generated fBm traces necessarily exhibit a fine-scale resolution limit (time intervals shorter than the fundamental interval Δt are undefined) as well as a coarse-scale size limit (time intervals longer than the total length of the trace are undefined). Nonetheless, given a generated fBm trace whose total length exceeds its minimum step by several orders of magnitude, the effects of these limitations on analytical estimates of the underlying Hurst exponent characterizing the trace may be considered negligible.

We therefore assume that a fBm trace generated with a Hurst exponent H_{in} and with a total length well in excess of its resolution limit is a suitable representative of a true fractal structure characterized by H_{in}, and may therefore be used as a test case against which the fidelity of the above-mentioned analysis techniques may be evaluated. The procedure for evaluating these analytical procedures is thus as follows: We first generate a set of 50 16384-point fBm traces at each of 39 input Hurst exponents H_{in} between 0.025 and 0.975. Next, each of these traces is passed through the analysis method in question, which returns either a measured Hurst exponent H_{out} or a measured fractal dimension D_{out}. In the case of the Dubuc variation analysis, which returns a fractal dimension, this value is "converted"[5] to a Hurst exponent via $H_{\text{out}} = 2 - D_{\text{out}}$. For each fractal analysis method, the respective scaling plots were assessed between length scales corresponding to five points on the trace and 1/5 of the trace's entire length.

Having extracted these values of H_{out} for each sample fBm trace, we may produce a plot of H_{out} vs H_{in} for each analysis technique; these results are displayed in Figs. 3.19 and 3.20 for randomly-generated fBm traces with lengths of 16384 points and 512 points, respectively. In the ideal case of a perfectly fractal fBm trace subjected to an analysis technique that produces a precise and accurate of the Hurst exponent, such a plot is expected to be linear with unity slope. Based on the results of these analyses, we may note that in general, the variational box-counting method tends to over-estimate H except in the case of high H values; the variance analysis tends to under-estimate H; the Dubuc variation analysis performs well only for $H \sim 0.5$; and the adaptive fractal analysis provides an accurate estimate of H throughout the range of H values. These deviations are more pronounced in the case of the shorter, 512-point traces, and the precision of the estimated H values suffer in these cases as well, as evidenced by the increases in the error bars on the data points corresponding to the shorter traces.

We may also investigate the effect on the measured H values of another common deviation from ideal fractal behavior; namely, the behavior of traces whose finest-scale features are significantly larger than their resolution limit. Such is very often the case for fractal structures observed in nature such as magnetoconductance fluctuations, whose finest features are often an order of magnitude larger than the point-wise

---

[5] As discussed above, such a conversion is not rigorously motivated, but it does allow for a self-consistent means of evaluating the behavior of this analysis technique on fBm traces of a known Hurst exponent, as well as deviations from this behavior.

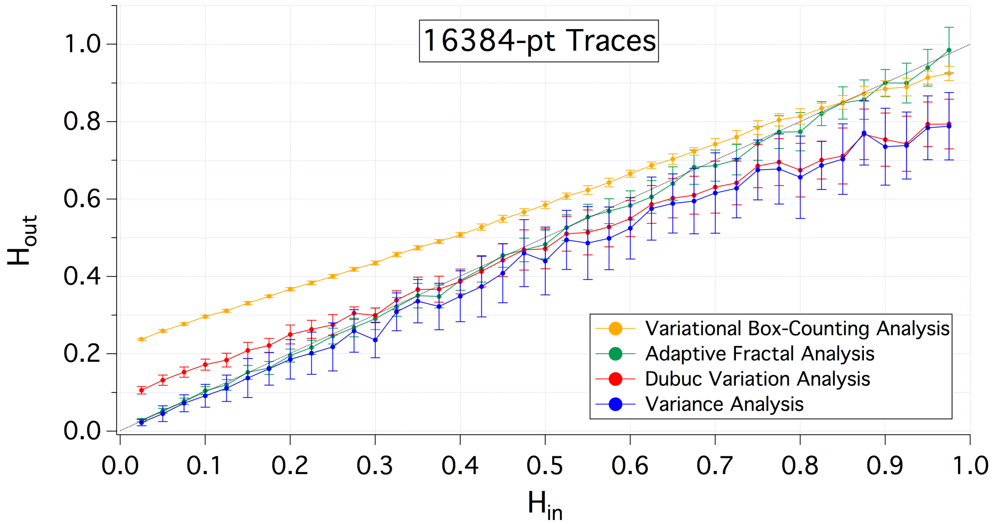

FIGURE 3.19. Results of a Monte Carlo analysis of the fidelity of the four fractal analysis methods in determining the H value for randomly-generated 16384-point fBm traces. Fifty fBm traces were generated at each of 39 input Hurst exponents H_{in} between 0.025 and 0.975 and analyzed using the variational box-counting method (yellow points), adaptive fractal analysis (green points), Dubuc's variation analysis (red points), and the variance analysis (blue points). Each data point represents the average H_{out} value measured for each analysis method using cutoffs corresponding to five data points and 1/5 of the entire trace; the error bars represent one standard deviation in the measured values. The dashed black line represents the relation $H_{\text{out}} = H_{\text{in}}$, such that data points representing traces whose measured H_{out} values exactly match their generating H_{in} values would fall on this line.

resolution of the trace. To probe the nature of this effect, we repeat the above technique on a set of randomly-generated 512-point fBm traces which have been subjected to a Fourier filter which eliminates all frequency components corresponding to periods shorter than 10 data points, such that the resultant traces have a minimum feature size of 10 points. Figure 3.21 demonstrates the result of this filtering procedure by comparing the original and filtered versions of an fBm trace with $H_{\text{in}} = 0.5$.

A fractal analysis of time-series traces with limited spectral content such as these requires a reassessment of the length scales over which one expects to find the fractal scaling properties. Whereas our analysis of fBm traces whose spectral content

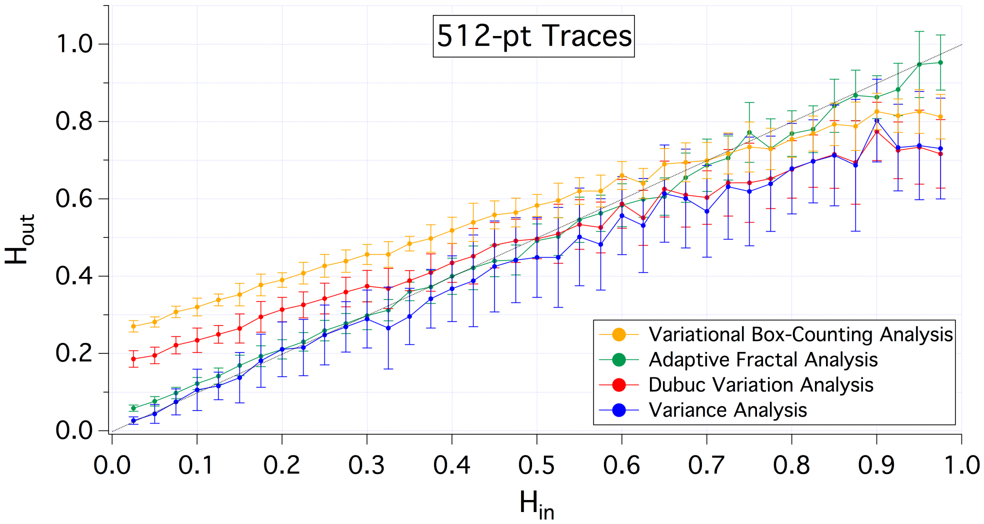

FIGURE 3.20. Results of a Monte Carlo analysis of the fidelity of the four fractal analysis methods in determining the H value for randomly-generated 512-point fBm traces. Fifty fBm traces were generated at each of 39 input Hurst exponents H_{in} between 0.025 and 0.975 and analyzed using the variational box-counting method (yellow points), adaptive fractal analysis (green points), Dubuc's variation analysis (red points), and the variance analysis (blue points). Each data point represents the average H_{out} value measured for each analysis method using cutoffs corresponding to five data points and 1/5 of the entire trace; the error bars represent one standard deviation in the measured values. The dashed black line represents the relation $H_{\text{out}} = H_{\text{in}}$, such that data points representing traces whose measured H_{out} values exactly match their generating H_{in} values would fall on this line.

extended down to the resolution limit examined scaling properties to a minimum length scale of five data points, we now cannot expect to see such scaling properties at length scales smaller than our minimum feature size of 10 data points. It may seem reasonable, then, to expect that we should be able to set our fine-scale analysis cutoff at 10 data points and observe the desired scaling properties at all length scales greater than this; in practice, however, the effect of a significant minimum feature size is manifest in a fractal analysis even at length scales greater than that minimum feature size. The results of passing the 512-point Fourier filtered fBm traces through our fractal analysis techniques are displayed in Figs. 3.22 and 3.23, in which the fine-

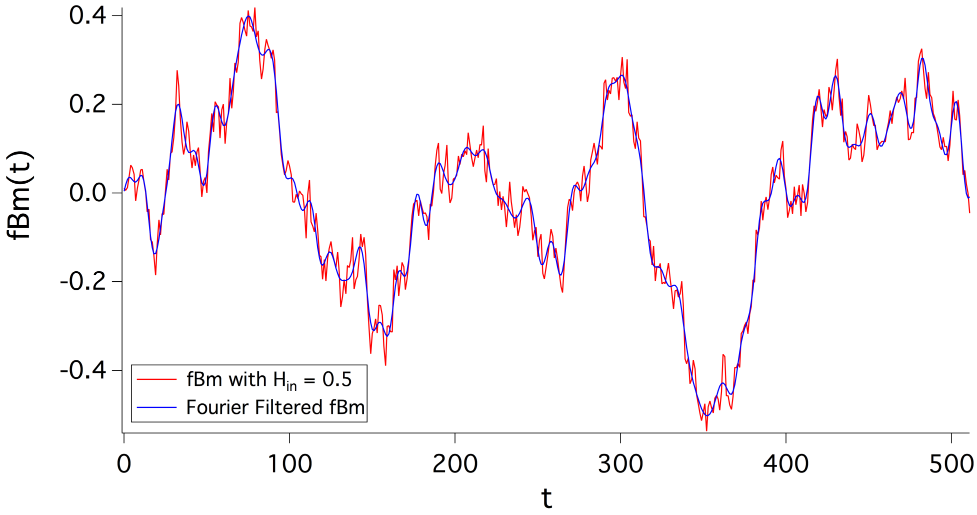

FIGURE 3.21. Comparison of a 512-point fBm trace with $H_{\text{in}} = 0.5$ before (red) and after (blue) Fourier filtering to a minimum feature size of 10 points.

scale cutoffs for the analysis are 10 data points (the traces' minimum feature size) and 20 data points, respectively.

Examples of the scaling plots from which the data in Figs. 3.20, 3.22, and 3.23 were taken are provided in Figs. 3.24, 3.25, 3.26, and 3.27. These figures show the scaling plots resulting from fractal analyses of an fBm trace with $H_{\text{in}} = 0.5$ before and after Fourier filtering (*viz.*, the pair displayed in Fig. 3.21) using the variational box-counting method, the variance method, the Dubuc variation method, and adaptive fractal analysis, respectively. These figures demonstrate the difficulty in identifying an appropriate fine-scale cutoff for fractal analysis of a time-series trace, even when the minimum feature size found in the trace is easily identifiable. Unlike spatial fractals, for which it is often reasonable to expect fractal scaling behavior between the length scales corresponding to physical constraints (and in particular at length scales sufficiently far from these cutoffs), the effect of imposing a minimum feature size on a time-series trace is found at all scales, not just those smaller than the minimum observed period.

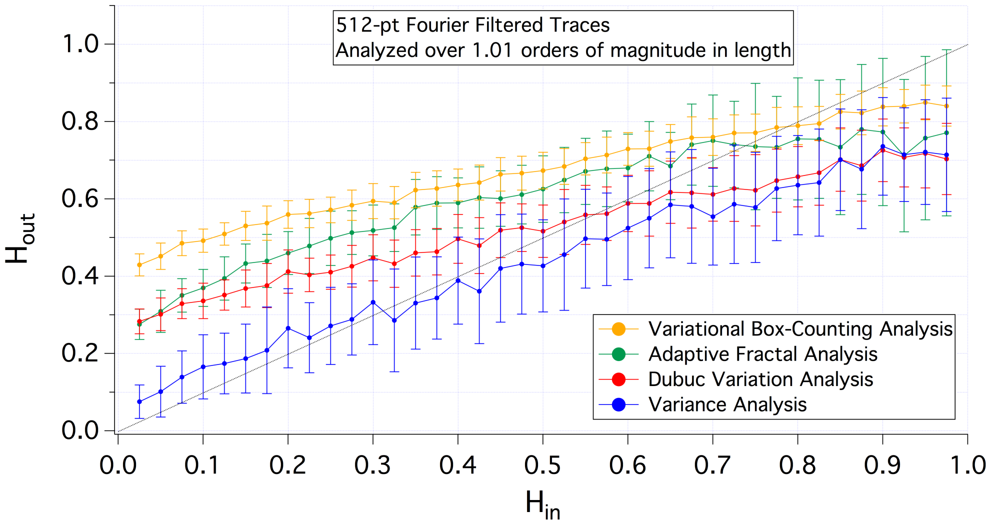

FIGURE 3.22. Results of a Monte Carlo analysis of the fidelity of the four fractal analysis methods in determining the H value for randomly-generated 512-point fBm traces Fourier filtered to a minimum feature size of 10 points. The analyses are performed over 1.01 orders of magnitude in length scale. Fifty fBm traces were generated at each of 39 input Hurst exponents H_{in} between 0.025 and 0.975 and analyzed using the variational box-counting method (yellow points), adaptive fractal analysis (green points), Dubuc's variation analysis (red points), and the variance analysis (blue points). Each data point represents the average H_{out} value measured for each analysis method using cutoffs corresponding to 10 data points and 1/5 of the entire trace; the error bars represent one standard deviation in the measured values. The dashed black line represents the relation $H_{\text{out}} = H_{\text{in}}$, such that data points representing traces whose measured H_{out} values exactly match their generating H_{in} values would fall on this line.

The trends displayed in Figs. 3.22 and 3.23, as contrasted with those displayed in Figs. 3.19 and 3.20, highlight the difficulty in assessing the fractal properties of time-series structures that suffer from limited length, limited spectral content, or both. The effect on a time-series trace of a minimum feature size significantly in excess of its resolution limit necessitates restricting a fractal analysis to length scales larger still than the minimum feature size, which often leads to an analysis of scaling properties over few orders of magnitude in length. For instance, restricting the fractal analysis of the 512-point Fourier filtered traces between cutoffs corresponding to 10 data points

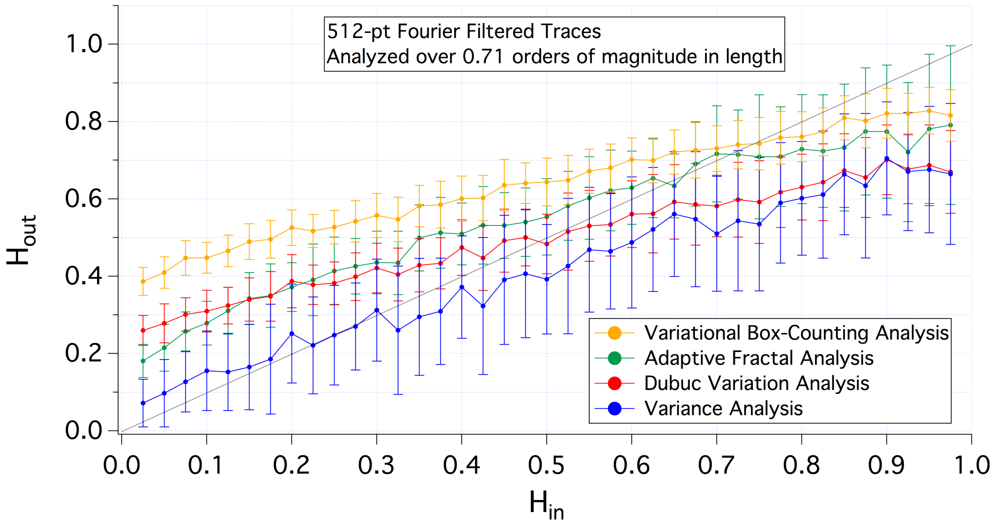

FIGURE 3.23. Results of a Monte Carlo analysis of the fidelity of the four fractal analysis methods in determining the H value for randomly-generated 512-point fBm traces Fourier filtered to a minimum feature size of 10 points. The analyses are performed over 0.71 orders of magnitude in length scale. Fifty fBm traces were generated at each of 39 input Hurst exponents H_{in} between 0.025 and 0.975 and analyzed using the variational box-counting method (yellow points), adaptive fractal analysis (green points), Dubuc's variation analysis (red points), and the variance analysis (blue points). Each data point represents the average H_{out} value measured for each analysis method using cutoffs corresponding to 20 data points and 1/5 of the entire trace; the error bars represent one standard deviation in the measured values. The dashed black line represents the relation $H_{\mathrm{out}} = H_{\mathrm{in}}$, such that data points representing traces whose measured H_{out} values exactly match their generating H_{in} values would fall on this line.

and 1/5 of the trace length yields an analysis over barely more than one order of magnitude in length scale; attempting to increase the accuracy of the measurement by raising the fine-scale cutoff to 20 data points reduces the scaling range to 0.71 orders of magnitude. Given that it is difficult to make a compelling argument for the presence of fractal behavior when examining such a narrow range of length scales, one must take care when applying these analysis techniques to data sets limited in length or spectral content. Nevertheless, it is instructive to examine the behavior of fractal

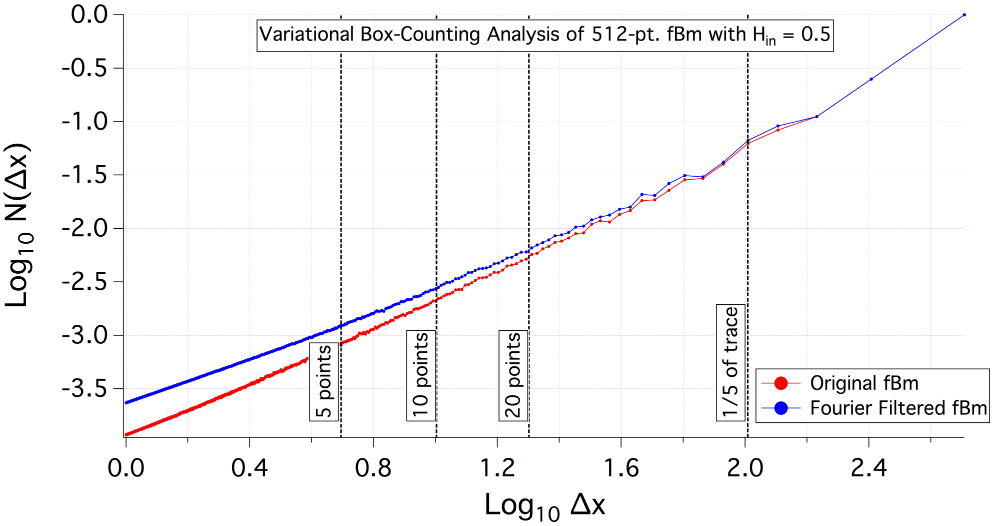

FIGURE 3.24. Comparison of scaling plots produced by the variational box-counting method applied to a 512-point fBm trace with $H_{\text{in}} = 0.5$ before (red) and after (blue) Fourier filtering to a minimum feature size of 10 points. The vertical dashed lines indicate the cutoffs between which the scaling plot is fitted with a straight line whose slope yields D_F (and is then converted to H_{out}): For both traces, the coarse-scale cutoff is given by the line labeled '1/5 of trace'. The fine-scale cutoff for the unfiltered trace (red points) is given by the line labeled '5 points' (corresponding to the data in Fig. 3.20), while the fine-scale cutoff for the filtered trace (blue points) may be chosen as 10 data points (corresponding to the data in Fig. 3.22) or 20 data points (corresponding to the data in Fig. 3.23).

analysis applied to legitimate fractal structures such as fBm traces which have been artificially subjected to such constraints.

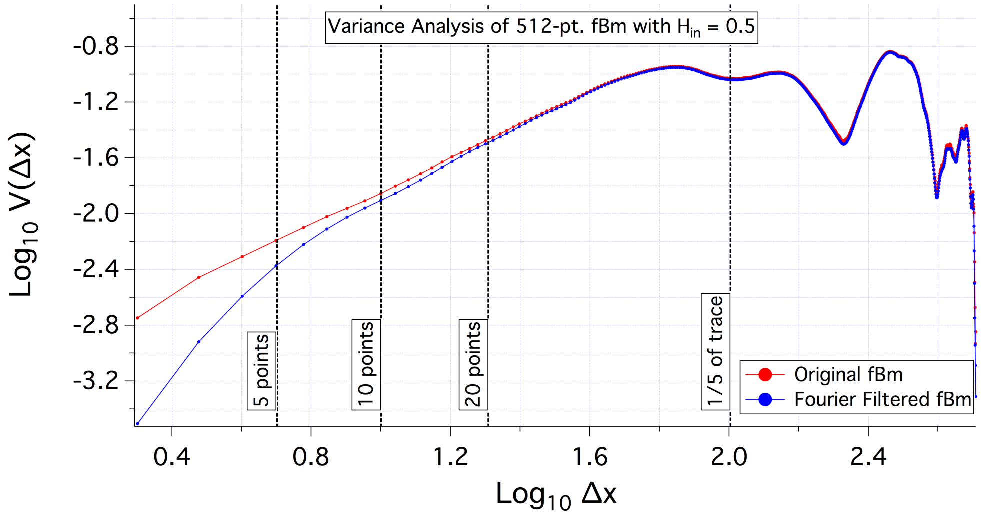

FIGURE 3.25. Comparison of scaling plots produced by the variance method applied to a 512-point fBm trace with $H_{\mathrm{in}} = 0.5$ before (red) and after (blue) Fourier filtering to a minimum feature size of 10 points. The vertical dashed lines indicate the cutoffs between which the scaling plot is fitted with a straight line whose slope yields H_{out}: For both traces, the coarse-scale cutoff is given by the line labeled '1/5 of trace'. The fine-scale cutoff for the unfiltered trace (red points) is given by the line labeled '5 points' (corresponding to the data in Fig. 3.20), while the fine-scale cutoff for the filtered trace (blue points) may be chosen as 10 data points (corresponding to the data in Fig. 3.22) or 20 data points (corresponding to the data in Fig. 3.23).

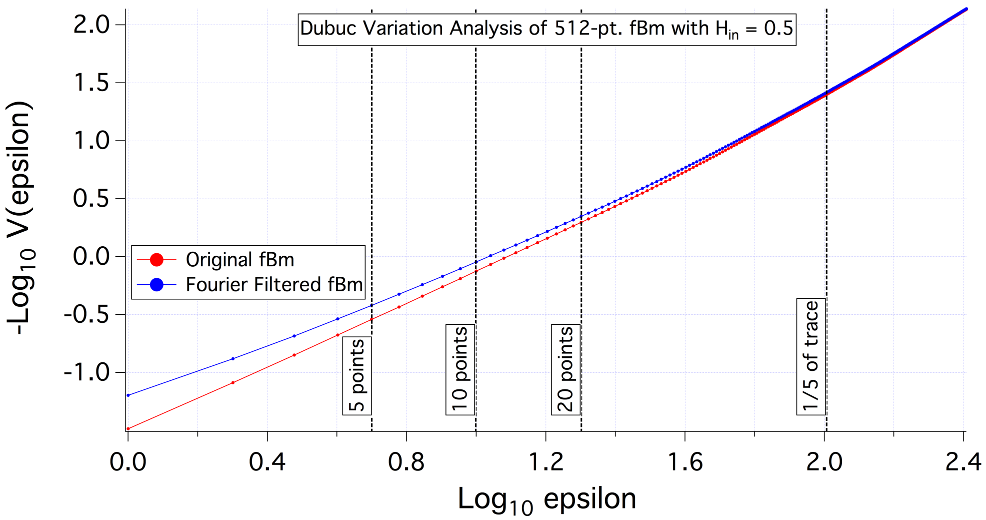

FIGURE 3.26. Comparison of scaling plots produced by the Dubuc variation method applied to a 512-point fBm trace with $H_{\text{in}} = 0.5$ before (red) and after (blue) Fourier filtering to a minimum feature size of 10 points. The vertical dashed lines indicate the cutoffs between which the scaling plot is fitted with a straight line whose slope yields D_F (and is then converted to H_{out}): For both traces, the coarse-scale cutoff is given by the line labeled '1/5 of trace'. The fine-scale cutoff for the unfiltered trace (red points) is given by the line labeled '5 points' (corresponding to the data in Fig. 3.20), while the fine-scale cutoff for the filtered trace (blue points) may be chosen as 10 data points (corresponding to the data in Fig. 3.22) or 20 data points (corresponding to the data in Fig. 3.23).

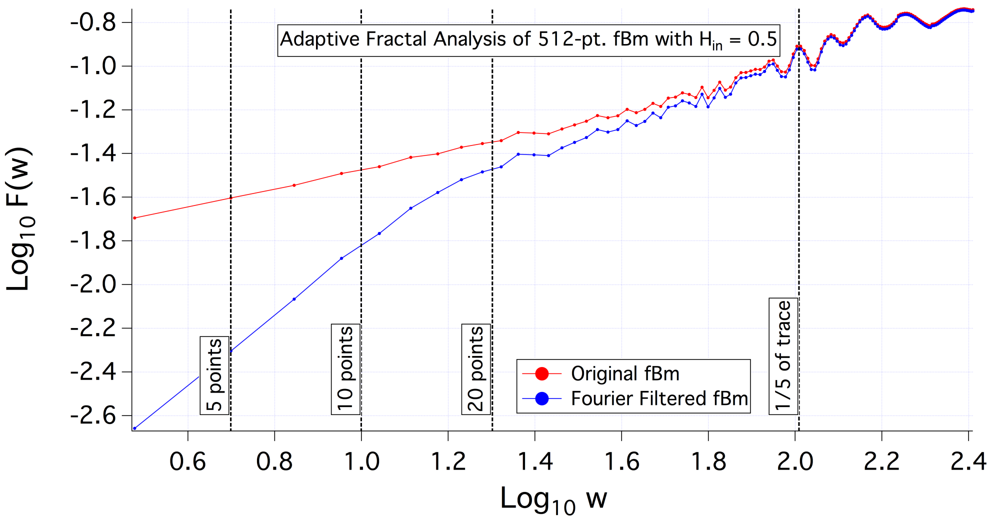

FIGURE 3.27. Comparison of scaling plots produced by the adaptive fractal analysis method applied to a 512-point fBm trace with $H_{\text{in}} = 0.5$ before (red) and after (blue) Fourier filtering to a minimum feature size of 10 points. The vertical dashed lines indicate the cutoffs between which the scaling plot is fitted with a straight line whose slope yields H_{out}: For both traces, the coarse-scale cutoff is given by the line labeled '1/5 of trace'. The fine-scale cutoff for the unfiltered trace (red points) is given by the line labeled '5 points' (corresponding to the data in Fig. 3.20), while the fine-scale cutoff for the filtered trace (blue points) may be chosen as 10 data points (corresponding to the data in Fig. 3.22) or 20 data points (corresponding to the data in Fig. 3.23).

CHAPTER IV

FRACTAL ANALYSIS OF MCF TRACES

As discussed in the introduction, a fractal analysis of MCF traces may provide insights regarding the phase space characterizing electron trajectories within the billiard. Specifically, the presence of fractal patterns is understood to be suggestive of a mixture of chaos and stability in this phase space [14]. Although electron billiards fabricated on the gated AlGaAs/GaAs heterostructure generally exhibit soft confinement potentials which may serve to introduce chaotic trajectories [14], it remains an open question whether the electrostatic potential landscape introduced by the modulation doping fabrication technique is itself sufficient to affect the fractal content.

With this in mind, we now turn our attention to a fractal analysis of MCF traces taken on electron billiards in the modulation-doped and undoped AlGaAs/GaAs heterostructure systems. These billiards share a nominally square shape and a soft-walled confinement potential from the electrostatic gates which serve to define the billiard; however, the undoped device is free of the ionized dopants which serve to impact the distribution of electron trajectories in the modulation-doped structures. Is this difference substantial enough to yield an observable effect on the fractal properties of the MCF? In particular, could the existence of small-angle scattering sites in the modulation-doped structures introduce chaotic dynamics that serve to amplify the fractal behavior of the MCF?

4.1. Generating Simulated Traces

4.1.1. MCF and fBm

Figure 4.1 displays the representative MCF traces from the modulation-doped and undoped AlGaAs/GaAs electron billiards whose relative fractal properties we seek to assess[1]. All 12 MCF were measured at a temperature of 240 mK. For the purposes of this analysis, we refer to the MCF traces produced by modulation-doped electron billiards as 'MD-MCF' and those produced by undoped electron billiards as 'UD-MCF'. For each family of traces, we restrict our analysis to the magnetic field range $0 \leq B \leq B_{\text{cyc}}$, where the cyclotron fields B_{cyc} for the modulation-doped and undoped electron billiards are 160 mT and 210 mT, respectively. Also note that the traces represented in Fig. 4.1 have each been vertically rescaled to have an RMS amplitude of 1 and have had any linear trend removed by subtracting a best-fit line from the trace. The vertical rescaling has no effect on the results of the fractal analyses, but allows for a clear and consistent visualization of the traces' fluctuations. The removal of a linear trend ensures that our analysis treats only the quantum fluctuations resulting from phase-coherent electron transport through the billiards; see Section 5.3 for a discussion of this linear trend.

As we saw in Chapter III, the accuracy and precision of a fractal analysis of a time-series trace suffer when the trace's total length does not significantly exceed the smallest feature size found in the trace. Such is the case for the MCF traces under consideration here: the MD-MCF traces each consist of 320 points at a resolution of 0.5 mT and exhibit a minimum feature size of roughly 4 mT (1.3 percent of the total length), while the UD-MCF traces each consist of 420 points at a resolution

---

[1] The MCF traces measured on the induced AlGaAs/GaAs heterostructure were measured by Drs. Andrew See and Adam Micolich and published in Ref. [27].

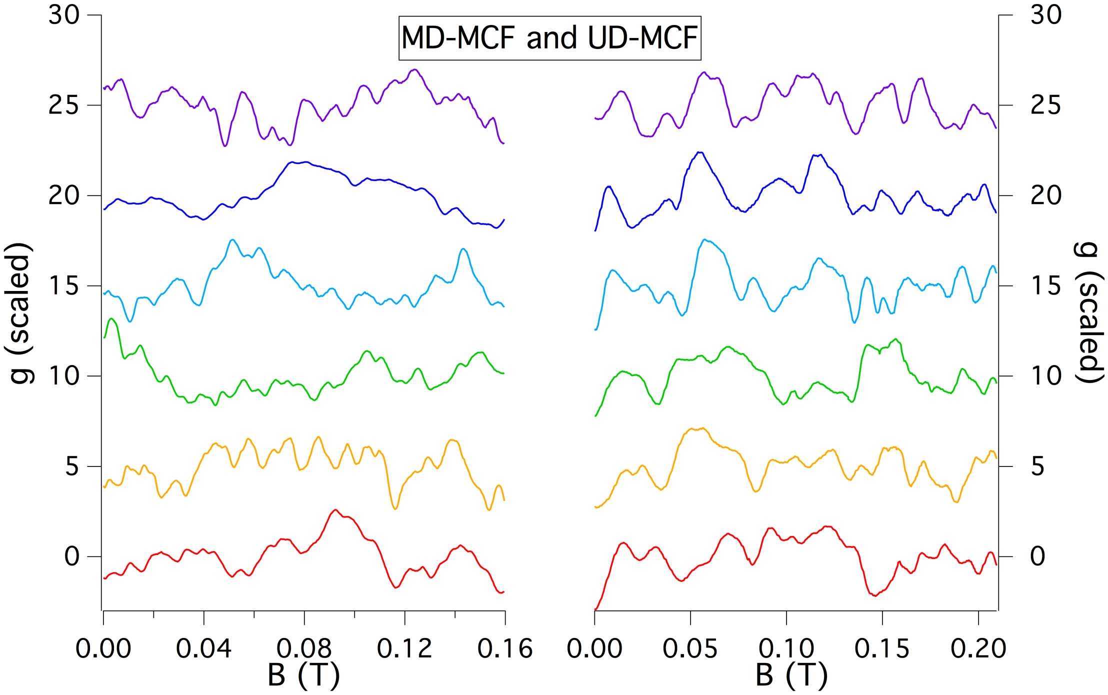

FIGURE 4.1. Magnetoconductance fluctuations measured on modulation-doped (left) and induced (right) electron billiards. All traces have been rescaled to have an RMS amplitude of 1. The six MD-MCF were each measured on different cooldowns from room temperature, while the six UD-MCF were measured in a single cooldown at different top gate voltages. All traces have been vertically offset for clarity.

of 0.5 mT and exhibit a minimum feature size of roughly 8 mT (1.9 percent of the total length). We therefore expect that a straightforward application of the analysis techniques described in Chapter III may not be sufficient to discriminate between the fractal characteristics of each family of MCF traces. Instead, we seek to examine the relative fractal characteristics of these MCF traces through a comparison against the behavior of simulated fractal traces which have been artificially smoothed.

We have at our disposal a technique for generating fractional Brownian motion (fBm) traces with arbitrary length and specified Hurst exponent, whose response to our fractal analysis techniques are documented in Chapter III. These fBm traces exhibit clear fractal scaling properties when their length far exceeds their minimum feature size, but the robustness of these properties is observed to diminish when the fBm traces are passed through a Fourier filtering algorithm. It may be claimed, however, that the filtered fBm traces represent fractal structures whose analyses are impeded by constraints which limit their spectral content.

With this in mind, let us propose by analogy that the measured MCF traces under consideration represent true fractal structures whose fractal analyses are impeded by a lack of spectral content owing to a physical constraint such as a finite phase-coherence length. To explore the validity of this hypothesis, we seek to compare the responses of our measured MCF traces and appropriately prepared fBm traces to our fractal analysis techniques. Because we wish to test the hypothesis that each MCF trace represents a fractal structure which has had its spectral content diminished, we seek to pair each MCF trace with a fBm trace whose basic properties upon Fourier filtering closely match those of the MCF, and subsequently examine the response of each trace to each fractal analysis method.

Our investigation thus proceeds as follows: For each of the 12 total MCF traces under consideration, we generate a set of fBm traces which are then resized and Fourier filtered so as to match the MCF's total length and minimum feature size (measured in numbers of data points). From this set of fBm traces, we identify the fBm trace whose measured H_{out} values most closely match those of the corresponding MCF trace. The scaling plots from which the H_{out} values are taken are then examined under the assumption that a scaling plot that is better fit by a straight line (in the appropriate scaling range) may be said to correspond to a trace that is more fractal. Under the hypothesis that the MCF traces are "as fractal" as their corresponding fBm traces, we would expect scaling plots for the MCF and fBm traces to yield similar deviations from linearity. If, on the other hand, one family of MCF traces are shown to yield scale plots that are consistently less linear than those of their corresponding fBm traces, we may say that that set of MCF traces is “less fractal” than the other set.

4.1.2. Trace Generating and Processing Procedure

It has been shown in Section 3.7 that Fourier filtering affects the measured fractal dimension or Hurst exponent of a trace in a largely unpredictable manner: our simulations demonstrate that a set of fBm traces generated using a given Hurst exponent H_{in} and subsequently passed through a Fourier filter will yield measured Hurst exponents H_{out} with a significant range of values; see Figs. 3.22 and 3.23. Thus, in order to identify the filtered fBm traces which most resemble our measured MCF, it is necessary to generate several fBm traces using a variety of “seed” Hurst exponents H_{in} and select from that batch those traces whose measured properties after filtering most closely match those of our MCF. To this end, we have generated 500 fBm traces with lengths of 512 points at each H value from 0.1, 0.2, . . ., 0.9 for each family of MCF, producing 4500 fBm candidate traces to compare with the six MCF in each family.

The Fourier filter smoothing is then performed on each trace as follows: Compute the FFT spectrum of the “raw” 512-point fBm trace, and set equal to zero all frequency components corresponding to periodicities smaller than the minimum desired period. Next, compute the inverse-FFT of this spectrum, and crop this reconstituted trace to the desired length (i.e., the same number of data points as the corresponding MCF) by removing points symmetrically from the beginning and end of the trace. Choosing a central selection of points in this way serves to eliminate any undesired artifacts found at either end of the filtered trace resulting from the FFT operations. Finally, compute the best-fit line to the remaining trace using a least-squares algorithm, and subtract this line from the trace, yielding a trace with no overall linear trend.

4.2. Analyzing the Simulated Traces

Each of these 4500 smoothed and cropped traces is then subjected to each of three time-series fractal analysis techniques: the Dubuc variation method, the variance method, and adaptive fractal analysis (AFA). Each of these methods is described in detail in Chapter III.

4.2.1. Identifying the valid scaling region

Before we may extract Hurst exponents or fractal dimensions using these analysis techniques, we need to identify the range in the scaling variable over which we expect the scaling behavior to persist. For this analysis, we have chosen a fine-scale cutoff length corresponding to the minimum feature size observed in the trace—eight points for the MD-MCF and 16 points for the UD-MCF—since we do not see any meaningful variation in the trace at smaller length scales. As a coarse-scale cutoff, we have chosen to use one-fifth of the total length of the trace—64 points for the MD-MCF and 84 points for the UD-MCF. This leads to analyzed scaling ranges of 0.90 orders of magnitude for the MD-MCF and 0.72 orders of magnitude for the UD-MCF.

4.3. Identifying Correspondences

In spite of the inherent limitations of a fractal analysis on a time-series trace with limited spectral content, it should be possible to employ the above analyses to identify smoothed fBm traces whose scaling properties match those of our measured MCF so as to subsequently compare their respective scaling properties. That is, given a collection of filtered fBm traces which respond similarly to the above analyses as our measured MCF, we hope to compare the scaling plots of the MCF to their corresponding filtered fBm counterparts as a means of assessing the relative 'fractality' of the MD-MCF and UD-MCF.

The representative filtered fBm are chosen in a one-to-one correspondence with the 12 measured MCF as follows: For each of the 9000 fBm generated and processed (500 at each of the nine seed Hurst exponents, for each family of MCF), each of the three analyses is performed and their respective measured Hurst exponents recorded. (Note that the Dubuc variation method returns a fractal dimension D_F; this is converted to an 'effective' Hurst exponent via the relation $H = 2 - D_F$.) The same analyses are performed for each of the six MCF in each set, each of which has also had a linear trend subtracted. We are thus left with three H values for each MCF and fBm corresponding to the three analyses, which can be thought of as a point in a three-dimensional 'H-space'. Since we are concerned with identifying the fBm trace whose three measured H values most closely match those of the MCF, we can recast the task as identifying the fBm trace whose point in H-space lies closest to that of the MCF. Specifically, let H_{a}, H_{d}, and H_{v} represent the Hurst exponents measured by AFA, the Dubuc method, and the variation method, respectively, and let the superscripts 1 and 2 label parameters describing an MCF and fBm, respectively; we then seek to minimize the quantity

$$d = \sqrt{[(H_{\mathrm{a}}^1 - H_{\mathrm{a}}^2)^2 + (H_{\mathrm{d}}^1 - H_{\mathrm{d}}^2)^2 + (H_{\mathrm{v}}^1 - H_{\mathrm{v}}^2)^2]}. \qquad \text{(Equation 4.1)}$$

Having done so, we arrived at fBm corresponding to each of our six MD-MCF with an average d of 0.0127, and fBm corresponding to each of our six UD-MCF with an average d of 0.0254. Visual comparisons of the MCF and their corresponding chosen fBm counterparts are shown in Figs. 4.2 and 4.3 (for the MD-MCF and UD-MCF, respectively).

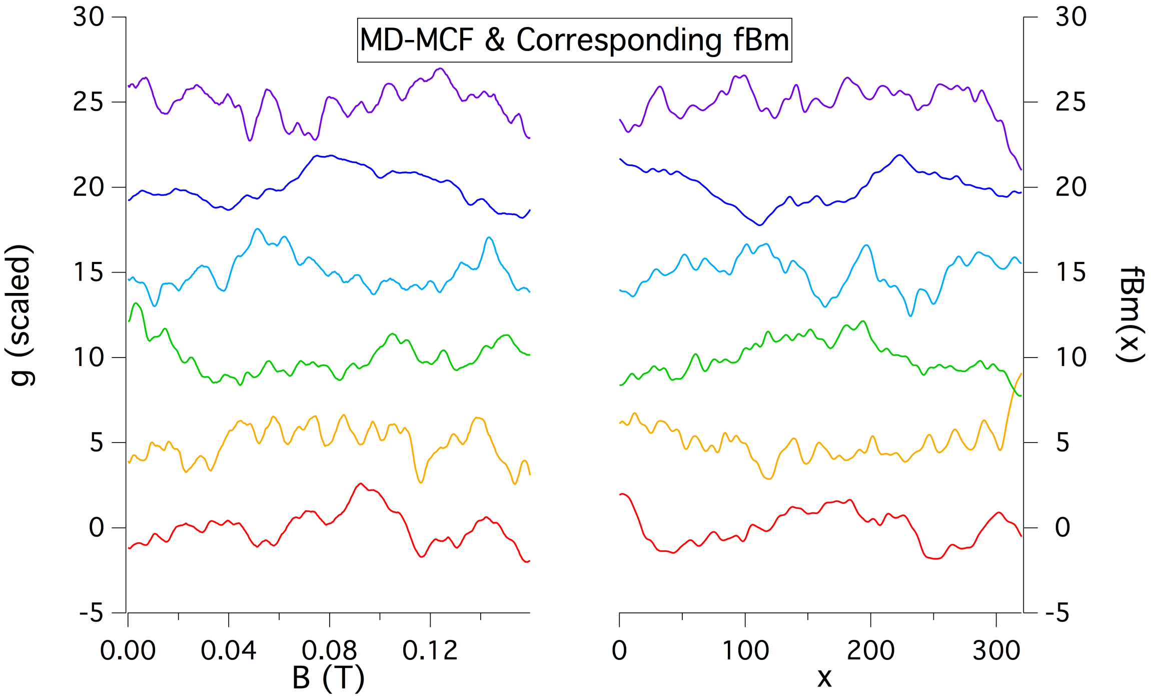

FIGURE 4.2. A comparison of the six MD-MCF traces under consideration (left) and their simulated counterparts (right), chosen such that both traces in a given pair return nearly identical Hurst exponents/fractal dimensions in three separate fractal analyses. All traces consist of 320 data points. The fBm traces have been Fourier filtered to exhibit a minimum feature size of 8 data points as is found in the MCF. All traces have been rescaled to exhibit an RMS amplitude of 1 and are offset for clarity.

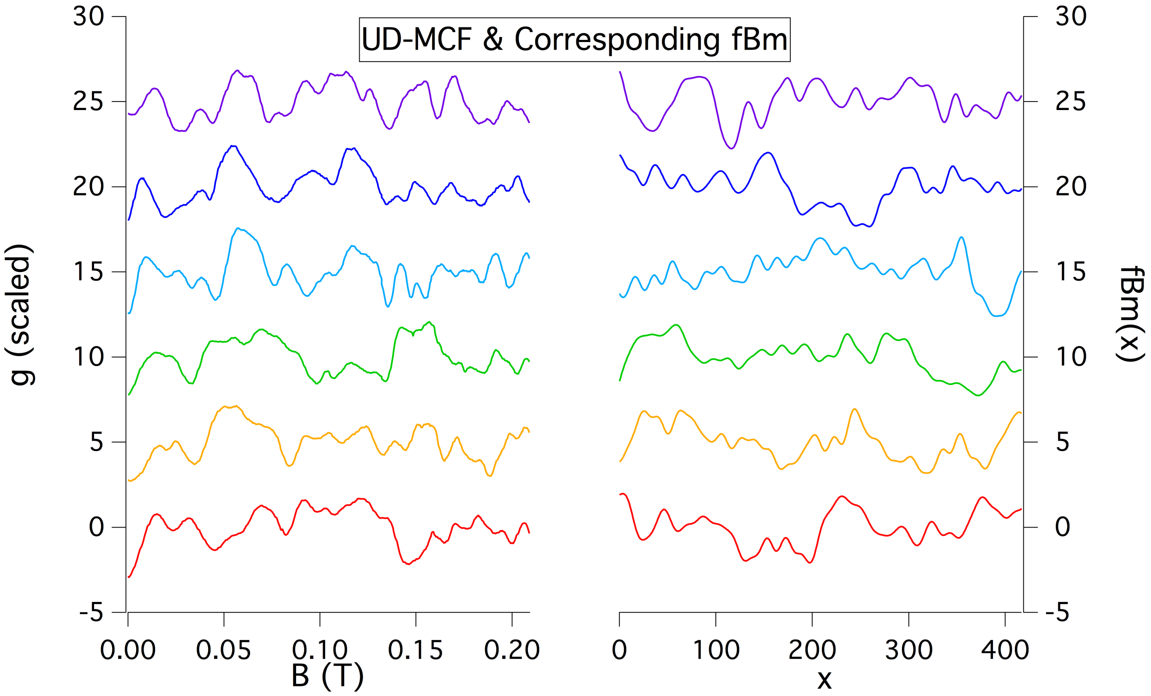

FIGURE 4.3. A comparison of the six UD-MCF traces under consideration (left) and their simulated counterparts (right), chosen such that both traces in a given pair return nearly identical Hurst exponents/fractal dimensions in three separate fractal analyses. All traces consist of 420 data points. The fBm traces have been Fourier filtered to exhibit a minimum feature size of 16 data points as is found in the MCF. All traces have been rescaled to exhibit an RMS amplitude of 1 and are offset for clarity.

4.4. Assessing Scale Plot Pairs

Generally speaking, a structure may be considered to be a fractal if an appropriate scaling plot exhibits a linear trend when plotted logarithmically with a slope corresponding to a non-integer dimension and this linear trend persists over an appreciable range of length scales. Fractal character becomes more difficult to evaluate, however, when one or both of these criteria are broken—when significant curvature appears in the scaling plot, for instance, or when a scaling behavior persists over a short range. This is frequently the case for our measured MCF, where a finite maximum frequency component and short total length tend to distort the results of a fractal analysis. How, then, are we to compare the fractal properties of our two groups of MCF to one another? Given that a direct comparison is unlikely to be informative, we choose to instead compare the fractal character of each group of MCF to groups of filtered fBm traces—traces which were constructed as true fractals but were processed so as to resemble the structures we observe in nature. If we then define a parameter q to capture the fractality of a given trace, then comparing the q values of MCF and their respective fBm across the two groups of MCF should help shed light on the respective fractal character of those two groups.

We choose to define a fitness parameter q that measures the extent to which a scaling plot deviates from perfect linearity within a given range on the scaling plot. Specifically, q represents the standard deviation of the list of differences between the data points and the best-fit line within this range. However, given that scaling plots for the three fractal analyses will exhibit different ranges along the y-axis and the two families of MCF will exhibit scaling trends across different ranges along the x-axis, it is necessary to standardize these scaling plots so that the q values for all plots will be comparable to one another.

As a technique for standardizing the scale plots, we can rescale and translate the data in both dimensions such that the best-fit line through the data is a constant for all the plots considered. In practice, this was implemented as follows: For a given scale plot $y_i = f(x_i)$, cropped to the valid scaling region, with corresponding fit line $f(x) = mx + b$, first translate and rescale the graph along the x axis such that the x-values range between 0 and 1. Next, translate the graph down along the y axis by an amount $b + m/2$ such that the fit line passes through the x axis at $x = 0.5$.

	MCF Trace	$\langle q_{\mathrm{MCF}} \rangle$	fBm Trace	$\langle q_{\mathrm{fBm}} \rangle$	$\Delta\langle q \rangle = \langle q_{\mathrm{MCF}} \rangle - \langle q_{\mathrm{fBm}} \rangle$
	MD1	0.0402	FF8–1	0.0347	0.0054
	MD2	0.1056	FF8–2	0.0857	0.0199
	MD3	0.0395	FF8–3	0.0319	0.0076
	MD4	0.0349	FF8–4	0.0555	-0.0206
	MD5	0.0218	FF8–5	0.0172	0.0046
	MD6	0.0621	FF8–6	0.0727	-0.0106
Averages:		0.0507		0.0496	**0.0011**

	MCF Trace	$\langle q_{\mathrm{MCF}} \rangle$	fBm Trace	$\langle q_{\mathrm{fBm}} \rangle$	$\Delta\langle q \rangle = \langle q_{\mathrm{MCF}} \rangle - \langle q_{\mathrm{fBm}} \rangle$
	UD1	0.0484	FF16–1	0.0353	0.0130
	UD2	0.0484	FF16–2	0.0494	-0.0010
	UD3	0.0363	FF16–3	0.0316	0.0047
	UD4	0.0824	FF16–4	0.0628	0.0195
	UD5	0.0646	FF16–5	0.0474	0.0172
	UD6	0.1610	FF16–6	0.2383	-0.0773
Averages:		0.0735		0.0775	−**0.0040**

TABLE 4.1. Collecting and averaging the q values found based on the three fractal analyses.

Finally, divide all the data points by the value m such that the fit line runs from $(x, y) = (0, -0.5)$ to $(1, 0.5)$ with unity slope.

Having transformed the scale plots as described, we then subtract the fit line from the transformed data points and calculate the standard deviation q of these residuals; the average of the standard deviations of the three scale plots for a given trace is then calculated. The results of these analyses are listed in Table 4.1. (The naming convention for the Fourier filtered fBm traces is as follows: the first number following “FF” indicates the minimum fluctuation period specified by the FF routine, and the second indexes the traces.)

By subtracting the q value for a given fBm trace from the q value for its corresponding MCF trace, we arrive at a metric for evaluating the extent to which the MCF’s scaling properties resemble those of a true fractal. That is, given that a trace’s q value represents the extent to which its scaling plots are nonlinear within the expected scaling range, if an MCF's q value significantly exceeds that of its corresponding smoothed fBm trace, we may conclude that the MCF is in a sense "less fractal" than the fBm. If, on the other hand, an MCF and its corresponding fBm trace exhibit similar q values, we may take that as evidence of the MCF's fractality, given that it responds similarly to our fractal analyses as a trace which was generated as a pure fractal and processed in analogy to the physical constraints present in our experimental systems. In short, we interpret a greater Δq value to correspond to an MCF that is less fractal.

Of all the numbers listed in Table 4.1, the two highlighted in boldface may be interpreted as summarizing the results. Specifically, given that the UD-MCF and their corresponding fBm traces exhibit a lower overall average Δq value than the MD-MCF do, one may at first be led to conclude that the UD-MCF are more fractal than the MD-MCF. Note, however, that this interpretation relies on the notion that negative $\Delta\langle q\rangle$ values are meaningful and may contribute to this average. An alternate interpretation is as follows: Given that the fBm traces are the 'true' fractal structures against which we are comparing the fBm, we should be interested only in the absolute value $\Delta_2\langle q\rangle = |\langle q_{\mathrm{MCF}}\rangle - \langle q_{\mathrm{fBm}}\rangle|$, such that all negative entries in Table 4.2 become positive. Under this interpretation, the $\langle\Delta_2\langle q\rangle\rangle$ values for the MD-MCF and UD-MCF become 0.0115 and 0.0221, respectively, with the implication that the MD-MCF are marginally more fractal. Under each interpretation, however, the standard deviations of the values from which each average $\langle\Delta\langle q\rangle\rangle$ is calculated are comparable to or larger than the differences between the $\Delta\langle q\rangle$ values for the MD-MCF and UD-MCF, suggesting that no clear trend may be identified.

We may also investigate the $\Delta\langle q\rangle$ values that result from averaging over all six traces in each family for each analysis technique, displayed in Table 4.2. We thus

Trace Group	$\langle \Delta q \rangle$ (AFA)	$\langle \Delta q \rangle$ (Dubuc)	$\langle \Delta q \rangle$ (Variance)
MD-MCF / FF8	0.0105	-0.0002	-0.0071
UD-MCF / FF16	0.0048	0.0022	-0.0189

TABLE 4.2. Average values for Δq found by averaging across all traces in each trace group, listed by fractal analysis technique.

see that the variance method analyses are largely responsible for the instances of negative values for $\Delta\langle q \rangle$ shown in Table 4.1. If we repeat the analysis presented in Table 4.1 but disregard all q values resulting from variance analyses, we arrive at values of $\langle \Delta\langle q \rangle \rangle$ of 0.0051 and 0.0035 for the MD-MCF / FF8 and UD-MCF / FF16 trace families, respectively. Repeating this analysis under the interpretation that the $\Delta\langle q \rangle$ values should be nonnegative yields values of $\langle \Delta_2\langle q \rangle \rangle$ of 0.0074 and 0.0054 for the MD-MCF / FF8 and UD-MCF / FF16 trace families, respectively. These results again support the prior conclusion that the neither family of MCF traces may be considered to be more fractal than the other.

Overall, these results may be seen as confirming Ketzmerick's claim [14] that the addition of small-angle scatterers has no effect on the phase space within electron billiards. Additionally, this investigation demonstrates the difficulty in evaluating the fractal character of traces limited in length, in spectral content, or (especially) both. Under various interpretations of the data, fractal analysis of the UD-MCF and MD-MCF trace sets may suggest that either the MD-MCF or UD-MCF exhibit more pronounced fractal behavior, though the differences between the magnitudes of these quantitative metrics are comparable to the uncertainties in each. In short, these conflicting results may be understood as representative of the limitations of fractal analysis applied to limited data sets, such that no clear distinction may be drawn between the relative fractality of MCF taken from induced and modulation-doped electron billiard devices. This limitation could in principle be alleviated by increasing the length of the MCF traces relative to their minimum feature size. Given that the length of the trace is limited by the cyclotron radius of electron orbits with the electron billiard, this may in principle be accomplished by employing smaller billiard devices or by increasing the phase coherence length of electrons within the billiard. However, as the size of the billiard device is decreased toward the Fermi wavelength of the electrons, one risks departing the semiclassical regime of electron transport which is crucial for MCF studies.

The normalized scaling plots for all the traces analyzed and for all the analysis techniques utilized are displayed in the Appendix.

CHAPTER V

THERMAL STABILITY OF ELECTRON CONDUCTION

5.1. Description of Experiment

The results of Chapter IV demonstrate that the presence of small-angle scattering sites in the AlGaAs/GaAs heterostructure does not significantly alter the phase space of electrons within an electron billiard, based on a fractal analysis of MCF traces. Although the small-angle scattering sites introduced by the modulation-doping technique are not seen to affect the chaotic properties of electron trajectories in a measurable way, we may still investigate the sensitivity of the precise distribution of these trajectories, and hence of the specific features of the MCF traces, to the precise form of the potential landscape induced by remote ionized donors.

Claims of true ballistic electron transport in electron billiard devices imply that the distribution of electron trajectories in the billiards are insensitive to the precise form of this potential landscape. Indeed, the small-angle scattering introduced by the remote ionized donors is traditionally considered to be negligible with respect to the trajectories of electrons within electron billiard devices [6–9, 13, 44]. To test these claims, we seek to investigate the effect on MCF traces of a reorganization of ionized dopants in modulation-doped heterostructures by means of thermal excitation. Our experimental evidence suggests that in fact, conductance through electron billiard devices is highly sensitive to the precise form of the slowly-varying potential landscape introduced by these donors.

It has been shown [7] that features of an MCF trace measured on an electron billiard device may be attributed to the billiard geometry—indeed, claims of true ballistic electron transport in electron billiards imply that device geometry alone is responsible for the details of an MCF trace. Under this reasoning, an MCF trace taken at a given temperature would be altered only by actions that serve to reconfigure the device geometry. However, we find that when a modulation-doped electron billiard device with a constant geometry is brought to a temperature in excess of ∼150 K between MCF measurements at a base temperature of 240 mK, the MCF are significantly altered, indicating that the electron trajectories within the billiard have been redistributed. We attribute this reconfiguration of electron trajectories to a redistribution of the charge states of the remote ionized donors whose collective electrostatic potential influences electron propagation through small-angle scattering events.

To demonstrate that the thermal instability of electron interference as measured by MCF is generic to the modulation doped heterostructure architecture and not unique to a specific heterostructure system, these experiments were performed on electron billiard devices in both the $Al_{0.33}Ga_{0.67}As/GaAs$ and $In_{0.75}Ga_{0.25}As/InP$ material systems.

The MCF measurements on the InGaAs/InP material system discussed in this chapter were performed by Dr. Billy Scannell, and the MCF measurements on the undoped AlGaAs/GaAs material system were performed by Dr. Andrew See. The MCF measurements on the modulation-doped AlGaAs/GaAs material system were performed by myself with the assistance of Rick Montgomery and in collaboration with Dr. Billy Scannell. The 2DEG electron density and mobility measurements on the InGaAs/InP material system described in Section 5.8 were performed by myself.

In the experimental procedure that follows, all MCF traces were measured at a base temperature of 240 mK and recorded with a resolution of 0.5 mK over a range $|B| > B_{\text{cyc}}$; correlation analyses of the MCF traces are performed only over the field range $|B| < B_{\text{cyc}}$. Recall from Section 2.8 that the cyclotron fields for the AlGaAs/GaAs and InGaAs/InP billiards are 160 mT and 280 mT, respectively. All MCF measurements on the AlGaAs/GaAs and InGaAs/InP billiards were performed with six transverse modes in the QPCs. Figures 5.1 and 5.2 display the robust reproducibility of the MCF traces when the billiard is held at base temperature.

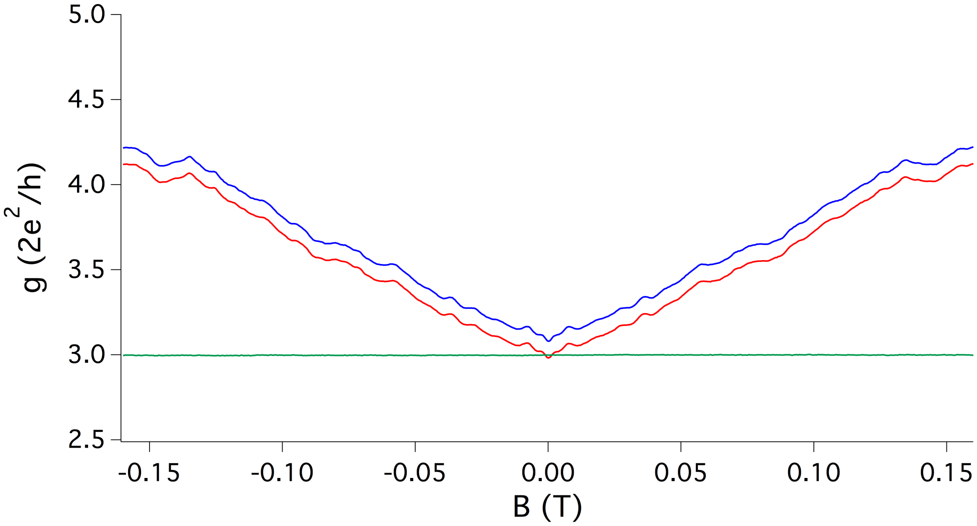

FIGURE 5.1. MCF traces recorded on the AlGaAs/GaAs electron billiard back-to-back while the billiard is held at $T = 240$ mK. The blue trace was recorded following the red trace, and is offset vertically by $0.1 \times 2e^2/h$ for clarity. The green trace represents the pointwise difference between the two MCF traces, and is vertically offset by $3 \times 2e^2/h$. The MCF traces are measured with a resolution of 0.5 mK. MCF measurements performed by myself in collaboration with Dr. Billy Scannell.

Following the MCF measurement, the device is then warmed to a temperature T_i, which is held for 30 minutes before returning the sample to 240 mK and repeating the MCF measurement. We find that the precise form of the MCF measured after the thermal cycle relative to that measured before the thermal cycle is highly dependent on the temperature T_i; see Figs. 5.3 and 5.4.

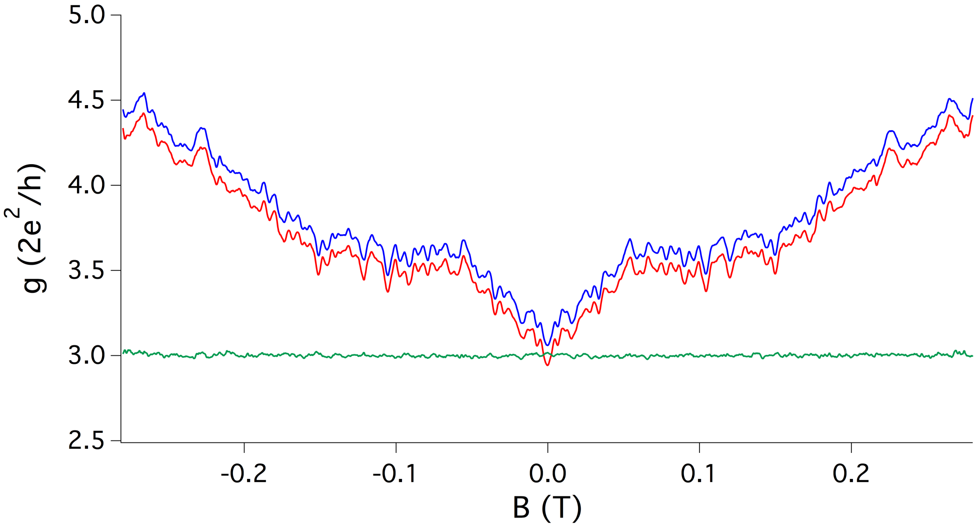

FIGURE 5.2. MCF traces recorded on the InGaAs/InP electron billiard back-to-back while the billiard is held at $T = 240$ mK. The blue trace was recorded following the red trace, and is offset vertically by $0.1 \times 2e^2/h$ for clarity. The green trace represents the pointwise difference between the two MCF traces, and is vertically offset by $3 \times 2e^2/h$. The MCF traces are measured with a resolution of 0.5 mK. MCF measurements performed by Dr. Billy Scannell.

By inspection of Figs. 5.3 and 5.4, it is clear that pairs of MCF taken on either side of a thermal cycle to $T_i = 115$ K are nearly indistinguishable, while a thermal cycle to room temperature significantly alters the fine-scale structure of the measured MCF. This result is suggestive of a thermally activated mechanism which serves to reconfigure the distribution of electronic trajectories within the billiard, and hence the details of the measured MCF, characterized by a threshold temperature between 115 K and 300 K. To probe the nature of this thermal activation mechanism, we measured pairs of MCF separated by thermal cycles to temperatures T_i and quantified the similarity between the two MCF as a function of T_i. To quantify the correlation between two MCF traces $g_1(B)$ and $g_2(B)$, we introduce the correlation function

$$F = \sqrt{1 - \frac{\langle [g_1(B) - g_2(B)]^2 \rangle_B}{N}}, \qquad \text{(Equation 5.1)}$$

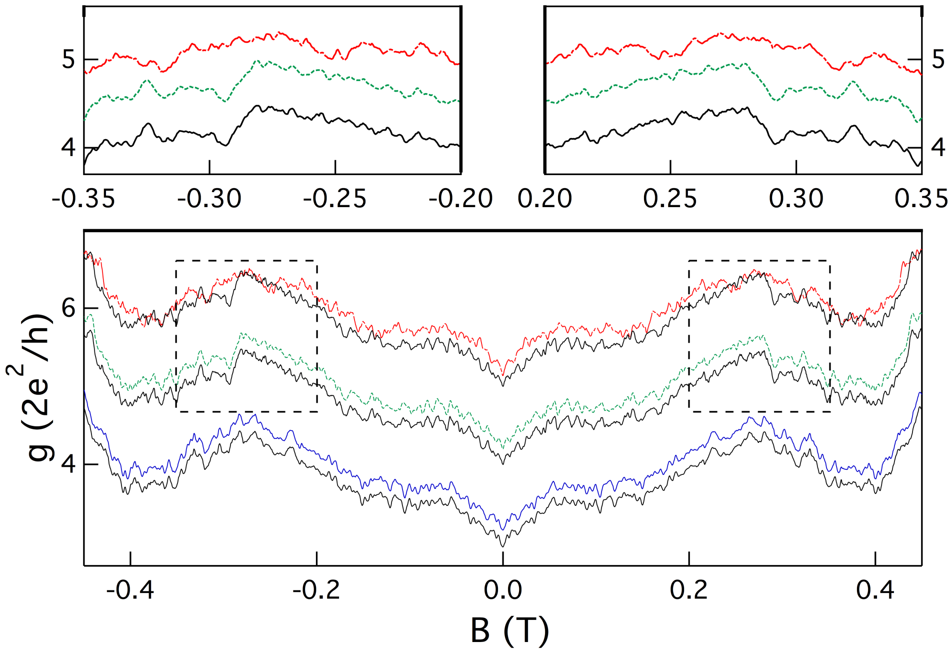

FIGURE 5.3. Comparison of MCF from the InGaAs/InP billiard measured at $T =$ 240 mK after being warmed to three intermediate temperatures T_i. Top to bottom, the T_i values of the pairs of traces are 300 K, 115 K, and 240 mK. The traces are vertically offset for clarity. Top: Magnified comparison of traces taken with $T_i = 115$ K (lower [black] and middle [green]) and $T_i = 300$ K (lower [black] and upper [red]). The MCF traces are measured with a resolution of 0.5 mK. MCF measurements performed by Dr. Billy Scannell.

where

$$N = \langle [g_x(B) - g_y(B)]^2 \rangle_B. \qquad \text{(Equation 5.2)}$$

The average $\langle\rangle_B$ represents an average over all MCF data points in the range $|B| \leq B_C$. The traces $g_x(B)$ and $g_y(B)$ represent a pair of traces that are thought to be "completely" decorrelated, such that the normalization constant N is taken to be the average of the mean-squared differences between several such pairs of traces. In our preliminary analyses, it was assumed that a room temperature thermal cycle was sufficient to completely decorrelate the MCF. In later studies (see below), this assumption was abandoned in favor of a normalization scheme which averaged

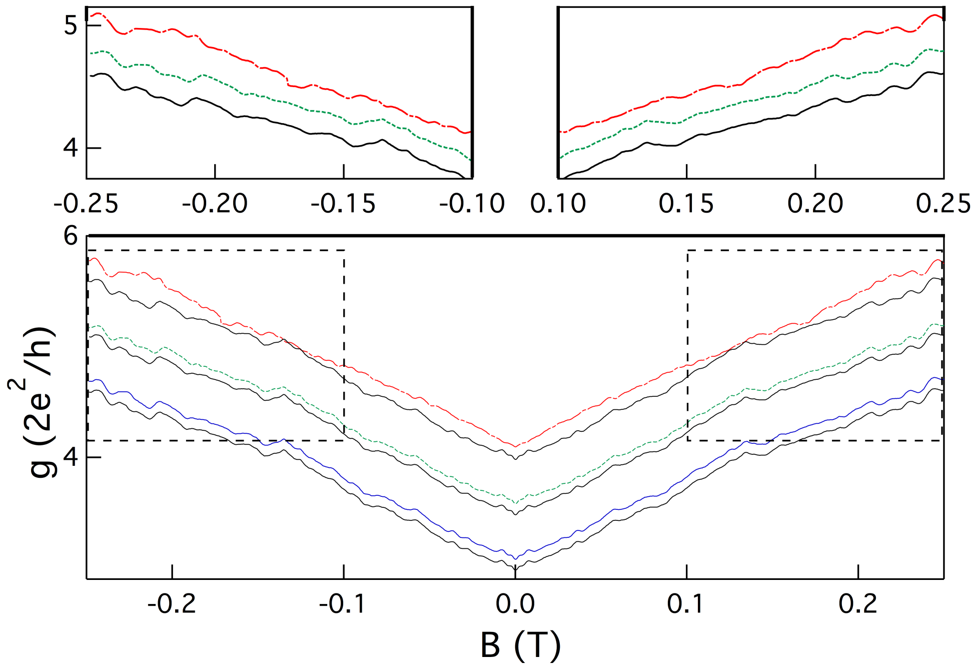

FIGURE 5.4. Comparison of MCF from the AlGaAs/InP billiard measured at $T = 240$ mK after being warmed to three intermediate temperatures T_i. Top to bottom, the T_i values of the pairs of traces are 300 K, 115 K, and 240 mK. The traces are vertically offset for clarity. Top: Magnified comparison of traces taken with $T_i = 115$ K (lower [black] and middle [green]) and $T_i = 300$ K (lower [black] and upper [red]). The MCF traces are measured with a resolution of 0.5 mK. MCF measurements performed by myself in collaboration with Dr. Billy Scannell.

the de-correlation between pairs of computer-generated MCF traces, such that any correlations between the generated traces were purely random. Simply put, the correlation function F provides a measure of the similarity of two traces such that a pair of mathematically identical traces returns a correlation $F = 1$, while a pair of "completely decorrelated" (i.e., randomly related) traces will return $F = 0$.

Having collected the data $F(T_i)$ for each heterostructure system, we may devise a physically-motivated fit function in order to quantify the mechanisms responsible for the MCF decorrelation. Specifically, we attribute MCF decorrelation to the thermally-activated relocation of charge among the silicon donor atoms in the doped layer of the heterostructure, which reconfigures the electrostatic potential landscape through which electrons propagate and hence also the precise distribution of electronic trajectories.

5.2. Preliminary Results

We first modeled the fit function to the correlation measure F as

$$F_{\text{fit}} = \exp(-t/\tau), \qquad \text{(Equation 5.3)}$$

where t is the time spent at an intermediate temperature T_i and $\tau(T_i)$ describes the temperature-dependent characteristic time scale for a decorrelation event to take place. This characteristic time may be described by $1/\tau = P/\tau_0$, where $P(T_i) = \exp(-\beta/k_B T_i)$ represents the probability that a thermally-activated process with activation energy β occurs at a temperature T_i, and where τ_0 represents the characteristic time for the process to occur given infinite thermal energy. Combining these expressions yields a fit function [45]

$$F_{\text{fit}} = \exp\left[-\eta \exp\left(-\frac{\beta}{k_B T_i}\right)\right], \qquad \text{(Equation 5.4)}$$

where $\eta = t/\tau_0$.

Figure 5.5 displays the results of fitting Equation 5.4 to the MCF correlation data from the AlGaAs/GaAs and InGaAs/InP billiards as well as for previously reported measurements taken on a GaAs wire [45, 46]. The insets in Fig. 5.5 display the effect on the fit function of varying the activation energy β and the normalized time constant η: an increase in β has the primary effect of shifting the onset of MCF decorrelation to higher temperatures, while an increase in η has the primary effect of creating a steeper fall-off in F following the onset of decorrelation. The wire was 10 μm long, 50 nm high, and 90 nm wide, and was heavily doped with silicon ($n = 5 \times 10^{24}$ m^{-3}, $E_F = 128$ meV) distributed uniformly through the wire's cross section. These fits return values for the activation energy β of 350 ± 100 meV, 45 ± 20 meV, and 80 ± 20 meV for the AlGaAs/GaAs, InGaAs/InP, and GaAs wire systems, respectively, with respective η values of 3×10^{10}, 45, and 80. These results were published in [2]; before we discuss a physical interpretation of these values, we shall first discuss our later refinements of these analyses.

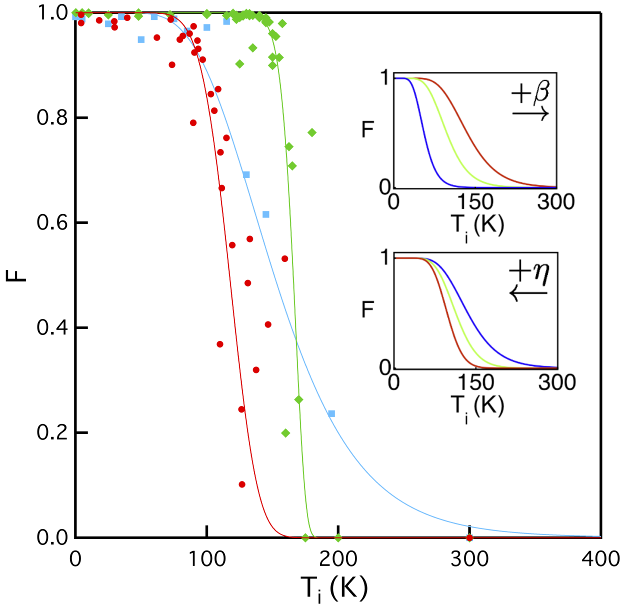

FIGURE 5.5. Fitting the functional form of Equation 5.4 to the MCF correlation data taken on the modulation-doped AlGaAs/GaAs billiard (green diamonds), the modulation-doped InGaAs/InP billiard (blue squares), and a uniformly-doped GaAs wire (red circles). The insets display the response of the fit function to changes in the activation energy β (top) and the normalized time constant η (bottom). From Ref. [2].

5.3. Refinement of Correlation Analysis of AlGaAs/GaAs Billiards

In the time since the publication of Ref. [2], we have performed several refinements to the above analysis. Given the relative wealth of MCF correlation data for the AlGaAs/GaAs material system, the refinements described below primarily pertain to this system; the challenges presented by the InGaAs/InP data, and our refined interpretation of the data at hand, are discussed later.

The first refinement of the above analysis as presented in Ref. [2] pertains to the form of Equation 5.1. Naïvely, we would require a correlation function to do the following: compare the "difference" between two MCF traces to the maximum "difference" we could expect to find; then, flip this normalized decorrelation into a normalized correlation by subtracting from 1. Why, then, did we subtract from 1 prior to evaluating the square root in Equation 5.1? The answer is primarily historical: this was the form of the decorrelation function reported in the original discussion of thermal MCF decorrelation in GaAs wires [46]. Alternately, historical precedent also exists in support of a correlation function in which the square root is evaluated prior to subtraction from unity [9], such that the correlation function becomes

$$F_2 = 1 - \sqrt{\frac{\langle [g_1(B) - g_2(B)]^2 \rangle_B}{N^2}}. \qquad \text{(Equation 5.5)}$$

Although the correlation function represented by Equation 5.1 was chosen for publication in [2], the functional form of Equation 5.5 is more mathematically sensible: Noting that the fraction under the radical sign of Equation 5.1 is a ratio of mean-squared difference, we should evaluate the square root immediately, such that this becomes a ratio of root-mean-square (RMS) difference, which may then be subtracted from unity as in Equation 5.5. Note that Equation 5.5 expresses the normalizing factor as N^2 rather than as N (as was the case in Equation 5.1), such that we may consider the quantity N to be an average of RMS differences for consistency with the numerator.

Another consideration in refining our analysis of MCF correlation data pertains to the fact that measured MCF, especially those taken on the AlGaAs/GaAs system, consistently exhibit a strong linear background trend upon which the conductance fluctuations due to electron interference are superimposed; see Fig. 5.4. This linear trend may be understood as resulting from the depopulation of Landau levels in the electron billiard. In the Landauer-Büttiker formalism, the resistance through an electron billiard supporting N_{QPC} subbands in the QPCs and N_{bill} subbands in the billiard will take the form [21, 47]

$$R = \frac{h}{2e^2}\left[\frac{1}{N_{\mathrm{QPC}}} - \frac{1}{N_{\mathrm{bill}}}\right]. \qquad \text{(Equation 5.6)}$$

At low magnetic fields, N_{QPC} is nearly constant, while N_{bill} decreases linearly with B as the Landau levels are depopulated, such that the conductance through the billiard will increase with magnetic field. Also present in the invariant background trend of the MCF is a structure resulting from the classical focusing of trajectories through the billiard. At certain magnitudes of the applied magnetic field, and hence curvatures of the classical electron trajectories, electrons entering the billiard will be directed through the billiard or reflected to the entrance, corresponding to local maxima and minima in measure conductance, respectively.

Since we expect (and observe) that this background trend is unaffected by thermal cycles, we would like our correlation function to measure the differences in the electron interference fluctuations superimposed upon this background, which are made more visually apparent by removing the background trend. Provided we subtract the same background trend from all MCF, the correlation value describing a given pair of MCF will be unaffected, so this may seem a moot point—but in fact, this procedure of ‘line-subtracting’ the measured MCF is a vital step in employing the next refinement in our analysis procedure, which pertains to the normalization procedure.

Normalizing MCF decorrelation values by the maximum decorrelation value observed in measured MCF assumes that a room-temperature (RT) thermal cycle is sufficient to maximally decorrelate the MCF. In reality, we do not know *a priori* if such an assumption is justified—perhaps even higher temperatures are needed to alter the configuration of small-angle scattering sites to the extent necessary to realize a maximum reconfiguration of electronic trajectories. To test this, we sought to generate mathematically random simulations of MCF using a computer program, such that the pairwise comparisons of these simulated traces may provide a realistic measure of the average correlation between two fully independent traces.

Owing to the well-studied fractal nature of MCF traces (see Chapter IV), our randomly generated simulations of MCF traces were created using the fractional Brownian motion generation algorithm described in Chapter III. Several considerations are necessary, however, before it is possible to compare a generated fBm trace to a measured MCF trace. For instance, we would like to create fBm traces which exhibit similar spectral content to the measured MCF; but because the fractal scaling properties of the MCF do not extend to the resolution limit of the MCF, this entails matching both the measured fractal dimension D_F (or Hurst exponent H) as well as the minimum feature size observed. The minimum size of features observed in MCF taken on the AlGaAs/GaAs system is approximately 4 mT, as determined by a visual inspection and confirmed by a Fourier analysis. (Note that this size scale is a full order of magnitude larger than the MCF resolution limit of 0.5 mT.) Also, a fBm trace will not exhibit a consistent background trend as is seen in the measured MCF traces, as it is intended to model only the conductance fluctuations due to electron interference within the electron billiard. Thus, it is necessary to match fBm traces to MCF traces which have been stripped of any persistent background trends.

To produce and process the fBm traces to be used for MCF correlation normalization, we first selected a set of six MCF traces, each recorded on a separate cooldown from room temperature, to serve as representative of the statistical properties desired in our simulated traces. (The 15 pairwise correlations of these six room-temperature-separated MCF traces provided the value for the normalization constant N as depicted in [2].) We then generated a set of fBm traces whose nominal fractal dimensions (as determined by their seed H value through the relation $D_F = 2 - H$) roughly match the fractal dimensions observed in the MCF (as determined using a variational box-counting method). To impose the desired minimum feature size observed in the MCF, the fBm traces were Fourier filtered by computing a fast Fourier transform (FFT), setting all frequency components higher than the frequency corresponding to this minimum observed size, and returning the trace to real space via an inverse FFT. At this point, the fractal dimensions of the resultant filtered fBm traces were measured, and fBm traces whose measured values of D_F closely matched those of the MCF traces (to within ± 0.01) were selected from the group. That is, since the representative MCF traces exhibit some variation in D_F, each of these six traces was individually matched to a fBm trace with the same statistical properties (viz., minimum feature size and measured D_F). These fBm traces were then vertically rescaled to match the RMS amplitude of its (line-subtracted) partner MCF; see Fig. 5.6 for a visual comparison of the pairs of MCF and fBm.

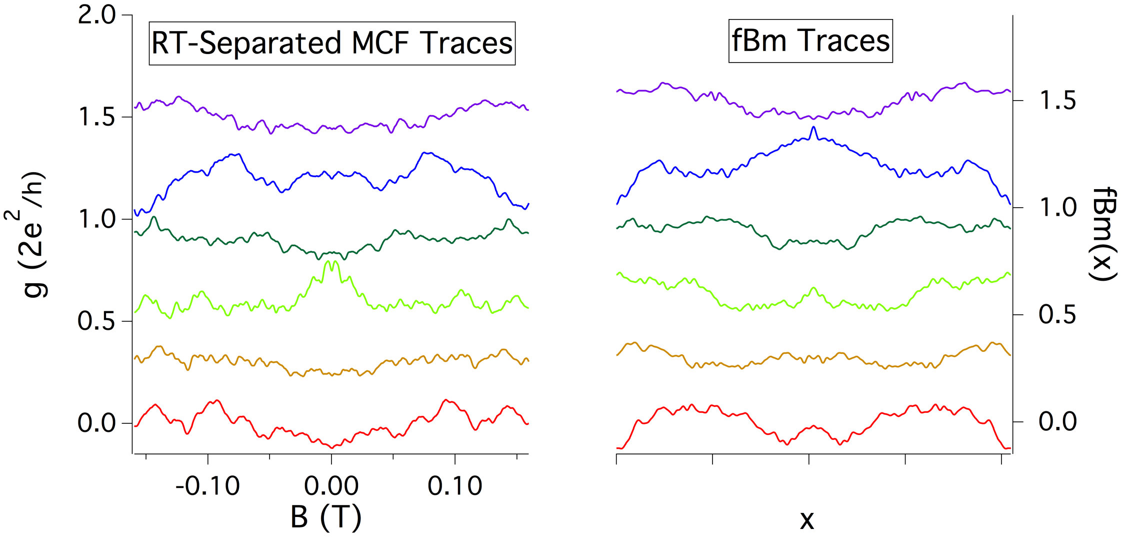

FIGURE 5.6. Left: MCF measured on the AlGaAs/GaAs billiard on six distinct cooldowns from room temperature. Each MCF trace has had a common linear background trend removed. Right: Six fractional Brownian motion traces, processed and selected to share statistical properties with the corresponding (i.e., similarly-colored) MCF. Traces are vertically offset for clarity.

Equipped with a revised correlation function in Equation 5.5 and a more physically meaningful normalization constant N, we may reassess the correlation data for MCF recorded on the AlGaAs/GaAs system. Fig. 5.7 displays the correlation data represented in Fig. 5.5 after reassessing the MCF correlations using Equation 5.5 and a normalization constant N as determined using fBm traces.

Figure 5.7 displays several notable features. First, note that the form of Equation 5.4 has been replaced by the following fit function:

$$F_{\text{fit}} = A \exp\left[-\eta \exp\left(-\frac{\beta}{k_B T_i}\right)\right], \qquad \text{(Equation 5.7)}$$

where the prefactor A is introduced to accommodate those MCF pairs separated by low values of T_i whose measurement noise brings their normalized correlations slightly below unity, such that Equation 5.7 may be used to adequately fit these points. The

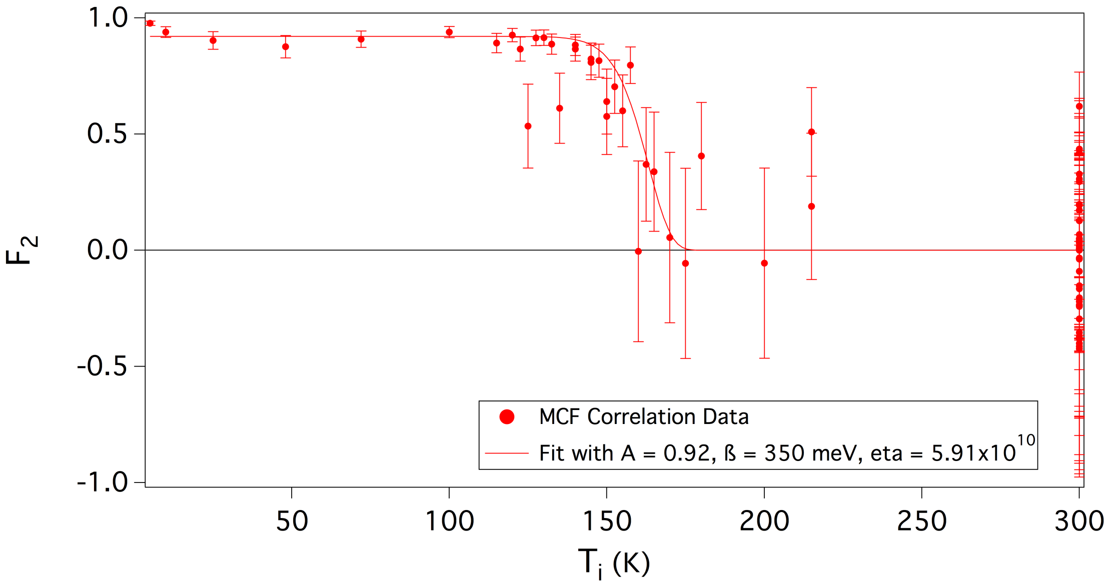

FIGURE 5.7. A plot of F_2 vs T_i for MCF recorded on the AlGaAs/GaAs system (data points) and a fit to the data (red line) based on a slight alteration to Equation 5.4. The displayed η value results from a fit to the data, weighted by their respective error bars, with $\beta = 350$ meV and $A = 0.92$ fixed. Note that all data points plotted at $T_i = 300$ K represent actually MCF data, not simulated traces. See text for discussion error bars and parameter values.

reported value of A was chosen “by eye” to satisfy the requirement that the fit line pass through the error bars for all data with T_i <100 K. Next, note that the fit function of Equation 5.7 remains a compelling fit to the data when the value of β is kept at 350 meV, as reported in [2], suggesting that our reported interpretations of these values remain valid.

The error bars that now appear on the data points reflect our uncertainty in the value of the normalization constant N rather than an uncertainty in the RMS difference between the MCF traces under comparison. In particular, note that Equation 5.7 is of the form $F_2 = 1 - \Delta/N$, where Δ is the RMS difference between two MCF traces separated by a thermal cycle and N is a normalization constant (ideally, the largest possible value of Δ). In practice, we have taken N to be the mean pairwise RMS difference between members of a set of randomly-generated and filtered fBm traces. This collection of RMS differences between the fBm traces taken pairwise also exhibits a nonzero sample standard deviation, δN, such that we may derive the uncertainty in F_2 given the (fixed) magnitude of δN:

$$\begin{aligned} F_2 &= 1 - \frac{\Delta}{N} \\ \frac{\delta F_2}{\delta N} &= \frac{\Delta}{N^2} \\ \delta F_2 &= \left(\frac{\Delta}{N}\right)\left(\frac{\delta N}{N}\right) \\ &= (1 - F_2)\frac{\delta N}{N}. \qquad \text{(Equation 5.8)} \end{aligned}$$

Since the quantity $\delta N/N$ is a constant (for a given set of pairwise correlations from which N was calculated), the quantity δF_2 depends only on the value of F_2 found for a given pair of measured MCF traces, and varies between zero (for $F_2 = 1$) and the full ratio $\delta N/N$ (for $F_2 = 0$).

5.4. Interpreting τ and η

Recall that our MCF correlation data are fit using

$$\begin{aligned} F_{\text{fit}} &= A \exp\left[-\eta \exp\left(-\frac{\beta}{k_B T_i}\right)\right], \\ \eta &= \frac{t}{\tau_0}, \qquad \text{(Equation 5.9)} \end{aligned}$$

where t is the time spent at the intermediate temperature T_i and τ_0 is a characteristic time for charge transfer. Thus, this model accounts for the decorrelation of MCF traces due to holding the electron billiard at T_i for a given length of time (30 minutes), but fails to account for any charge transfer between donor sites that takes place during the finite (and often lengthy) time needed to warm the billiard to T_i and cool it back down to our base temperature. However, since the approximate heating and cooling rates $T(t)$ are known, it is straightforward to generalize the form of Equation 5.7 to account for charge transfer events that take place during heating and cooling cycles (see Appendix). The result is a fit function with three terms, one of which is simply Equation 5.7, and the remaining two being integrals representing the heating and cooling cycles:

$$F_{\text{fit}}(T_i) = A\exp\left[-\frac{1}{\tau_0}\sum_{k=1,2,3}\int_{T_j=0}^{T_i} dT_j\left(\frac{dt}{dT_j}\right)_k \exp\left(-\frac{\beta}{k_BT_j}\right)\right] \tag{Equation 5.10}$$

$$\begin{aligned} &= A\exp\left\{-\frac{1}{\tau_0}\right. \\ &\left[0.0214\int_{T_j=0}^{T_i} dT_jT_j\exp\left(-\frac{\beta}{k_BT_j}\right)\right. \\ &+ t(T)\exp\left(-\frac{\beta}{k_BT_i}\right) \\ &\left.\left.+\ 0.41\int_{T_j=0}^{T_i} dT_j\exp\left(-\frac{\beta}{k_BT_j}\right)\right]\right\}. \end{aligned} \tag{Equation 5.11}$$

Despite the significantly altered form of this revised fit function, it is in fact possible to fit this function to our data with negligible variation from the fit provided by Equation 5.7 using the same value of $\beta = 350$ meV as before and a revised τ_0 value; see Fig. 5.8.

The value of τ_0 needed to obtain this correspondence is roughly twice as large as the value suggested by Equation 5.7 (using $t = 30$ minutes, $\beta = 350$ meV, and η as determined by fitting Equation 5.7 to the data). This is a sensible result, as accounting for the additional time spent at temperatures above the base temperature should return a larger characteristic time scale needed to observe a given degree of

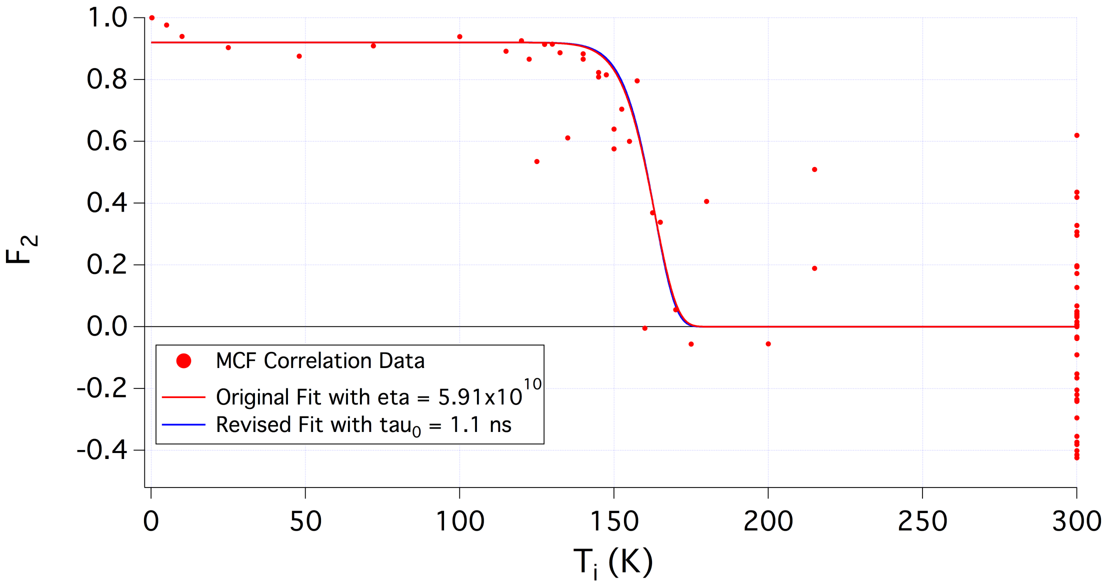

FIGURE 5.8. A plot of F_2 vs T_i for the AlGaAs/GaAs billiards. The red data points and fit line are identical to those shown in Fig. 5.7. The blue fit line represents a fit of the form Equation 5.11 and uses the same value of $\beta = 350$ meV, returning a value of $\tau_0 = 1.1$ ns.

MCF decorrelation. It is also worth noting, however, that the uncertainty in the best-fit value of η is typically at least 25 percent of the total value.

5.5. Refining the Data Set

An examination of Fig. 5.7 suggests that the fit provided by Equation 5.11 would be more compelling if not for the presence of a handful of data points which serve as outliers to the trend. For instance, two data points in the vicinity of $T_i = 130$ K lie conspicuously below the fit line, and at least one point at $T_i = 215$ K is similarly removed from the trend.

As noted above, MCF taken from a given AlGaAs/GaAs billiard are observed to exhibit slightly different fractal dimensions D_F (as determined using a variational box counting method) ranging roughly from $D_F = 1.15 - 1.39$. While the precise nature of this evolution of D_F remains an open question, the existence of this discrepancy offers a means to asses the relative validity of the data points in Fig. 5.7.

Figure 5.9 displays the same data and fit curve as Fig. 5.7, with several key differences. First, the shapes of the data point markers are now reflective of which of the two nominally identical AlGaAs/GaAs billiards provided the data point—circles represent MCF taken on the device labeled “Ca”, and squares represent MCF taken on the device labeled “Cb”. Also, the plot has been edited such that the size of each data point marker is proportional to the difference between the measured D_F values of the two MCF whose normalized RMS difference provides the data point in question. Thus, to the extent that we may expect D_F to change minimally due to a thermal cycle, we may regard the larger data point markers in Fig. 5.9 to represent data that are more likely to be erroneous.

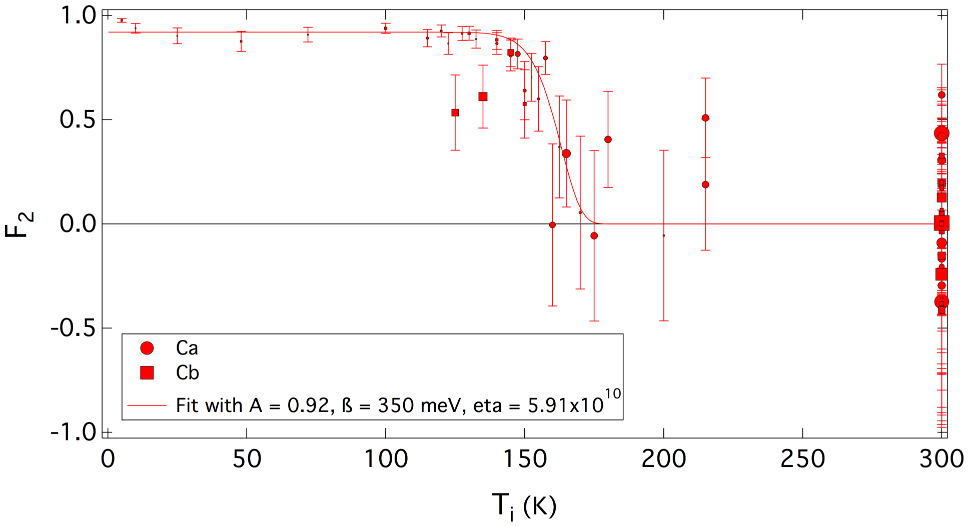

FIGURE 5.9. A plot of F_2 vs T_i for the AlGaAs/GaAs billiards. Here, the size of each data point marker is proportional to the difference between the D_F values for the two MCF represented by the data point. Also, the shapes of the data point markers now illustrate which of the two nominally identical AlGaAs/GaAs billiard devices, Ca and Cb, provided the data point.

The expectation that D_F should remain unchanged after a thermal cycle is well-supported. As discussed in prior publications [25, 35], the fractal dimension of a MCF trace is found to depend on the dimensionless quantity Q, which represents the ratio of the billiard's electron energy level spacing to the thermal energy level broadening:

$$\begin{aligned} Q &= \frac{\Delta E_S}{\Delta E_B} \\ &= \frac{(2\pi\hbar^2)/(m^* A)}{\sqrt{(\hbar/\tau_\phi)^2 + (k_B T)^2}}. \end{aligned} \qquad \text{(Equation 5.12)}$$

In this expression, m^* is the electron effective mass in the billiard, A is the billiard area, and τ_ϕ is the phase coherence time, related to the phase coherence length through $\ell_\phi = v_F \tau_\phi$. Figure 5.10 displays the empirical relationship between the fractal dimension and the Q value for MCF taken on seven different AlGaAs/GaAs electron billiards.

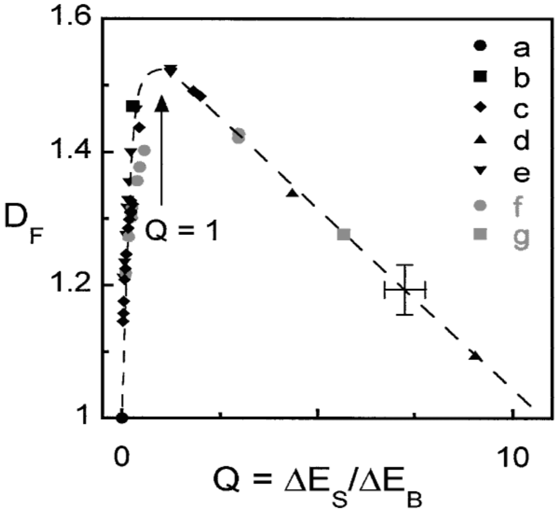

FIGURE 5.10. A plot of fractal dimension D_F vs the quantity Q for seven different billiard devices labeled 'a' through 'g' fabricated in the AlGaAs/GaAs heterostructure. This plot is known as the 'Q Curve'. See Refs. [25, 35] for more information. From Ref. [35].

Of the quantities embedded in the definition of Q, the only value which could be expected to vary between nominally identical measurements of a given billiard is the effective billiard area A. While our experimental procedure made an effort to keep this value constant (through appropriate gate-voltage calibration), it is possible that this was not always the case, and we hypothesize that a slight variation in A is responsible for the observed variation in D_F. Thus, since we seek to isolate the effect of a thermal cycle on the MCF recorded on a billiard with a given geometry, we are justified in excluding from our analysis data points that are suggestive of a variation in device geometry, as indicated by an observed drift in the MCF's fractal dimension.

Excluding data points based on a maximum acceptable drift in observed fractal dimension of 0.05 returns the data shown in Fig. 5.11, which reveals a closer agreement between the data and fit line.

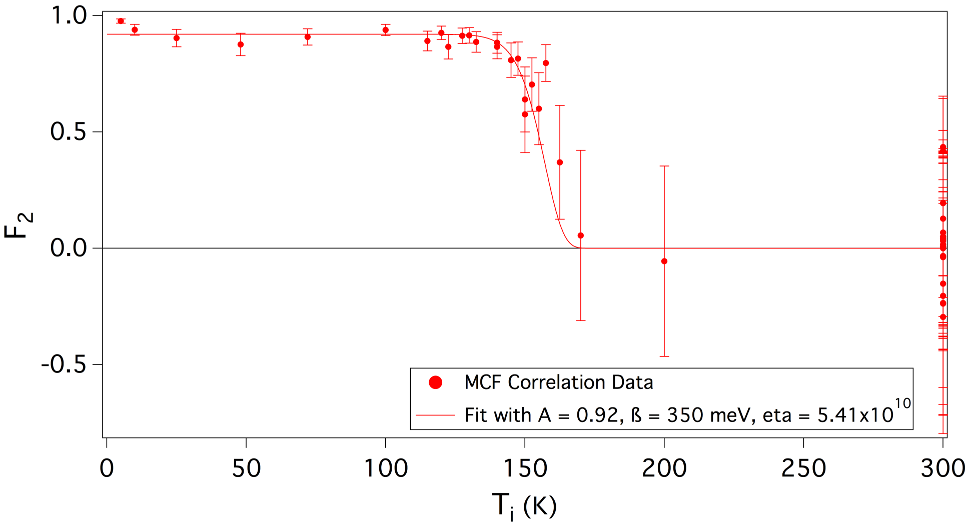

FIGURE 5.11. A plot of F_2 vs T_i for the AlGaAs/GaAs billiards. This figure displays the same data as Fig. 5.9 after omitting those data points (red) which represent MCF pairs in which the fractal dimension D_F is observed to vary by more than 0.05. Fitting this data set with Equation 5.11 (red line) with the value $\beta = 350$ meV yields a slightly lower value of η.

5.6. Adding Data from Induced Billiard Devices

Armed now with a correlation normalization scheme which places no requirements on the behavior of MCF taken on distinct cooldowns from room temperature, we may add to these plots the data representing MCF taken on induced electron billiard devices. Drs. Andrew See and Adam Micolich have demonstrated [18, 27] that MCF obtained on billiards free of ionized dopants are remarkably robust to thermal cycles, even up to room temperature. This result may be seen qualitatively in Fig. 5.12, displayed in Ref. [27], which displays MCF measured on an electron billiard in an undoped AlGaAs/GaAs heterostructure.

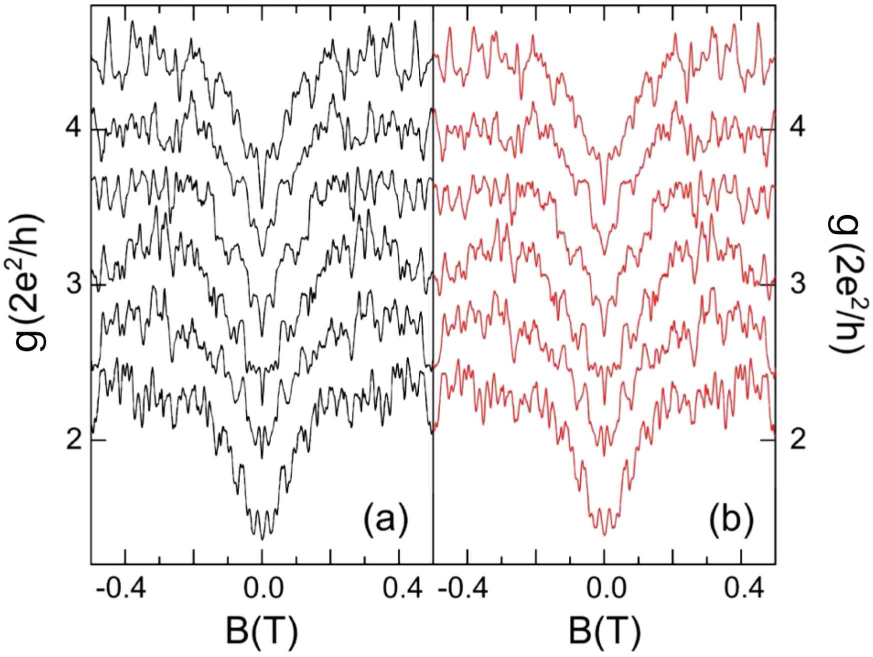

FIGURE 5.12. Comparison of MCF traces taken on an electron billiard device in the undoped $Al_{0.33}Ga_{0.67}As$/GaAs heterostructure (a) before and (b) after a thermal cycle to room temperature. In each panel (a) and (b), the sequence of traces represents MCF taken with top gate voltages ranging in 5 mV increments between +0.93 V (bottom) to +0.955 V (top). Traces are sequentially offset vertically for clarity. From Ref. [27].

Given the analysis presented in [2], which assumed that a room-temperature thermal cycle is sufficient to completely decorrelate the MCF, it would have been impossible to display this thermal insensitivity on Fig. 5.5. While we have demonstrated that a room-temperature thermal cycle is indeed sufficient to completely decorrelate the MCF taken on modulation-doped systems, this is clearly not the case for induced electron billiards, and hence we must rely on randomly-generated fBm traces to provide a normalization constant against which the pairwise differences between MCF traces may be compared.

To generate and modify fBm traces adequate for comparison to MCF taken on induced devices, it is necessary to match the spectral content, depth of fine structure, and RMS amplitude of the MCF. However, this method is only appropriate if we may assume that MCF from induced devices exhibit similar fractal scaling characteristics as MCF from modulation-doped devices. Prior variational method box-counting fractal analysis performed in our group by Dr. Billy Scannell concluded that the MCF from induced devices are not fractal. However, upon revisiting this analysis and comparing scale plots (see Chapter IV), we have found that we cannot conclusively say that MCF from induced devices are any less fractal than those from modulation-doped devices.

Given that MCF from induced devices appear to exhibit similar scaling properties as those taken from modulation-doped devices, we repeated the above method of generating fBm traces, Fourier filtering the traces to obtain the desired minimum feature size, and rescaling vertically to match the RMS amplitudes found in the MCF. Fractional Brownian motion traces were generated to resemble each of the 12 MCF traces displayed in 5.12 representing pairs of MCF taken at each of six unique top-gate voltages before and after room-temperature thermal cycles. These MCF are observed to exhibit fractal dimensions between 1.20 and 1.35, and contained fine-scale features down to a minimum period of 8 mT, well in excess of their resolution limit of 0.4 mT.

Because the measured fractal dimension is seen to vary with the applied top-gate voltage, a batch of fBm traces was generated which exhibited the range in D_F seen at each top-gate voltage. That is, for each top-gate voltage, a number of fBm traces were generated whose fractal dimensions are similar to those of the corresponding MCF. The number of fBm traces simulated for each gate voltage range from four to 16, providing between six and 120 pairwise combinations from which normalization constants may be extracted for each pair of MCF. Although fractal dimension appears to generally increase with the applied top-gate voltage, the average N value obtained for each gate voltage varies little with gate voltage, such that the variation among the N values used for each gate voltage is smaller than the uncertainty (*viz.*, standard deviation) in calculating each value of N.

Also available for analysis are MCF traces taken on the induced device labeled AS57N, which were measured at the University of Oregon in the summer of 2010 by myself in collaboration with Drs. Andrew See and Adam Micolich. These traces include MCF measured on several cooldowns from room temperature at the same six top-gate voltages used in [27]. A new batch of fBm traces was needed to simulate these MCF, since these MCF are found to exhibit a different fractal dimension, minimum feature size, and cyclotron field than those measured on AS61N. In further contrast to the MCF measured on AS61N, those measured on AS57N are found to have fractal dimensions that do not vary systematically with changes in gate voltage, such that a single normalization constant may be applied to the entire data set. Eight fBm traces, with measured D_F between 1.13 and 1.15, were used to calculate this normalization constant.

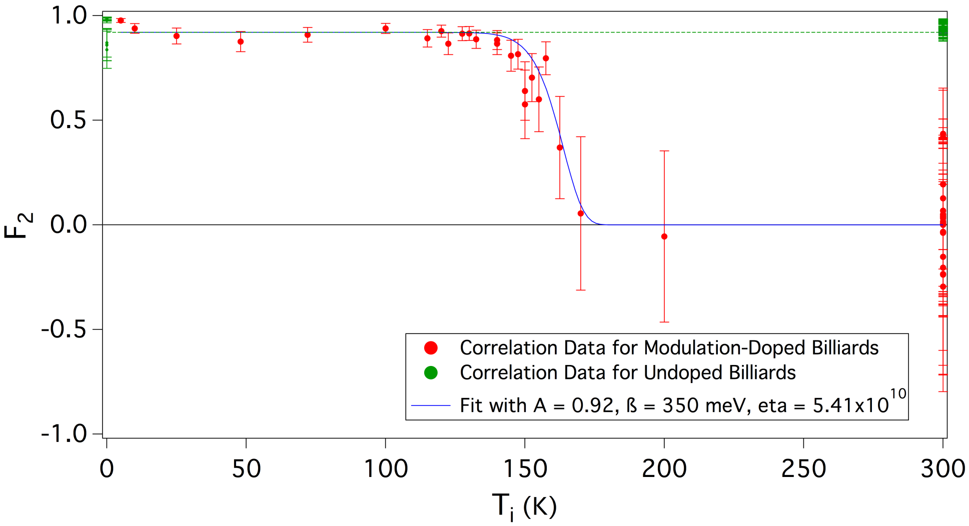

FIGURE 5.13. A plot of F_2 vs T_i for the AlGaAs/GaAs billiards (red), the induced device AS57N (green), and the induced device AS61N (purple). The blue fit line is identical to the fit line displayed in Fig. 5.11. The room-temperature-cycle-separated data taken from AS61N are horizontally offset by -5 K for clarity. The horizontal green dashed line is intended to serve as a guide to the eye to demonstrate that MCF decorrelation due to a room-temperature thermal cycle is on par with the noise level at base temperature.

Normalized correlations from both induced devices are displayed in Fig. 5.13. This plot serves as a quantitative confirmation that billiards formed using induced heterostructure architectures are significantly more thermally stable than their modulation-doped counterparts. Indeed, inspection of Fig. 5.13 indicates that a room temperature thermal cycle does not induce any additional decorrelation of the MCF from induced devices relative to the noise signal differentiating back-to-back measurements at base temperature.

5.7. Interpretation of Fit Parameters

We hypothesize that the observed thermally-activated decorrelation of MCF measured on modulation-doped electron billiard systems results from the fact that the distribution of electron trajectories within the billiard is highly sensitive to small-angle electron scattering events induced by the remote ionized dopants' electrostatic potential. That is, these ionized dopant atoms, though removed from the plane of the 2DEG, collectively create an electrostatic potential landscape in the plane of the 2DEG (see Fig. 5.14), such that an electron's trajectory through the billiard is dependent upon the precise configuration of this potential landscape. We thus expect that the conditions needed to reconfigure the recorded MCF traces will match the conditions needed to rearrange the charge states of the ionized dopants.

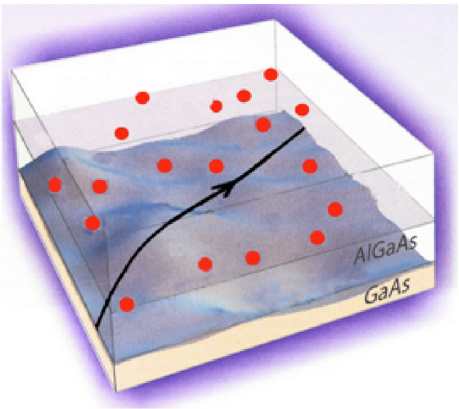

FIGURE 5.14. A schematic of the slowly-varying electrostatic potential landscape (blue) induced in the plane of a 2DEG by ionized dopant atoms (red) located above the plane of the 2DEG. The black line indicates a sample electron trajectory through such a potential landscape. From Ref. [48].

If it were the case that all dopant atoms are ionized at low temperature, we would not expect to see any thermally-activated MCF decorrelation—since the individual dopant atoms are fixed in place in the crystal lattice at all temperatures, the electrostatic potential induced by these ions would then also remain unchanged.

Instead, only a fraction of the dopant atoms are ionized at low temperature—simulations suggest that only 50 percent of donors in the AlGaAs/GaAs system are ionized, and it is similarly likely that not all donors in the InGaAs/InP system are ionized at low temperature[1]—and the form of their collective electrostatic potential depends on precisely which of the atoms are ionized. We now consider the kinetics of such charge transfer events for each material system in turn.

5.7.1. Charge Transfer in the AlGaAs/GaAs Heterostructure

We hypothesize that charge transfer to and from the donor atoms must take place via communication with the 2DEG, given that the doped layer of the heterostructure is not populated with free electrons. At first glance, however, the observed activation energy of 350 meV for MCF-decorrelating charge transfer in the AlGaAs/GaAs heterostructure seems incommensurate with the 220 meV potential barrier separating the 2DEG from the doping plane; see Fig. 5.15.

However, it is well-known that the Si-doped n-Al$_x$Ga$_{1-x}$As alloy supports a deep donor trap state known as the DX center when $x \geq 0.22$ [49, 50]. The DX center is so named as it was originally believed to be formed by a substitutional donor atom (D) together with an unknown lattice defect (X). More recent investigations [50, 51] suggest that the DX center is properly understood as a highly-localized center with negative charge formed when an ionized silicon donor atom DX^+ captures a single electron to reach the unstable state DX^0, which may then capture a second electron with a higher binding energy than the first to reach the negatively-charged DX^- state. Because the DX center traps the second electron more strongly than the first, the center is said to have negative-U properties, in reference to the Hubbard correlation

---

[1] We acknowledge Drs. Alex Hamilton and Theodore Martin for fruitful discussions regarding the ionization rates of donors in the AlGaAs/GaAs and InGaAs/InP systems, respectively.

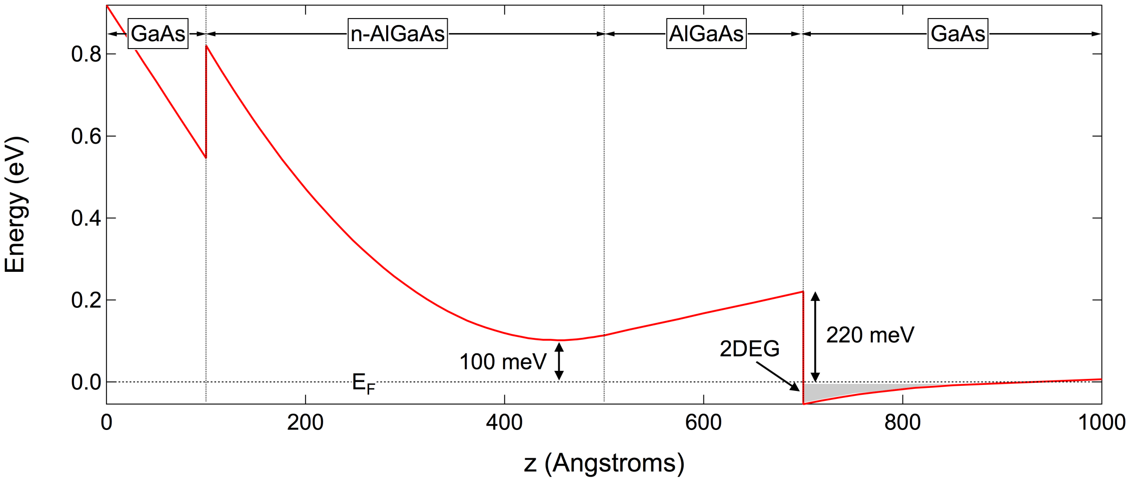

FIGURE 5.15. Conduction band diagram for the AlGaAs/GaAs heterostructure system. The vertical axis measures energy; the horizontal axis measures depth into the heterostructure. The 2DEG (gray) forms at the interface between the spacer AlGaAs layer and the GaAs layer.

energy U. Figure 5.16 presents a configuration coordinate diagram indicating the energy levels characterizing the DX center.

A notable property of the DX center is the observed energy barrier to both electron capture and emission. Deep-level transient spectroscopy (DLTS) studies reveal a thermal activation energy for electron emission from the DX center of 440 meV. Electron capture by the DX center is found to be characterized by a thermally activated capture cross section of the form $\sigma = \sigma_\infty \exp(-E_{\text{cap}}/k_B T)$ with a capture energy (with respect to the conduction band minimum) of $E_{\text{cap}} = 200$ meV [52]. Although the DX center may be photoionized (with a threshold energy of 800 meV), the capture cross section for optically-activated electron capture is zero. Many studies [53–57] of the thermal activation energy for electron capture by the DX center involve persistent photoconductivity (PPC) measurements, in which the DX centers are photoionized, and the temperature-dependent rate at which electrons are recaptured is observed. Such studies report that this decay of PPC follows a

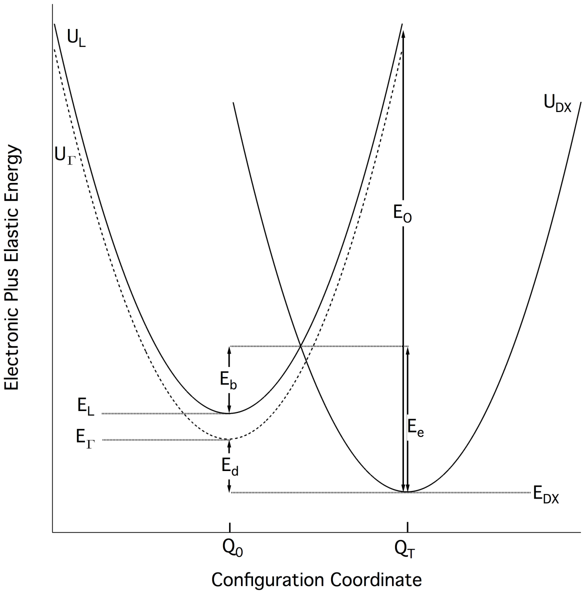

FIGURE 5.16. Configuration coordinate diagram for the DX center in Si-doped n-$\mathrm{Al}_{0.33}\mathrm{Ga}_{0.67}\mathrm{As}$. The parabolas centered at Q_0 and Q_T represent the sum of the electronic and lattice energies for electrons in the conduction band and trapped in the DX center, respectively. The energies E_L and E_Γ represent the L and Γ conduction band minima, respectively. E_d represents the donor binding energy, and E_b represents the DX capture barrier with respect to the L minimum of the conduction band. E_e and E_O represent, respectively, the activation energy for emission of an electron from the DX center and the optical ionization energy. Figure based on diagram provided in Ref. [49].

stretched-exponential decay law of the form

$$n(t) = n_0 \exp\left[-\left(\frac{t}{\tau}\right)^{\alpha}\right], \qquad \text{(Equation 5.13)}$$

where τ represents the characteristic time scale for PPC decay and the stretching exponent[2] $\alpha \leq 1$. Ghosh and Kumar [57] report that the time constant τ is temperature-dependent as $\tau = \tau_0 \exp[\Delta E_B / k_B T]$, such that substituting the value $\alpha = 1$ into Equation 5.13 yields an expression of the same form as Equation 5.3, suggesting a correspondence between the decorrelation fit function and the kinetic of trapping by DX centers. However, fitting our MCF decorrelation data using a stretched-exponential model fails to return a reasonable fit for $\alpha < 1$.

---

[2] Note that the literature typically gives the stretching exponent as β; it is relabeled here as α to avoid confusion with our MCF decorrelation energy β.

The literature offers a variety of interpretations for the stretching parameter α in systems characterized by stretched exponential behavior, including material-dependent factors such as time-dependent barriers to electron capture [58]; a distribution of capture activation energies [52] or of binding energies [53]; as well as more geometrical arguments such as hierarchically constrained dynamics [59] and hopping-transport models [60].

Despite the preponderance of stretched-exponential models describing charge transport among DX centers, there are several factors suggesting that we need not be concerned that the observed MCF decorrelation can instead be described by simple exponential functions. For instance, studies of PPC decay due to recombination with DX centers typically treat systems of bulk Si-doped n-AlGaAs so as to probe these kinetics directly; by contrast, we are concerned with communication of electrons between a 2DEG and an n-AlGaAs layer separated by a potential barrier, and it is reasonable to assume that electron tunneling through this barrier will play an important role in shaping these dynamics. In particular, He *et al.* [55] provide compelling evidence that our observed MCF decorrelation kinetics are closely related to the capture kinetics of DX centers. They derive an effective activation energy and time constant for electron capture by DX centers from the 2DEG as follows: With the capture lifetime for an electron in an n-AlGaAs layer to be trapped by a DX center with capture barrier E_{DX} given by

$$\tau = \tau_0 \exp(E_{DX}/k_B T) \qquad \text{(Equation 5.14)}$$

(with $\tau_0 \sim 10^{-11}$ s), the capture lifetime for an electron in the 2DEG to be captured due to tunneling becomes

$$\tau = [\tau_0 \exp(E_{DX}/k_B T)]/P, \qquad \text{(Equation 5.15)}$$

where P represents the temperature-dependent tunneling probability

$$P = P_0 \exp\left(-\frac{E_t}{k_B T}\right). \qquad \text{(Equation 5.16)}$$

In this expression, $P_0 = 1$ in the high-temperature limit and E_t is an activation energy for tunneling through the barrier. Hence, the tunneling lifetime for an electron to be captured by a DX center from the 2DEG is

$$\tau = \tau_0^* \exp\left[\frac{E_{DX} + E_t}{k_B T}\right], \qquad \text{(Equation 5.17)}$$

where $\tau_0^* = \tau_0/P_0$ and $E_{DX} + E_t = E_c'$ is an effective capture energy. Transient photocurrent (TPC) measurements on an n-$\mathrm{Al_{0.3}Ga_{0.7}As}$/GaAs sample with a 30 nm AlGaAs layer doped to 1×10^{18} cm^{-3} separated from the 2DEG by a 10 nm undoped AlGaAs layer yielded a measurement of $E_c' = 340 \pm 40$ meV and $\tau_0 \sim 10^{-9}$ s [55]. These results are in excellent agreement with our fit values of $\beta = 350 \pm 100$ meV and $\tau_0 \sim 10^{-9}$ s, strongly suggesting that electronic communication between DX centers in the n-AlGaAs layer and the 2DEG in our electron billiards is responsible for the observed decorrelation of MCF traces.

As a quantitative demonstration of the temperature sensitivity of electron transfer between the 2DEG and donor layer in our model, Table 5.1 displays

T (K)	$\tau(T)$
4 K	$\sim 10^{424}$ years
77 K	2.8 million years
150 K	10.5 minutes
300 K	0.8 ms

TABLE 5.1. Values of the thermally-activated characteristic time for electron migration τ at several temperatures. These figures are based on applying the model $\tau = \tau_0 \exp(\beta/k_B T)$ with $\tau_0 = 1.1$ ns and $\beta = 350$ meV, as suggested by our experimental results from MCF taken on AlGaAs/GaAs electron billiards.

the characteristic time for MCF decorrelation $\tau(T) = \tau_0 \exp(\beta/k_B T)$ at several temperatures.

5.8. Charge Transfer and MCF Correlation in the InGaAs/InP Heterostructure

Having demonstrated a correspondence between the temperature-dependent decorrelation of MCF from the AlGaAs/GaAs system and the energetics of deep-level donor sites in that system, we turn our attention to the behavior of charge trapping in the InGaAs/InP system. Unlike the deep-level trap states in AlGaAs, Si donors in InP are understood to be shallow hydrogenic traps with a capture energy of 5.6 meV [61]. This lack of deep-level traps is commensurate with the lower MCF decorrelation activation energy of 45 ± 20 meV in this system as reported in Ref. [2]. For comparison, the InP conduction band edge is roundly 250 meV above the Fermi energy, while the conduction band edge at the δ-doping layer is roughly 75 meV above E_F (see the band diagram reproduced in Fig. 5.17).

Before investigating the relationship between MCF decorrelation and the energetics of the InGaAs/InP heterostructure system, let us first consider the effects of the aforementioned refinements to the MCF analyses pertaining to the AlGaAs/GaAs

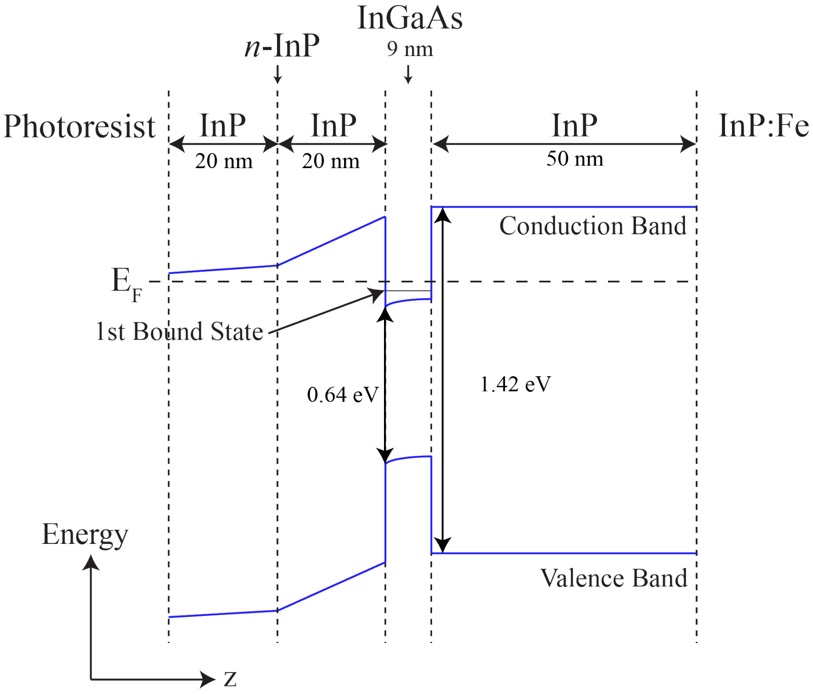
InGaAs
9 nm
n-InP
Photoresist
InP
20 nm
InP
20 nm
InP
50 nm
InP:Fe
Conduction Band
E_F
1st Bound State
0.64 eV
1.42 eV
Energy
Valence Band
z

FIGURE 5.17. Band diagram for the InGaAs/InP heterostructure. The vertical axis represents energy; the horizontal axis represents the distance z in the heterostructure growth direction. (Note: This figure is identical to Fig. 2.11 displayed in Chapter II.)

system as applied to the InGaAs/InP system. First, regarding the recalculation of the normalization constant N against which temperature-dependent MCF correlations are measured: The MCF correlation data under investigation were normalized using pairs of measured MCF separated by room-temperature thermal cycles as opposed to the computer-generated traces used to normalize MCF correlations from the AlGaAs/GaAs devices. We may expect this analytical difference to have a negligible effect on our efforts to fit the data, however, given that the studies of MCF from the AlGaAs/GaAs devices suggest that a room-temperature thermal cycle is indeed sufficient to "completely" decorrelate the MCF in that system, and the InGaAs/InP system is observed to exhibit a lower threshold temperature for the onset of MCF decorrelation.

Given that we may retain the value of N used in our initial analysis of the InGaAs/InP MCF data, it is a straightforward matter to revisit the plot of MCF correlation vs intermediate temperature using the correlation metric F_2 given by Equation 5.5. A comparison of the MCF correlation data provided in Ref. [2] using Equation 5.1 and the same data described by Equation 5.5 is provided in Fig. 5.18.

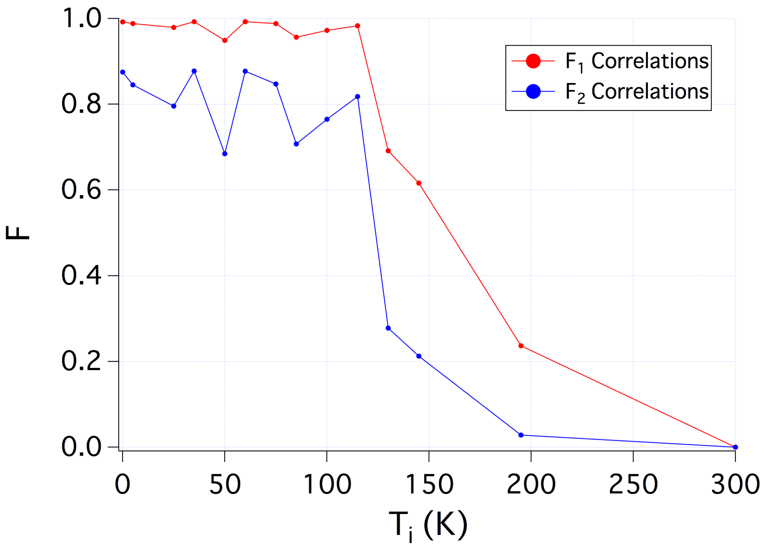

FIGURE 5.18. Comparison of the MCF correlation data for the InGaAs/InP billiards using the correlation functions given by Equation 5.1 (red) and Equation 5.5 (blue). The lines connecting the data points are provided as a guide to the eye.

To fit the correlation data computed using the correlation metric F_2, it is again necessary to adopt the revised fit function Equation 5.4 which includes an overall scaling term A to allow for data points that fall short of $F_2 = 1$ for low T_i. In this case, A is computed by taking the mean of the data points corresponding to $T_i \leq 115$ K. Figure 5.19 displays a comparison of the MCF correlation data using both correlation metrics, and the fit line published in Ref. [2] as well as the same fit line scaled by the factor A.

It is evident from Fig. 5.19 that the previously published fit parameters do a poor job of representing the dynamics that serve to decorrelate the MCF at an

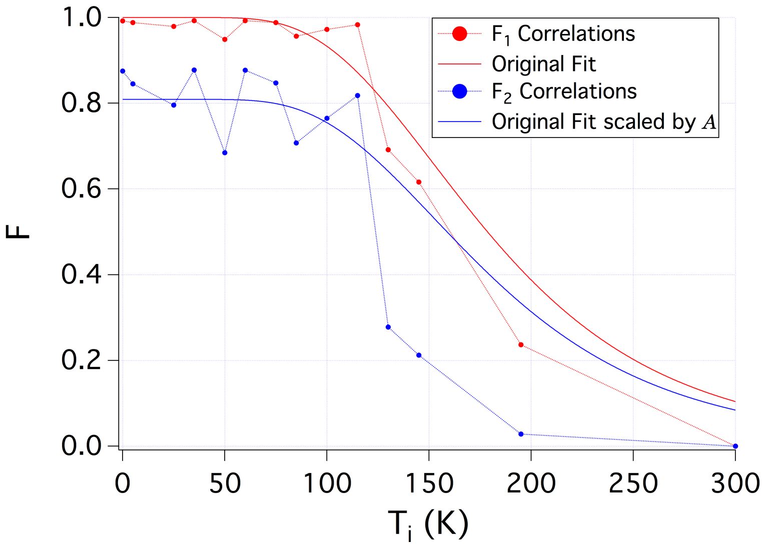

FIGURE 5.19. Comparison of the MCF correlation data for the InGaAs/InP billiards using the correlation functions given by Equation 5.1 (red) and Equation 5.5 (blue), as well as the fits provided by Equation 5.4 (red) and Equation 5.7 (blue) using the parameters $\eta = 12.9$, $\beta = 45$ meV published in Ref. [2], and (for the blue curve) $A = 0.809$. The dotted lines connecting the data points are provided as a guide to the eye.

intermediate temperature of $\sim$ 120 K. That is, we should expect an accurate fit function to effectively model the threshold temperature at which the MCF begin to decorrelate, while the best fit provided by the automated fitting routine falls off well in advance of this temperature. Indeed, the lack of correlation data points in the vicinity of the steep decline in normalized correlation observed near 120 K serves to significantly impede our efforts to fully understand the nature of MCF decorrelation in the InGaAs/InP system. This limitation is due in large part to the excessive cost of performing MCF decorrelation experiments—at the time of this writing, the cost of liquid helium is approximately $14/Liter, and it is not uncommon for a modest experimental run to consume 500 L of liquid helium. In spite of these shortcomings, however, we may use these data—and in particular, the steep decline in normalized

MCF correlation between $T_i = 115$ K and $T_i = 130$ K—to gain several insights regarding the mechanism for MCF decorrelation in the InGaAs/InP billiard.

In order to further probe the relation between MCF decorrelation and electronic communication between the 2DEG in the quantum well and the dopant layer, we employed the following illumination experiment: After cooling to base temperature in the dark, the 2DEG carrier density was measured using low-field Hall effect measurements, and the InGaAs/InP billiard was illuminated using a series of pulses from a red LED until the carrier density saturated. This illumination typically increased the measured 2DEG density from 6.8×10^{11} cm^{-2} to 7.8×10^{11} cm^{-2}. At this point, the billiard was gradually heated (in the dark) and the carrier density was recorded as a function of temperature for temperatures between 240 mK and 190 K (the maximum sustainable temperature in the cryostat). These density data were then normalized as

$$n_{\text{norm}} = \frac{n - n_{\min}}{n_{\max} - n_{\min}}, \qquad \text{(Equation 5.18)}$$

where $n_{\min}$ and $n_{\max}$ are the minimum and maximum density values recorded on a given cooldown from room temperature, respectively. These data are displayed alongside the MCF correlation data (represented using the initial correlation function, Equation 5.1) for this system in Fig. 5.20. The corresponding mobility measurements are provided in Fig. 5.21.

The red line connecting the MCF correlation data in Fig. 5.20 is intended to serve as a guide to the eye. Note that the MCF correlation data presented in 5.20 are plotted using the original version of the correlation function given by Equation 5.1. This is because, rather than attempting to use these correlation data to determine precise values for the parameters β and η for this system, we may instead compare the qualitative form of these data (specifically, the temperature at which the MCF begin

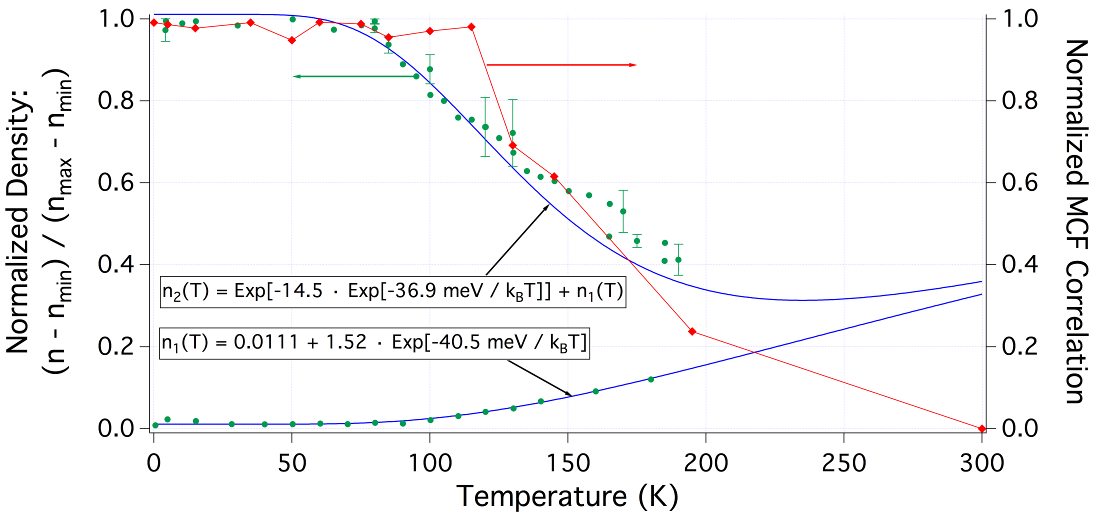

FIGURE 5.20. Green: Normalized 2DEG density (left axis) vs billiard temperature before and after illumination. Red: MCF correlation data (right axis) vs intermediate temperature for the InGaAs/InP billiard. The MCF correlation function used was that given in Equation 5.1, as published in Ref. [2]. See text for explanation.

to decorrelate) to the decay of PPC observed on the same system. This comparison is more easily made when the correlation data are presented in such a way that low values of T_i return near-unity correlation values.

The lower green curve in Fig. 5.20, labeled $n_1(T)$, represents the temperature-dependent 2DEG density in the dark and is well characterized by an activation energy of 40.5 meV. This trend is readily understood as the temperature-dependent occupation of the 2DEG based on the Fermi energy; using $E_F = 40.5$ meV yields an effective electron mass in the InGaAs layer of $m^* = 0.040m_e$, which closely matches the value of $m^* = 0.038m_e$ reported elsewhere [62]. The upper green curve, labeled $n_2(T)$, represents a fit of the post-illumination 2DEG density data using the fit function Equation 5.4; the temperature-dependent occupation of the 2DEG is accounted for by simply adding the trend $n_1(T)$ to this fit. As is the case for persistent photoconductivity studies of the AlGaAs/GaAs system, the decay of PPC in the InGaAs/InP system has been described [63] using a stretched-exponential

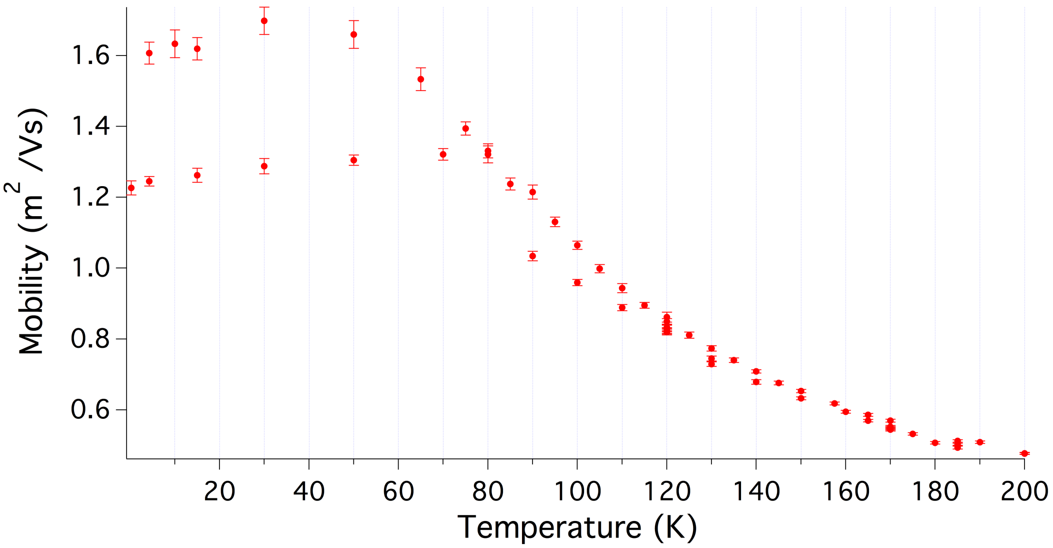

FIGURE 5.21. Mobility as a function of temperature for the InGaAs/InP billiard device. The order in which the measurements were taken is clockwise from the lower right. Note that the low-temperature mobilities reported in this figure are significantly lower than the value of 3.3×10^5 cm^2/Vs reported in Chapter II. Each of these figures represents a mobility measurement made on the same electron billiard device on separate cooldowns from room temperature; the source of this discrepancy is not fully understood, but is likely related to an artifact of the ohmic contacts. Nonetheless, these data reveal a systematic trend with temperature before and after illumination, and are included here for completeness.

model with a stretching exponent of $\alpha \sim 0.4$. Such a model is similarly effective in describing the PPC decay shown in Fig. 5.20, as displayed in 5.22.

The fit line displayed in Fig. 5.22 was performed by eye using the value $\alpha = 0.4$ suggested by Ref. [63] and an activation energy $\beta = 75$ meV that matches the potential barrier at the InGaAs/InP heterojunction; these parameters led to a value of $t/\tau_0 = 180$. Also note that the fit line intentionally meets the error bars displayed nearer to their lowest points: These error bars result from the fact that when the billiard was held at a temperature greater than that necessary to induce PPC decay (roughly 80 K), the 2DEG density was observed to decrease on subsequent measurements at the same temperature over the course of several hours. See Fig.

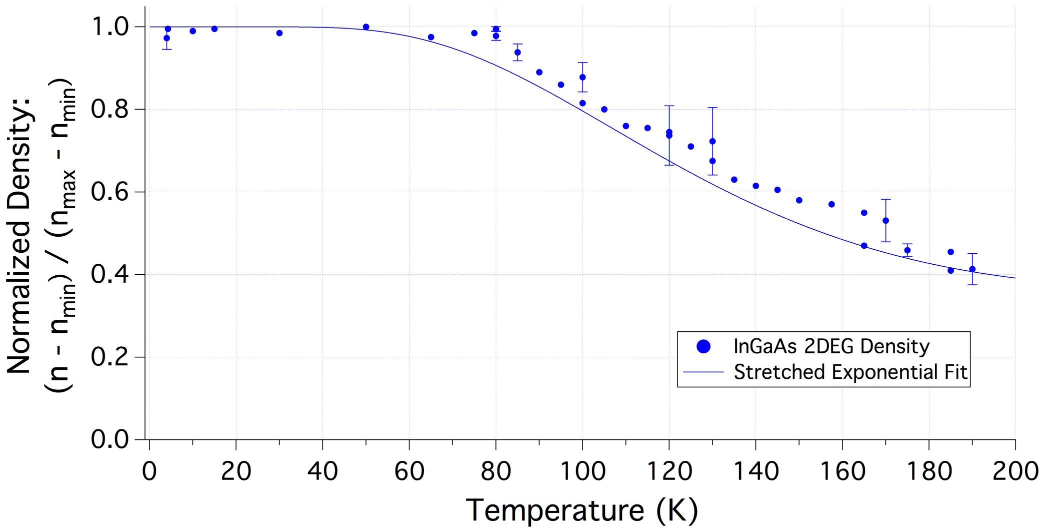

FIGURE 5.22. Normalized 2DEG density vs billiard temperature after illumination. The fit to the data represents a stretched exponential function of the form of Equation 5.13, using $\alpha = 0.4$ (after Ref. [63]), $t/\tau_0 = 180$, and an activation energy $\beta = 75$ meV. Note that this fit was performed by eye and is intended to demonstrate the plausibility of a stretched-exponential PPC decay characterized by a previously-reported stretching exponent and an activation energy commensurate with the heterojunction barrier height. See text for a discussion of error bars.

5.23 for an example of this constant-temperature density decay as a function of time. Owing to the time constraints imposed by the operating costs of this experiment, most data points represent the density measured immediately upon reaching the temperature in question and not the final density that would be reached at that temperature. The error bars are placed on those data points taken at temperatures at which several density measurements were made; the tops and bottoms of these error bars correspond to the initial and final densities recorded, respectively.

The intent of the PPC experiment was to fully ionize all Si donor atoms, such that the increase in 2DEG density would be due to this ionization; by tracking the decay of this PPC as the device was gradually heated, it was hoped that the activation energy β and/or characteristic time scale τ_0 for the observed decline in 2DEG density

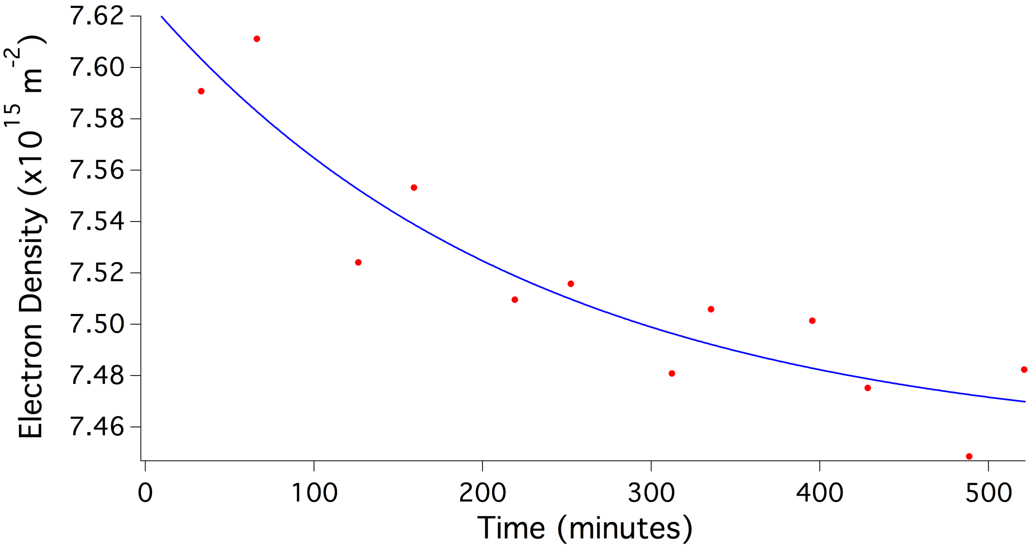

FIGURE 5.23. Post-illumination 2DEG density (red) as a function of time at a constant temperature of T = 120 K. The blue fit curve represents an exponential decay: $n(t,T) = n_0(T) + n_1(T)\exp(-(t - t_0)/\tau_0)$ with $n_0(120\text{ K}) = 7.45 \times 10^{15}\text{ m}^{-2}$, $n_1(120\text{ K}) = 1.51 \times 10^{14}\text{ m}^{-2}$, $t_0(120\text{ K}) = 33.2$ minutes, and $\tau_0 = 227$ minutes.

would correspond to those for the mechanism that induces MCF decorrelation. If such a correspondence could be identified, then the observed delay between the decay of PPC and the decorrelation of MCF as temperature is increased could serve as evidence that a certain threshold of charge relocation in the doped layer is necessary to induce sufficient change in the potential profile in the 2DEG to decorrelate the MCF. Such a study would grant us a means to compare our results to the prediction [64] that the motion of a single strong scattering site is sufficient to completely decorrelate the MCF, as it remains to be determined how much charge rearrangement in the donor layer is necessary to correspond to the motion of a ‘strong scattering site’ in the 2DEG.

In actuality, the illumination source used in this experiment was a red LED, with a (room-temperature) photon energy of roughly 1.9 eV, significantly in excess of the band gaps of both materials in this heterostructure. Furthermore, given the shallow nature of the Si donor trap states, it is reasonable to expect the vast majority of these donors to be ionized even at liquid helium temperatures [65], such that it is very unlikely that the 2DEG density increase of roughly 15 percent may be attributed solely to the full ionization of Si donors.

Although the phenomenon of persistent photoconductivity in the InGaAs/InP heterostructure is well studied [63, 66, 67], the precise nature of the phenomenon we observe here is unclear. The onset of PPC is often attributed to the excitation of electrons across the band gap of either the InGaAs or the InP layers, such that the heterostructure's built-in potential spatially separates the electrons in the conduction band from the holes in the valence band. Such an explanation necessitates a band structure wherein the 2DEG resides at a minimum in the conduction band that is spatially separated from a maximum in the valence band at which holes are trapped. In the case of the heterojunction system described by Wei *et al.* [66], which lacks a quantum well layer, this is simply accomplished because the conduction and valence bands are nowhere flat in the vicinity of the 2DEG. Kane *et al.* [67] discuss a PPC effect in InGaAs/InP quantum well systems, in which electrons excited across the band gap in the InGaAs layer cannot be spatially separated from the remaining holes, as is the case in our devices. Kane *et al.* cite this fact, along with the wavelength-dependent nature of the PPC, as evidence that electron-hole pair production and separation in the InP layer is responsible for the observed effect. However, given that we expect the bands in the InP buffer layer in our system to be relatively flat (see Fig. 2.11), it is unclear whether this mechanism may account for the effect observed in our devices.

Indeed, it is reasonable to expect that our InGaAs/InP heterostructure system supports a variety of trap states which are to date poorly understood. Specifically, we may expect such trap states to exist at the interfacial planes of the heterostructure: at the interface of the InP cap and the photoresist, in the δ-doping layer, and at the interface between the InP spacer layer and the quantum well. The potential profile in the plane of the 2DEG may be expected to be influenced by the charge distribution in any of these interfaces; however, it is difficult to probe the nature of each layer individually. It is nonetheless reasonable to expect that charge relocation in those layers nearer to the InGaAs quantum well will have a greater impact on this potential profile and thus on the MCF measured on the billiard. We may thus seek to interpret the trends witnessed in Fig. 5.20—namely, the onset of PPC decay at a lower temperature than that needed to decorrelate the MCF—as evidence that this excess charge is preferentially migrating to interfaces farther from the 2DEG. We thus hypothesize that electron migration to the more remote surface states exhibits a lower activation energy and affects small-angle scattering sites, while electron migration to interface states nearer to the 2DEG requires a greater activation energy and results in a redistribution of large-angle scatterers. A proposed experiment to help elucidate the nature of these trap states, developed in collaboration with Dr. Theodore Martin, is described in Chapter VI.

CHAPTER VI

CONCLUSIONS

The development of epitaxial semiconductor fabrication techniques, especially paired with conduction band engineering employing the modulation doping technique, has allowed for the development of electronic devices exhibiting remarkable electron mobility. Electron billiard devices fabricated in such heterostructures provide a novel test bed for semiclassical phenomena in the ballistic regime of electron transport. Claims of true ballistic electron transport, however, rely on the assumption that the slowly varying potential landscape at the plane of the 2DEG that results from remote ionized donors in the modulation doping technique are negligible with respect to conduction dynamics through such billiard devices.

In this dissertation, we sought to test two hypotheses regarding the role of remote ionized donors in shaping electron dynamics in billiard devices: first, that the presence of a slowly-varying potential may affect the general phase space in a soft-walled electron billiard in a manner detectible by a fractal analysis of MCF; and second, that the individual features present in MCF traces are sensitive to the precise form of this potential landscape.

To summarize our findings, Chapter IV has demonstrated that the existence of small-angle scattering sites in electron billiards employing the modulation-doped architecture do not measurably alter the electron phase space within the billiards as revealed by a fractal analysis. We have shown that MCF traces from modulation-doped electron billiards are not significantly more fractal than MCF traces measured on undoped electron billiards, which exhibit a similar soft-walled confinement potential but lack the ionized donors of the modulation-doped heterostructure. These results may be seen as providing an experimental verification of the prediction of Ref. [14] that soft-walled billiards generally exhibit fractal MCF, regardless of the presence of a slowly-varying potential in the billiard. It remains an open question, however, whether this slowly-varying potential landscape may be sufficient to yield a mixed phase space in an otherwise stable system. Future work directed toward rigorously modeling the phase space of a hard-walled square electron billiard both with and without ionized donors would be of great value in addressing this question.

In Chapter V, we demonstrated that the small-angle scattering sites produced by the modulation doping technique cannot be neglected in asserting claims of true ballistic electron transport. Through an investigation of the thermal stability of MCF measurements, we have confirmed our hypothesis that the precise distribution of electron trajectories through a modulation-doped billiard is highly sensitive to the configuration of the remote ionized donors in the doped layer. We have further demonstrated that the redistribution of trapped charge in the doped layer of a heterostructure is attributable to a thermally-activated transfer of charge between the 2DEG and the doped layer.

While the nature of charge trapping in the DX centers that populate n-AlGaAs is well understood, further experimentation is necessary to understand the nature of the trap states in the InGaAs/InP heterostructure and their relative effects on the potential landscape in the 2DEG. A proposed experimental technique to probe these states, developed in collaboration with Dr. Theodore Martin, is described as follows:

First, it is necessary to establish whether the observed increase in 2DEG density upon illumination and subsequent PPC decay may be attributed to electron excitation across the band gap in either the InGaAs or the InP layers. This would be straightforward to accomplish by employing an illumination source whose photon energy does not exceed either band gap; given that $In_{0.25}Ga_{0.75}As$ is the smaller band gap material with a band gap of 644 meV, this corresponds to using an illumination source with a wavelength of at least 1.93 μm. Next, we may utilize the top gate on the device to probe the behavior of the charge traps. Note that the application of a negative voltage to this top gate will have the effect of moving the conduction band up with respect to the Fermi energy; since the binding energy of the Si donors is fixed with respect to the conduction band edge, we would expect to find donor reoccupation at higher temperatures as the gate is made more negative. Applying an increasing (negative) bias to the gate will also have the effect of increasing the energy level of the other interfacial trap states relative to the Fermi energy, although to varying degrees: since the cap/photoresist interface is twice as far from the 2DEG as the donor layer, and the 2DEG is held at 0 V with respect to the gate, we may expect that the conduction band moves up by twice as much at the interface than at the donor layer. Thus, by repeating the aforementioned density vs temperature measurements after illumination and at a range of negative applied gate biases, it may be possible to distinguish between charging of the donor sites and of the interfacial trap states.

APPENDIX A

GENERALIZING MCF CORRELATION FIT FUNCTION

The correlation between two MCF measured on modulation-doped electron billiard devices due to thermally-activated charge transfer among dopant atoms is modeled by

$$F_{\text{fit}} = \exp\left[-\frac{t}{\tau_0}\exp\left(-\frac{\beta}{k_B T_i}\right)\right], \qquad \text{(Equation A.1)}$$

where t is the time interval spent at intermediate temperature T_i. Note that, for a time interval $t = t_1 + t_2$ (held at a constant temperature T_i), we may write

$$F(T_i, t_1) \cdot F(T_i, t_2) = F(T_i, t_1 + t_2) = F(T_i, t). \qquad \text{(Equation A.2)}$$

Given a situation in which $t = \sum_j t_j$, but where the temperature varies as a function of time (i.e., $T = T(t_j)$), the simplification is not so elegant, but we may still compute F_{fit} as the product of terms $F(T_j, \Delta t_j)$:

$$F(T_j, t) = \prod_{T_j \le T_i} \exp\left[-\frac{\Delta t(T_j)}{\tau_0}\exp\left(-\frac{\beta}{k_B T_j}\right)\right] \qquad \text{(Equation A.3)}$$

$$= \exp\left[-\frac{1}{\tau_0}\sum_{T_j \le T_i} \Delta t(T_j)\exp\left(-\frac{\beta}{k_B T_j}\right)\right]. \qquad \text{(Equation A.4)}$$

Now, we let the time interval Δt shrink to the infinitesimal dt such that we may replace $\sum_{T_j}$ with $\int\ dt$ (note that summing over T_j is identical to summing over the corresponding time intervals Δt, so that we may replace a sum over temperatures with an integral over corresponding times):

$$F(T_i,t) = \exp\left[-\frac{1}{\tau_0}\int_{t=0}^{t(T_i)} dt \exp\left(-\frac{\beta}{k_B T_j(t)}\right)\right] \qquad \text{(Equation A.5)}$$

$$= \exp\left[-\frac{1}{\tau_0}\int_{T_j=0}^{T_i} dT_j \frac{dt}{dT_j} \exp\left(-\frac{\beta}{k_B T_j}\right)\right]. \qquad \text{(Equation A.6)}$$

To compute this integral, we need to know how the temperature varies with time. In practice, when heating a sample in the cryostat, temperature is empirically found to rise roughly with the square root of time as

$$T_j(t) = 9.67 \cdot t^{1/2}, \qquad \text{(Equation A.7)}$$

such that

$$t(T_j) = 0.0107 T_j^2 \qquad \text{(Equation A.8)}$$

and

$$\frac{dt}{dT_j} = 0.0214 T_j. \qquad \text{(Equation A.9)}$$

On the other hand, when cooling a sample, temperature falls roughly linearly with time at a rate of 2.4 K/min, such that $dt/dT_j \approx 0.41$ min/K. Figure A.1 displays the temperature data from which these rates were inferred.

Finally, if the sample is held at some temperature T_i for total time $t(T_i)$ we know that Equation A.6 must collapse to the form of Equation A.1, so we may say that in this case, $dt/dT_j = t(T_i)\delta(T_j - T_i)$.

If we index these three stages of temperature variation—heating the sample, holding the sample at a temperature T_i, and cooling the sample back to a base measurement temperature—as k = 1, 2, and 3, respectively, we may then write the

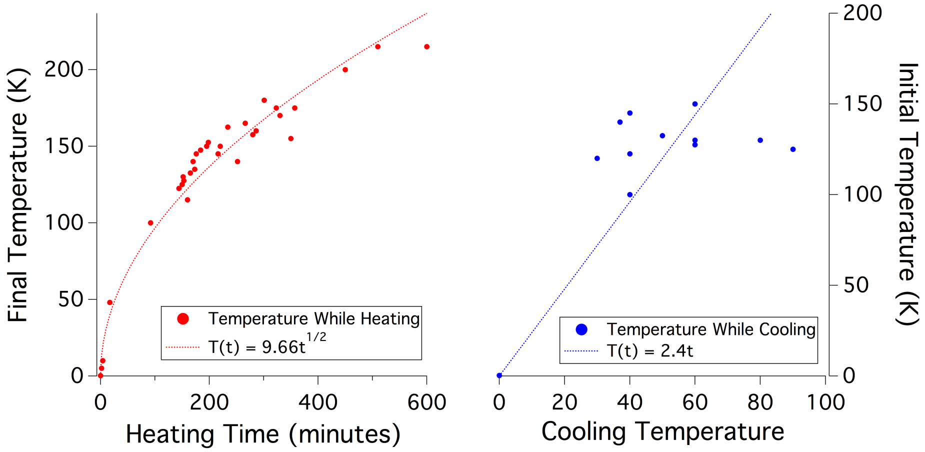

FIGURE A.1. Characterizing the heating and cooling rates for an electrical sample in the cryostat. Left: Final temperature of the sample plotted against the total time required to reach that temperature (solid red) and fit line demonstrating $T \propto \sqrt{t}$ (dashed red). Right: Initial temperature of the sample plotted against the total time required to cool to 240 mK (solid blue) and fit line demonstrating $T \propto t$ (dashed blue).

total contribution to F_{fit} as:

$$F_{\text{fit}}(T_i) = \exp\left[-\frac{1}{\tau_0}\sum_{k=1,2,3}\int_{T_j=0}^{T_i} dT_j \left(\frac{dt}{dT_j}\right)_k \exp\left(-\frac{\beta}{k_B T_j}\right)\right] \qquad \text{(Equation A.10)}$$

$$\begin{aligned} &= \exp\left\{-\frac{1}{\tau_0}\right. \\ &\left[0.0214\int_{T_j=0}^{T_i} dT_j T_j \exp\left(-\frac{\beta}{k_B T_j}\right)\right. \\ &+ t(T)\exp\left(-\frac{\beta}{k_B T_i}\right) \\ &\left.\left. + \ 0.41\int_{T_j=0}^{T_i} dT_j \exp\left(-\frac{\beta}{k_B T_j}\right)\right]\right\}. \end{aligned} \qquad \text{(Equation A.11)}$$

APPENDIX B

NORMALIZED SCALE PLOTS FROM CHAPTER IV ANALYSIS

The normalized scaling plots for all the traces analyzed and for all the analysis techniques utilized in Chapter IV are displayed in the following six pages. In these figures, the MD-MCF traces (red) are denoted MDx and their corresponding fBm traces (blue) denoted FF8x; the UD-MCF traces (red) are denoted UDx and their corresponding fBm traces (blue) denoted FF16x. Also included in these plots are the best-fit lines to each data set; however, since these correspondences are chosen so as to minimize the differences between each pair of best-fit lines, these fit lines are nearly indistinguishable in all cases.

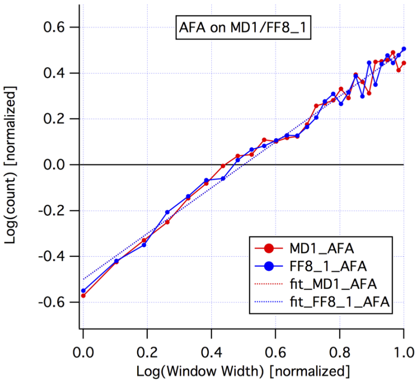
AFA on MD1/FF8_1
Log(count) [normalized]
Log(Window Width) [normalized]
0.6
0.4
0.2
0.0
-0.2
-0.4
-0.6
0.0
0.2
0.4
0.6
0.8
1.0
● MD1_AFA
● FF8_1_AFA
fit_MD1_AFA
fit_FF8_1_AFA

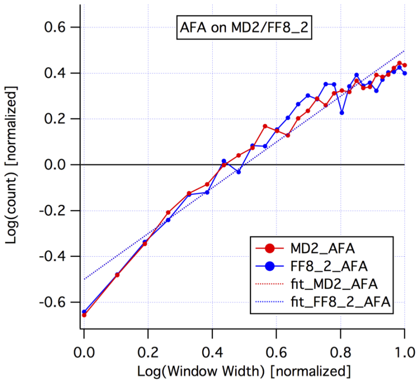
AFA on MD2/FF8_2
Log(count) [normalized]
Log(Window Width) [normalized]
0.6
0.4
0.2
0.0
-0.2
-0.4
-0.6
0.0
0.2
0.4
0.6
0.8
1.0
● MD2_AFA
● FF8_2_AFA
fit_MD2_AFA
fit_FF8_2_AFA

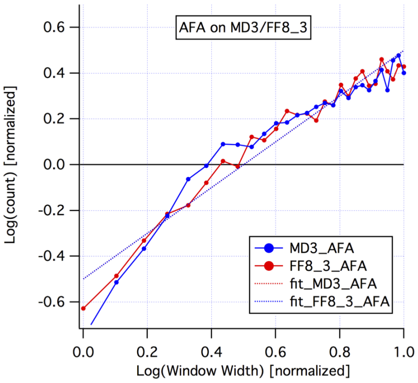
AFA on MD3/FF8_3
Log(count) [normalized]
Log(Window Width) [normalized]
0.6
0.4
0.2
0.0
-0.2
-0.4
-0.6
0.0
0.2
0.4
0.6
0.8
1.0
● MD3_AFA
● FF8_3_AFA
fit_MD3_AFA
fit_FF8_3_AFA

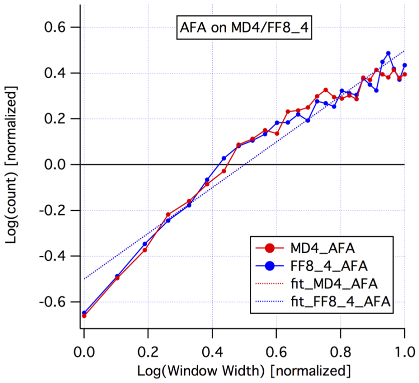
AFA on MD4/FF8_4
Log(count) [normalized]
Log(Window Width) [normalized]
0.6
0.4
0.2
0.0
-0.2
-0.4
-0.6
0.0
0.2
0.4
0.6
0.8
1.0
● MD4_AFA
● FF8_4_AFA
fit_MD4_AFA
fit_FF8_4_AFA

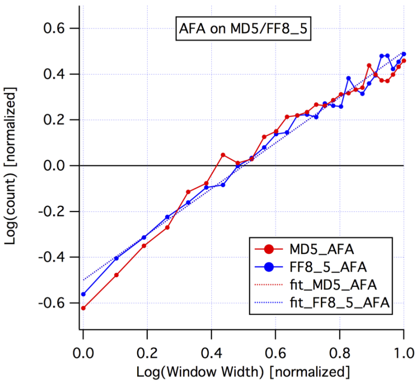
AFA on MD5/FF8_5
Log(count) [normalized]
Log(Window Width) [normalized]
0.6
0.4
0.2
0.0
-0.2
-0.4
-0.6
0.0
0.2
0.4
0.6
0.8
1.0
● MD5_AFA
● FF8_5_AFA
fit_MD5_AFA
fit_FF8_5_AFA

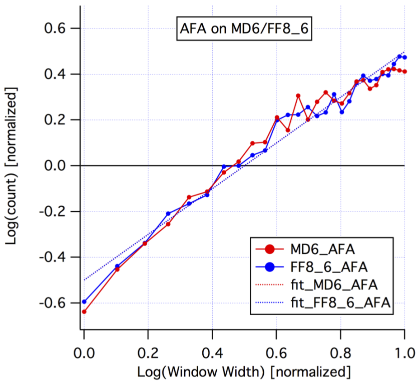
AFA on MD6/FF8_6
Log(count) [normalized]
Log(Window Width) [normalized]
0.6
0.4
0.2
0.0
-0.2
-0.4
-0.6
0.0
0.2
0.4
0.6
0.8
1.0
● MD6_AFA
● FF8_6_AFA
fit_MD6_AFA
fit_FF8_6_AFA

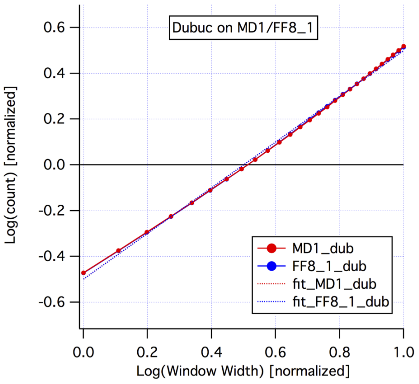

Dubuc on MD1/FF8_1
Log(count) [normalized]
0.6
0.4
0.2
0.0
-0.2
-0.4
-0.6
0.0
0.2
0.4
0.6
0.8
1.0
Log(Window Width) [normalized]
MD1_dub
FF8_1_dub
fit_MD1_dub
fit_FF8_1_dub

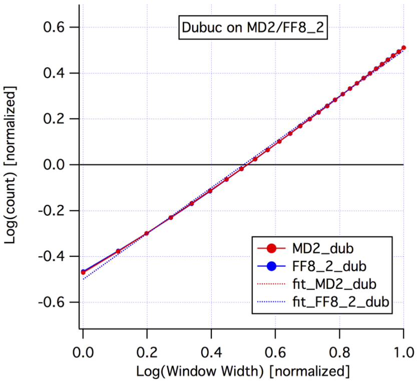

Dubuc on MD2/FF8_2
Log(count) [normalized]
0.6
0.4
0.2
0.0
-0.2
-0.4
-0.6
0.0
0.2
0.4
0.6
0.8
1.0
Log(Window Width) [normalized]
MD2_dub
FF8_2_dub
fit_MD2_dub
fit_FF8_2_dub

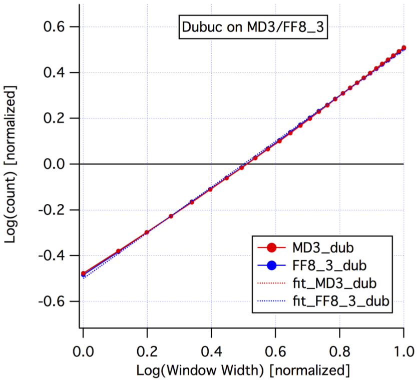

Dubuc on MD3/FF8_3
Log(count) [normalized]
0.6
0.4
0.2
0.0
-0.2
-0.4
-0.6
0.0
0.2
0.4
0.6
0.8
1.0
Log(Window Width) [normalized]
MD3_dub
FF8_3_dub
fit_MD3_dub
fit_FF8_3_dub

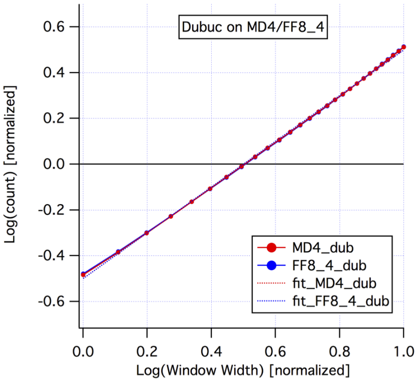

Dubuc on MD4/FF8_4
Log(count) [normalized]
0.6
0.4
0.2
0.0
-0.2
-0.4
-0.6
0.0
0.2
0.4
0.6
0.8
1.0
Log(Window Width) [normalized]
MD4_dub
FF8_4_dub
fit_MD4_dub
fit_FF8_4_dub

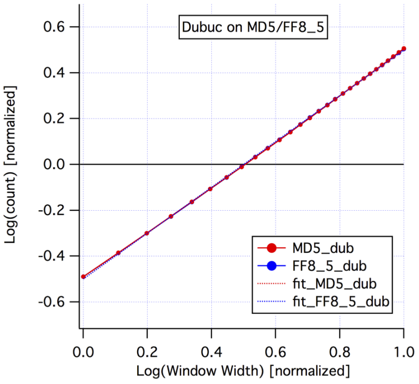

Dubuc on MD5/FF8_5
Log(count) [normalized]
0.6
0.4
0.2
0.0
-0.2
-0.4
-0.6
0.0
0.2
0.4
0.6
0.8
1.0
Log(Window Width) [normalized]
MD5_dub
FF8_5_dub
fit_MD5_dub
fit_FF8_5_dub

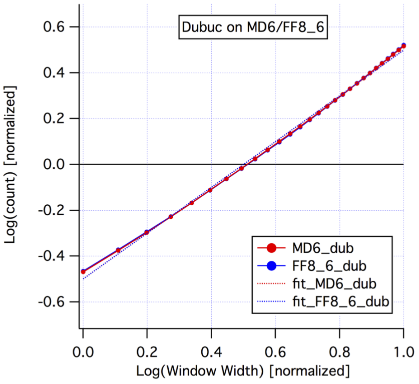

Dubuc on MD6/FF8_6
Log(count) [normalized]
0.6
0.4
0.2
0.0
-0.2
-0.4
-0.6
0.0
0.2
0.4
0.6
0.8
1.0
Log(Window Width) [normalized]
MD6_dub
FF8_6_dub
fit_MD6_dub
fit_FF8_6_dub

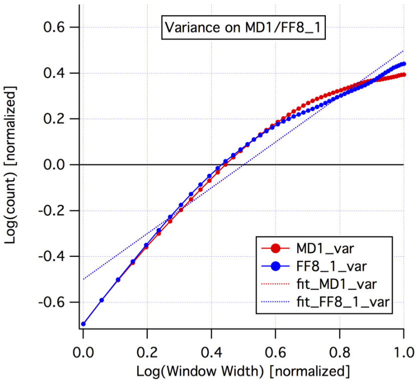
Variance on MD1/FF8_1
Log(count) [normalized]
Log(Window Width) [normalized]
0.6
0.4
0.2
0.0
-0.2
-0.4
-0.6
0.0
0.2
0.4
0.6
0.8
1.0
MD1_var
FF8_1_var
fit_MD1_var
fit_FF8_1_var

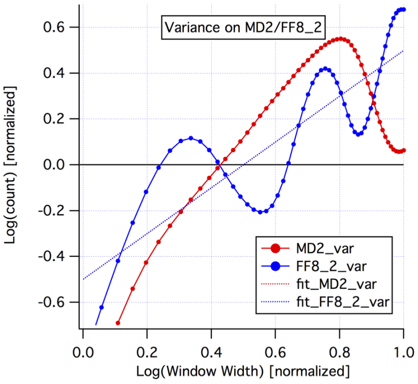
Variance on MD2/FF8_2
Log(count) [normalized]
Log(Window Width) [normalized]
0.6
0.4
0.2
0.0
-0.2
-0.4
-0.6
0.0
0.2
0.4
0.6
0.8
1.0
MD2_var
FF8_2_var
fit_MD2_var
fit_FF8_2_var

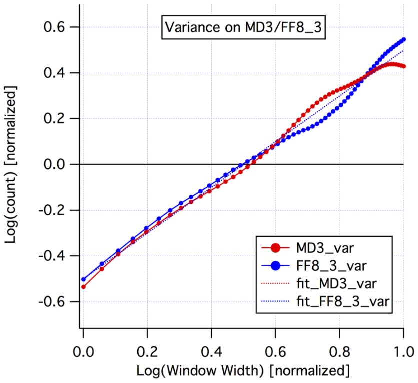
Variance on MD3/FF8_3
Log(count) [normalized]
Log(Window Width) [normalized]
0.6
0.4
0.2
0.0
-0.2
-0.4
-0.6
0.0
0.2
0.4
0.6
0.8
1.0
MD3_var
FF8_3_var
fit_MD3_var
fit_FF8_3_var

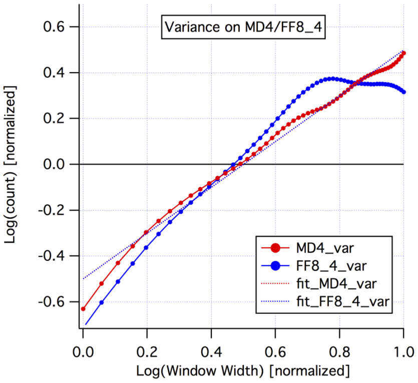
Variance on MD4/FF8_4
Log(count) [normalized]
Log(Window Width) [normalized]
0.6
0.4
0.2
0.0
-0.2
-0.4
-0.6
0.0
0.2
0.4
0.6
0.8
1.0
MD4_var
FF8_4_var
fit_MD4_var
fit_FF8_4_var

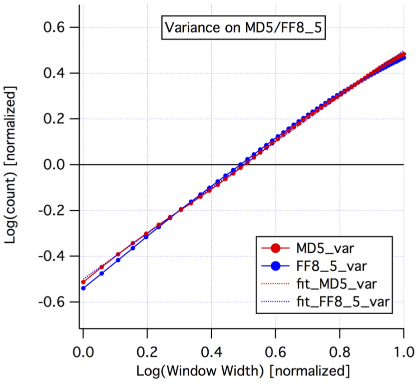
Variance on MD5/FF8_5
Log(count) [normalized]
Log(Window Width) [normalized]
0.6
0.4
0.2
0.0
-0.2
-0.4
-0.6
0.0
0.2
0.4
0.6
0.8
1.0
MD5_var
FF8_5_var
fit_MD5_var
fit_FF8_5_var

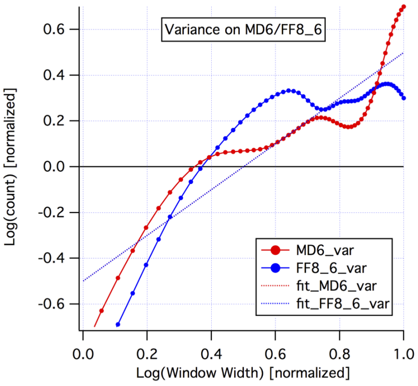
Variance on MD6/FF8_6
Log(count) [normalized]
Log(Window Width) [normalized]
0.6
0.4
0.2
0.0
-0.2
-0.4
-0.6
0.0
0.2
0.4
0.6
0.8
1.0
MD6_var
FF8_6_var
fit_MD6_var
fit_FF8_6_var

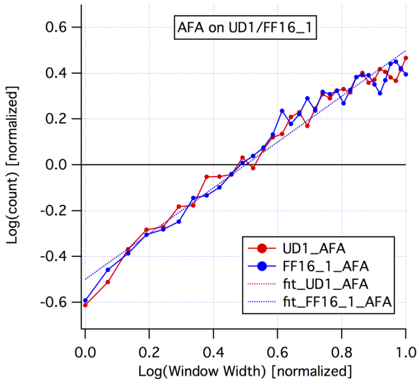
AFA on UD1/FF16_1
Log(count) [normalized]
Log(Window Width) [normalized]
0.6
0.4
0.2
0.0
-0.2
-0.4
-0.6
0.0
0.2
0.4
0.6
0.8
1.0
UD1_AFA
FF16_1_AFA
fit_UD1_AFA
fit_FF16_1_AFA

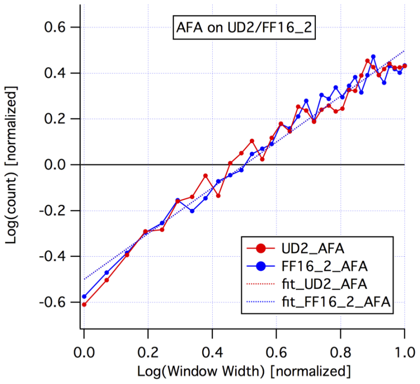
AFA on UD2/FF16_2
Log(count) [normalized]
Log(Window Width) [normalized]
0.6
0.4
0.2
0.0
-0.2
-0.4
-0.6
0.0
0.2
0.4
0.6
0.8
1.0
UD2_AFA
FF16_2_AFA
fit_UD2_AFA
fit_FF16_2_AFA

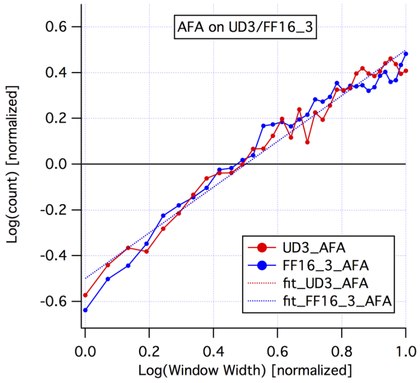
AFA on UD3/FF16_3
Log(count) [normalized]
Log(Window Width) [normalized]
0.6
0.4
0.2
0.0
-0.2
-0.4
-0.6
0.0
0.2
0.4
0.6
0.8
1.0
UD3_AFA
FF16_3_AFA
fit_UD3_AFA
fit_FF16_3_AFA

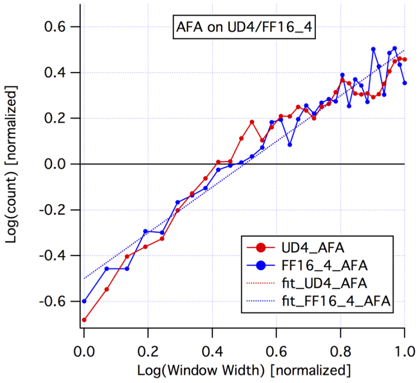
AFA on UD4/FF16_4
Log(count) [normalized]
Log(Window Width) [normalized]
0.6
0.4
0.2
0.0
-0.2
-0.4
-0.6
0.0
0.2
0.4
0.6
0.8
1.0
UD4_AFA
FF16_4_AFA
fit_UD4_AFA
fit_FF16_4_AFA

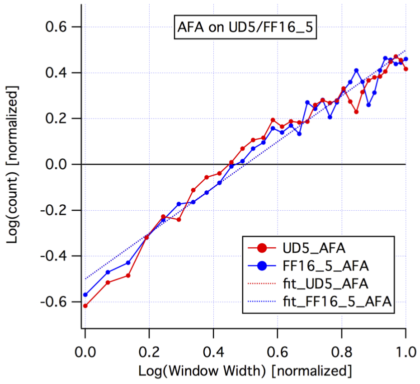
AFA on UD5/FF16_5
Log(count) [normalized]
Log(Window Width) [normalized]
0.6
0.4
0.2
0.0
-0.2
-0.4
-0.6
0.0
0.2
0.4
0.6
0.8
1.0
UD5_AFA
FF16_5_AFA
fit_UD5_AFA
fit_FF16_5_AFA

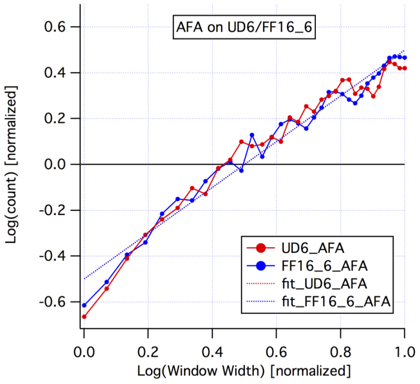
AFA on UD6/FF16_6
Log(count) [normalized]
Log(Window Width) [normalized]
0.6
0.4
0.2
0.0
-0.2
-0.4
-0.6
0.0
0.2
0.4
0.6
0.8
1.0
UD6_AFA
FF16_6_AFA
fit_UD6_AFA
fit_FF16_6_AFA

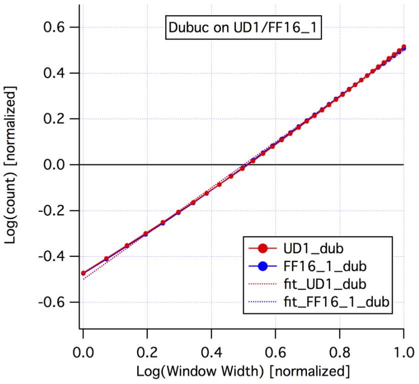
Dubuc on UD1/FF16_1
Log(count) [normalized]
0.6
0.4
0.2
0.0
-0.2
-0.4
-0.6
0.0
0.2
0.4
0.6
0.8
1.0
Log(Window Width) [normalized]
UD1_dub
FF16_1_dub
fit_UD1_dub
fit_FF16_1_dub

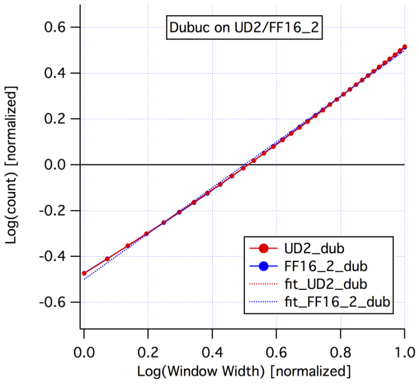
Dubuc on UD2/FF16_2
Log(count) [normalized]
0.6
0.4
0.2
0.0
-0.2
-0.4
-0.6
0.0
0.2
0.4
0.6
0.8
1.0
Log(Window Width) [normalized]
UD2_dub
FF16_2_dub
fit_UD2_dub
fit_FF16_2_dub

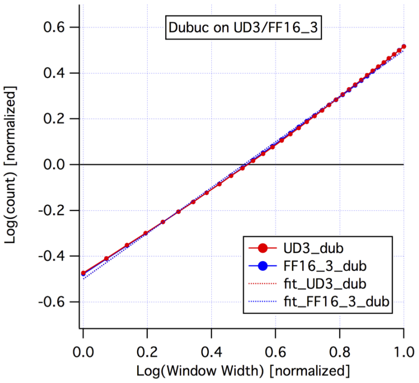
Dubuc on UD3/FF16_3
Log(count) [normalized]
0.6
0.4
0.2
0.0
-0.2
-0.4
-0.6
0.0
0.2
0.4
0.6
0.8
1.0
Log(Window Width) [normalized]
UD3_dub
FF16_3_dub
fit_UD3_dub
fit_FF16_3_dub

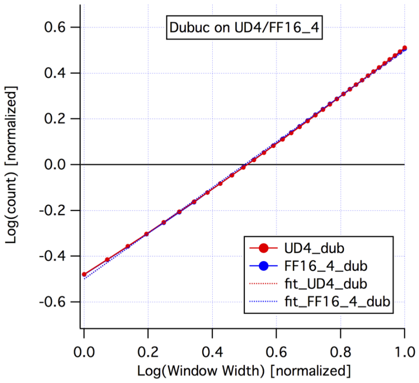
Dubuc on UD4/FF16_4
Log(count) [normalized]
0.6
0.4
0.2
0.0
-0.2
-0.4
-0.6
0.0
0.2
0.4
0.6
0.8
1.0
Log(Window Width) [normalized]
UD4_dub
FF16_4_dub
fit_UD4_dub
fit_FF16_4_dub

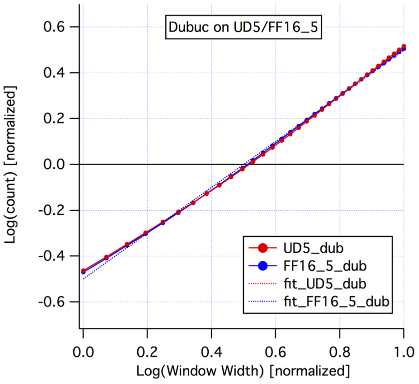
Dubuc on UD5/FF16_5
Log(count) [normalized]
0.6
0.4
0.2
0.0
-0.2
-0.4
-0.6
0.0
0.2
0.4
0.6
0.8
1.0
Log(Window Width) [normalized]
UD5_dub
FF16_5_dub
fit_UD5_dub
fit_FF16_5_dub

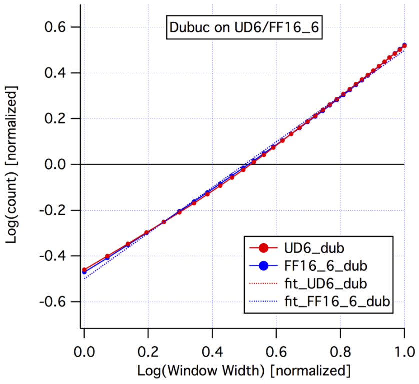
Dubuc on UD6/FF16_6
Log(count) [normalized]
0.6
0.4
0.2
0.0
-0.2
-0.4
-0.6
0.0
0.2
0.4
0.6
0.8
1.0
Log(Window Width) [normalized]
UD6_dub
FF16_6_dub
fit_UD6_dub
fit_FF16_6_dub

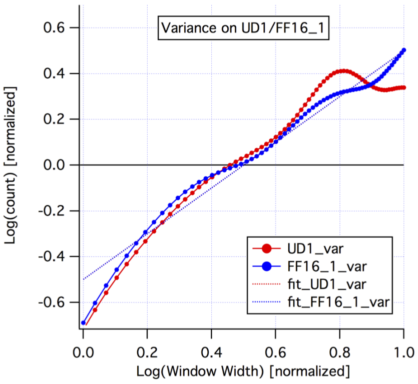
Variance on UD1/FF16_1
UD1_var
FF16_1_var
fit_UD1_var
fit_FF16_1_var
0.6
0.4
0.2
0.0
-0.2
-0.4
-0.6
Log(count) [normalized]
0.0
0.2
0.4
0.6
0.8
1.0
Log(Window Width) [normalized]

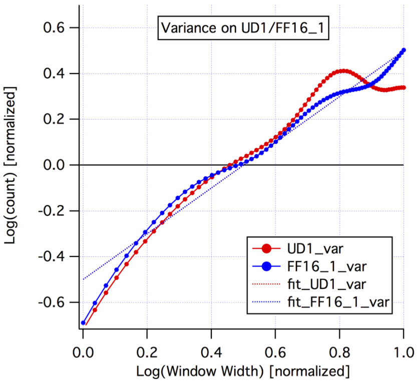
Variance on UD1/FF16_1
UD1_var
FF16_1_var
fit_UD1_var
fit_FF16_1_var
0.6
0.4
0.2
0.0
-0.2
-0.4
-0.6
Log(count) [normalized]
0.0
0.2
0.4
0.6
0.8
1.0
Log(Window Width) [normalized]

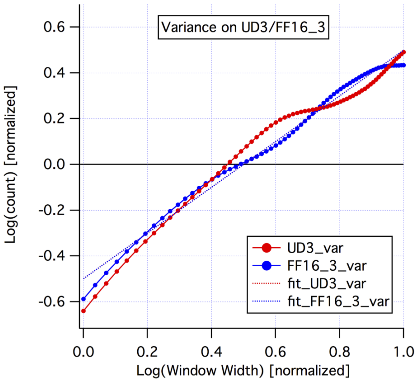
Variance on UD3/FF16_3
UD3_var
FF16_3_var
fit_UD3_var
fit_FF16_3_var
0.6
0.4
0.2
0.0
-0.2
-0.4
-0.6
Log(count) [normalized]
0.0
0.2
0.4
0.6
0.8
1.0
Log(Window Width) [normalized]

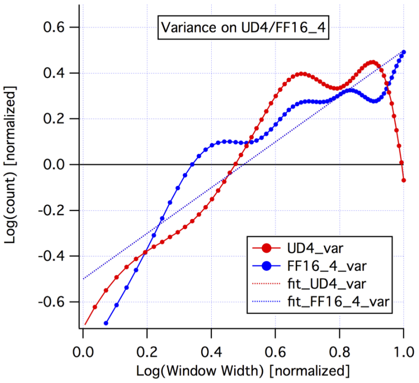
Variance on UD4/FF16_4
UD4_var
FF16_4_var
fit_UD4_var
fit_FF16_4_var
0.6
0.4
0.2
0.0
-0.2
-0.4
-0.6
Log(count) [normalized]
0.0
0.2
0.4
0.6
0.8
1.0
Log(Window Width) [normalized]

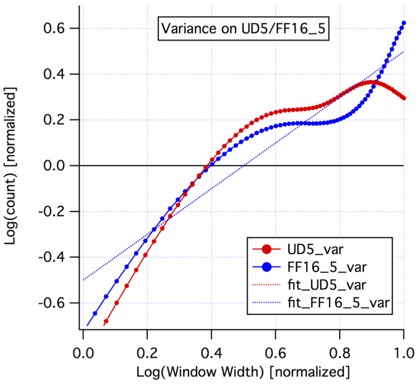
Variance on UD5/FF16_5
UD5_var
FF16_5_var
fit_UD5_var
fit_FF16_5_var
0.6
0.4
0.2
0.0
-0.2
-0.4
-0.6
Log(count) [normalized]
0.0
0.2
0.4
0.6
0.8
1.0
Log(Window Width) [normalized]

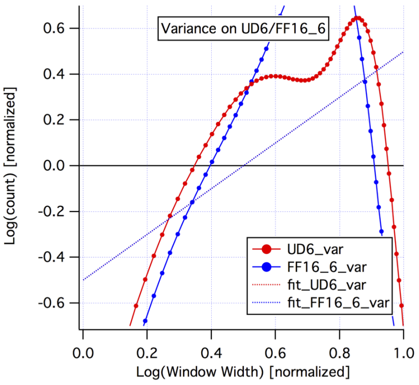
Variance on UD6/FF16_6
UD6_var
FF16_6_var
fit_UD6_var
fit_FF16_6_var
0.6
0.4
0.2
0.0
-0.2
-0.4
-0.6
Log(count) [normalized]
0.0
0.2
0.4
0.6
0.8
1.0
Log(Window Width) [normalized]

REFERENCES CITED

[1] Y. Aharonov and D. Bohm. Significance of electromagnetic potentials in the quantum theory. *Phys. Rev.*, 115:485, 1959.

[2] B. C. Scannell, I. Pilgrim, A. M. See, R. D. Montgomery, P. K. Morse, M. S. Fairbanks, C. A. Marlow, H. Linke, I. Farrer, D. A. Ritchie, A. R. Hamilton, A. P. Micolich, L. Eaves, and R. P. Taylor. Probing the sensitivity of electron wave interference to disorder-induced scattering in solid-state devices. *Phys. Rev. B*, 85:195319, 2012.

[3] G. E. Moore. Cramming more components onto integrated circuits. *Electronics Magazine*, page 114, April 1965.

[4] A. P. Micolich, A. M. See, B. C. Scannell, C. A. Marlow, T. P. Martin, I. Pilgrim, A. R. Hamilton, H. Linke, and R. P. Taylor. Is it the boundaries or disorder that dominates electron transport in semiconductor 'billiards'? *Fortschr. Phys.*, 61:332, 2013.

[5] R. G. Chambers. Shift of an electron interference pattern by enclosed magnetic flux. *Phys. Rev. Lett.*, 5:3, 1960.

[6] C. M. Marcus, A. J. Rimberg, R. M. Westervelt, P. F. Hopkins, and A. C. Gossard. Conductance fluctuations and chaotic scattering in ballistic microstructures. *Phys. Rev. Lett.*, 69:506, 1992.

[7] M. J. Berry, J. A. Katine, R. M. Westervelt, and A. C. Gossard. Influence of shape on electron transport in ballistic quantum dots. *Phys. Rev. B*, 50 (17721(R)), 1994.

[8] R. P. Taylor, R. Newbury, A. S. Sachrajda, Y. Feng, P. T. Coleridge, C. Dettmann, N. Zhu, H. Guo, A. Delage, P. J. Kelly, and Z. Wasilewski. Self-similar magnetoresistance of a semiconductor sinai billiard. *Phys. Rev. Lett.*, 78(10):1952–1955, 1997.

[9] R. P. Taylor, A. P. Micolich, R. Newbury, and T. M. Fromhold. Correlation analysis of self-similarity in semiconductor billiards. *Phys. Rev. B*, 56:R12733, 1997.

[10] R. A. Jalabert, H. U. Baranger, and A. D. Stone. Conductance fluctuations in the ballistic regime: a probe of quantum chaos? *Phys. Rev. Lett.*, 65:2442, 1990.

[11] M. A. Topinka, B. J. LeRoy, R. M. Westervelt, S. E. J. Shaw, R. Fleischmann, E. J. Heller, K. D. Maranowski, and A. C. Gossard. Coherent branched flow in a two-dimensional electron gas. *Nature*, 410:183, 2001.

[12] A. P. Micolich, R. P. Taylor, R. Newbury, J. P. Bird, R. Wirtz, C. P. Dettmann, Y. Aoyagi, and T. Sugano. Geometry-induced fractal behaviour in a semiconductor billiard. *J. Phys.: Condens. Matter*, 10:1339, 1998.

[13] A. S. Sachrajda, R. Ketzmerick, C. Gould, Y. Feng, P. J. Kelly, A. Delage, and Z. Wasilewski. Fractal conductance fluctuations in a soft-wall stadium and a sinai billiard. *Phys. Rev. Lett.*, 80:1948, 1998.

[14] R. Ketzmerick. Fractal conductance fluctuations in generic chaotic cavities. *Phys. Rev. B*, 54:10841, 1996.

[15] N. W. Ashcroft and N. D. Mermin. *Solid State Physics.* Hold-Saunders International Editions, 1976.

[16] S. Datta. *Electronic Transport in Mescoscopic Systems.* Cambridge University Press, 1995.

[17] J. H. Davies. *The Physics of Low-Dimensional Semiconductors: An Introduction.* Cambridge University Press, 1998.

[18] A. M. See. *Undoped AlGaAs/GaAs quantum dots with thermally robust quantum properties.* PhD thesis, University of New South Wales, 2011.

[19] R. Dingle, H. L. Störmer, A. C. Gossard, and W. Wiegmann. Electron mobilities in modulation-doped semiconductor heterojunction superlattices. *Appl. Phys. Lett.*, 33:665, 1978.

[20] B. J. van Wees, H. van Houten, C. W. J. Beenakker, J. G. WIlliamson, L. P. Kouwenhoven, D. van der Marel, and C. T. Foxon. Quantized conductance of points contacts in a two-dimensional electron gas. *Phys. Rev. Lett.*, 60:848, 1988.

[21] C. W. J. Beenakker and H. van Houten. Quantum transport in semiconductor nanostructures. *Solid State Phys.*, 44:1, 1991.

[22] A. P. Micolich. *Fractal magneto-conductance fluctuations in mesoscopic semiconductor billiards.* PhD thesis, University of New South Wales, 2000.

[23] H. Hardtdegen, R. Meyer, M. Hollfelder, Th. Schäpers, J. Appenzeller, H. Lo/ken Larsen, Th. Klocke, C. Dieker, B. Lengeler, H. Lüth, and W. J ager. Optimization of modulation-doped ga$_{1-x}$in$_x$as/inp heterostructures towards extremely high mobilities. *J. Appl. Phys.*, 73:4489, 1993.

[24] P. Ramvall, N. Carlsson, P. Omling, L. Samuelson, W. Seifert, Q. Wang, K. Ishibashi, and Y. Aoyagi. Quantum transport in high mobility modulation doped ga$_{0.25}$in$_{0.75}$as/inp quantum wells. *J. Appl. Phys.*, 84:2112, 1998.

[25] C. A. Marlow, R. P. Taylor, T. P. Martin, B. C. Scannell, H. Linke, M. S. Fairbanks, G. D. R. Hall, I. Shorubalko, L. Samuelson, T. M. Fromhold, C. V. Brown, B. Hackens, S. Faniel, C. Gustin, V. Bayot, X. Wallart, S. Bollaert, and A. Cappy. Unified model of fractal conductance fluctuations for diffusive and ballistic semiconductor devices. *Phys. Rev. B*, 73:195318, 2006.

[26] B. E. Kane, L. N. Pfeiffer, K. W. West, and C. K. Harnett. Variable density high mobility two-dimensional electron and hole gases in a gated gaas/al$_x$ga$_{1-x}$as heterostructure. *Appl. Phys. Lett.*, 63:2132, 1993.

[27] A. M. See, I. Pilgrim, B. C. Scannell, R. D. Montgomery, O. Klochan, A. M. Burke, M. Aagesen, P. E. Lindelof, I. Farrer, D. A. Ritchie, R. P. Taylor, A. R. Hamilton, and A. P. Micolich. Impact of small-angle scattering on ballistic transport in quantum dots. *Phys. Rev. Lett.*, 108:196807, 2012.

[28] P. M. Solomon, P. J. Price, D. J. Frank, and D. C. La Tulipe. New phenomena in coupled transport between 2d and 3d electron-gas layers. *Phys. Rev. Lett.*, 63:2508, 1989.

[29] J. P. Bird, K. Ishibashi, D. K. Ferry, Y. Ochiai, Y. Aoyagi, and T. Sugano. Phase breaking in ballistic quantum dots: transition from two- to zero-dimensional behavior. *Phys. Rev. B*, 51:18037(R), 1995.

[30] B. C. Scannell. *Chaotic electron transport in semiconductor devices.* PhD thesis, University of Oregon, 2010.

[31] B. Mandelbrot. How long is the coast of britain? statistical self-similarity and fractal dimension. *Science*, 156(3775):636–638, 1967.

[32] L. F. Richardson. The problem of contiguity: An appendix to statistic of deadly quarrels. *General Systems Yearbook*, 6:139, 1961.

[33] B. Mandelbrot. *The Fractal Geometry of Nature.* W. H. Freeman and Co., 1982.

[34] R. F. Voss. Characterization and measurement of random fractals. *Phys. Scr.*, T13:27–32, 1986.

[35] A. P. Micolich, R. P. Taylor, A. G. Davies, J. P. Bird, R. Newbury, T. M. Fromhold, A. Ehlert, H. Linke, L. D. Macks, W. R. Tribe, E. H. Linfield, D. A. Ritchie, J. Cooper, Y. Aoyagi, and P. B. Wilkinson. Evolution of fractal patterns during a classical-quantum transition. *Phys. Rev. Lett.*, 87:036802, 2001.

[36] H. E. Hurst. Long-term storage capacity of reservoirs. *Trans. Am. Soc. Civ. Eng.*, 116:770–808, 1951.

[37] B. Dubuc, J. F. Quiniou, C. Roques-Carmes, and C. Tricot. Evaluating the fractal dimension of profiles. *Phys. Rev. A*, 39(3):1500–1512, 1989.

[38] M. A. Riley, S. Bonnette, N. Kuznetsov, S. Wallot, and J. Gao. A tutorial introduction to adaptive fractal analysis. *Front. Physio.*, 3(371), 2012.

[39] B. Mandelbrot and J. W. Van Ness. Fractional brownian motions, fractional noises and applications. *SIAM Rev.*, 10(4):422–437, 1968.

[40] B. Mandelbrot. Self-affine fractals and fractal dimension. *Phys. Scr.*, 32: 257–260, 1985.

[41] T. Gneiting and M. Schlather. Stochastic models that separate fractal dimension and the hurst effect. *SIAM Rev.*, 46:269, 2004.

[42] M. F. Barnsley, R. L. Devaney, B. Mandelbrot, H. O. Peitgen, D. Saupe, and R. F. Voss. *The Science of Fractal Images.* Springer-Verlag New York Inc., 1988.

[43] D. Labate, F. Canavero, and A. De Marchi. A comparison of fractal dimension and spectrum coefficient characterization of $1/f^{\alpha}$ noise. *Metrologia*, 31:51, 1994.

[44] M. Prusty and H. Schanz. Signature of directed chaos in the conductance of a nanowire. *Phys. Rev. Lett.*, 96:130601, 2006.

[45] R. P. Taylor, P. C. Main, L. Eaves, S. Thoms, S. P. Beaumont, and C. D. W. Wilkinson. Quantum interference effects as a tool to probe the sidewalls of sub-micrometre-size n^{+}gaas channels. *Can. J. Phys.*, 70:979, 1992.

[46] R. P. Taylor, P. C. Main, L. Eaves, S. P. Beaumont, S. Thoms, and C. D. W. Wilkinson. In W. Zawadzki, editor, *ICPS-19*, volume 1, page 83. Institute of Physics, Warsaw, Poland, 1988.

[47] H. van Houten, C. W. J. Beenakker, P. H. M. van Loosdrecht, T. J. Thornton, H. Ahmed, M. Pepper, C. T. Foxon, and J. J. Harris. Four-terminal magnetoresistance of a two-dimensional electron-gas constriction in the ballistic regime. *Phys. Rev. B*, 37:8534, 1988.

[48] M. A. Topinka, R. M. Westervelt, and E. J. Heller. Imaging electron flow, 2003.

[49] P. M. Mooney. Deep donor levels (d x centers) in iii-v semiconductors. *J. Appl. Phys.*, 67:R1, 1990.

[50] S. Ghosh and V. Kumar. Direct evidence for the negative-u nature of the dx center in $al_x ga_{1-x}$as. *Phys. Rev. B*, 46:7533, 1992.

[51] D. J. Chadi and K. J. Chang. Energetics of dx-center formation in gaas and $al_x ga_{1-x}$as alloys. *Phys. Rev. B*, 39:10063, 1989.

[52] P. M. Mooney, N. S. Caswell, and S. L. Wright. The capture barrier of the d x center in si-doped al$_x$ga$_{1-x}$as. *J. Appl. Phys.*, 62:4786, 1987.

[53] E. Calleja, P. M. Mooney, S. L. Wright, and M. Heiblum. Origin of the nonexponential thermal emission kinetics of d x centers in gaalas. *Appl. Phys. Lett.*, 49:657, 1986.

[54] A. C. Campbell and B. G. Streetman. Application of the williams-watts decay law to dx center capture and emission kinetics. *Appl. Phys. Lett.*, 54:445, 1989.

[55] L. X. He, K. P. Martin, and R. J. Higgins. Phonon-assisted tunneling in persistent-photocurrent decay. *Phys. Rev. B*, 39:13276, 1989.

[56] J. J. Plombon, W. W. Bewley, C. L. Felix, M. S. Sherwin, P. Hopkins, M. Sundaram, and A. C. Gossard. Far-infrared capture of electrons by dx centers. *Appl. Phys. Lett.*, 60:1972, 1992.

[57] S. Ghosh and V. Kumar. Stretched exponential relaxation of persistent photoconductivity due to the si-related dx centre in al$_x$ga$_{1-x}$as. *Europhys. Lett.*, 24:779, 1993.

[58] H. J. Queisser. Nonexponential relaxation of conductance near semiconductor interfaces. *Phys. Rev. Lett.*, 54:234, 1985.

[59] R. G. Palmer, D. L. Stein, E. Abrahams, and P. W. Anderson. Models of hierarchically constrained dynamics for glassy relaxation. *Phys. Rev. Lett.*, 53: 958, 1984.

[60] B. Sturman, E. Podivilov, and M. Gorkunov. Origin of stretched exponential relaxation for hopping-transport models. *Phys. Rev. Lett.*, 91:176602, 2003.

[61] M. S. Skolnick, P. J. Dean, S. H. Groves, and E. Kuphal. Donor identification in liquid phase epitaxial indium phosphide. *Appl. Phys. Lett.*, 45:962, 1984.

[62] T. P. Martin, A. Szorkovszky, A. P. Micolich, A. R. Hamilton, C. A. Marlow, R. P. Taylor, H. Linke, and H. Q. Xu. Field-oreintation dependence of the zeeman spin splitting in (in,ga)as quantum point contacts. *Phys. Rev. B*, 81: 041303(R), 2010.

[63] S. Müller, J. Pillath, W. Bauhofer, A. Kohl, and K. Heime. Persistent photoconductivity and electron density dependent magnetotransport measurements in narrow ingaas/inp quantum wells. *Appl. Phys. Lett.*, 61:1603, 1995.

[64] S. Feng, P. A. Lee, and A. D. Stone. Sensitivity of the conductance of a disordered metal to the motion of a single atom: implications for $1/f$ noise. *Phys. Rev. Lett.*, 56:1960, 1986.

[65] P. Ramvall. *InP and Related Compounds: Materials, Applications and Devices*, chapter VIII. Gordon and Breach Science Publishers, 2000.

[66] H. P. Wei, D. C. Tsui, and M. Razeghi. Persistent photoconductivity and the quantized hall effect in in0.53ga0.47as/inp heterostructures. *Appl. Phys. Lett.*, 45:666, 1984.

[67] M. J. Kane, D. A. Anderson, L. L. Taylor, and S. J. Bass. Transport properties and persistent photoconductivity in inp/in$_{0.53}$ga$_{0.47}$as modulation-doped heterostructures. *J. Appl. Phys.*, 60:657, 1986.